GSMBE GROWTH ON V-GROOVE PATTERNED SUBSTRATES FOR InP-BASED QUANTUM WIRES

by

JUN WANG, B.Sc., M.Sc.

A Thesis

Submitted to the School of Graduate Studies

In Partial Fulfillment of the Requirements

for the Degree

Doctor of Philosophy

McMaster University

© Copyright by Jun Wang, September 1997

GSMBE GROWTH ON V-GROOVED InP QUANTUM WIRES

DOCTOR OF PHILOSOPHY (1997)
(Engineering Physics)

McMASTER UNIVERSITY
Hamilton, Ontario

TITLE: GSMBE Growth on V-groove Patterned Substrates for InP-Based Quantum Wires

AUTHOR: Jun Wang

B.Sc. (Tianjin University)
M.Sc. (Chinese Academy of Science)
M.Sc. (Queen's University)

SUPERVISORS: Professor D.A. Thompson
Professor J.G. Simmons

NUMBER OF PAGES: xi, 139

ABSTRACT

Quantum wire (QWR) lasers are of interest because of predicted improvement of performance compared to quantum well lasers. For fiber optical communication, lasers are required that operate at wavelengths of 1.3 μm or 1.55 μm. This requires lasers grown in the InP-based materials. In the GaAs-based system, it has been shown that good QWR lasers can be achieved through epitaxial growth onto GaAs substrates having etched V-grooves. However, to date, no InP-based QWRs have been successfully grown in V-grooves. This arises from two problems: (i) the tendency for InP to planarize during growth, in contrast to the resharpening effect of AlGaAs; (ii) the potential for lattice-mismatch between InGaAs(P) and InP, which could result in strain relaxation and defect formation. Therefore, the purpose of this thesis is to establish the conditions whereby InGaAs/InGaAsP QWRs can be achieved and to confirm and characterize the one-dimensional behaviour.

V-grooves with both (111)A and (111)B sidewalls are used in this study. They are obtained using chemical etching. The etching process is explained and conditions necessary to achieve each type of V-groove are established. Gas source molecular beam epitaxy has been used to grow various epitaxial structures. For InP layers grown under different growth conditions, it is found that the V/III flux ratio significantly affects the shape of a V-groove bottom and the roughness of both the V-bottom and the sidewalls. With the growth conditions optimized, InP layers can be grown which retain the sharpness and the smoothness of the V-groove. The sharpness of the bottom of the groove is related to growth conditions that decrease the growth rate at the bottom by limiting the supply of the group V component. InGaAs/InP quantum well structures have been grown using the optimized conditions. For (111)A V-grooves, transmission electron microscopy shows that all epilayers are defect-free and that InGaAs/InP quantum wires are successfully obtained

with well thickness variation as high as a factor of 6. Lateral subband separations are estimated by a simple one-dimensional parabolic potential model with the thickness determined by TEM. Photoluminescence emission from the InGaAs quantum wires is spatially resolved with a spatially selective etch technique. For (111) B V-grooves, defects such as dislocations are observed in the bottom. However, the growth of bulk InGaAsP and InGaAs/InGaAsP yields different results. No extended defects have been observed in the InGaAsP layer grown in either (111) A or (111)B V-grooves. This is because, at the groove bottom the layer is both P and In rich, as analyzed by using energy dispersive X-rays. This tends to reduce the strain compared to InGaAs deposition, where the absence of P leads to In-rich, strained material. The growth of an InGaAsP layer in a (111)A V-groove results in a flat and wide bottom, which excludes the possibility of forming InGaAs/InGaAsP quantum wires. However, the growth of an InGaAsP layer in (111)B V-grooves results in a sharper bottom, such that crescent-shaped InGaAs/InGaAsP structures are formed when the InGaAs layer is very thin. Quantum-wire behaviour has been confirmed through the observation of lateral subbands in the photoluminescence (PL) spectra. This is further supported by polarization measurements. Also, the subband separation observed in PL spectra is consistent with a calculated value using the one-dimensional parabolic potential model. The InGaAs/InGaAsP QWRs should be able to be incorporated into laser structures.

ACKNOWLEDGEMENTS

I wish to thank Drs. D.A. Thompson and J.G. Simmons for their valuable supervision and for assigning this project, which exposed me to many aspects in the field of optoelectronics.

I would like to thank Dr. B.J. Robinson and S. McMaster for the MBE growth and advice in planning the growth.

I also would like to acknowledge my other colleagues at the Center for Electrophotonic Materials & Devices: K. Song, D. Stevanovic and E. Tan for support on processing, R. LaPierre for discussions on MBE and photoluminescence measurements, M. Beudreau, M. Boumerzoug and P. Mascher for SiN_x depositions; A. Gupta, C. Mullan X. Zhou and Dr. G. Weatherly for help with the TEM studies; Dr. D. Bruce, H. Pinkney, L. Balasubramanin, S. Nagy, X. Wu and R. Huang for general help; J. Swoger, J. Hazell, A. Pratt G. Dyck and Dr. J. Preston for laser characterization (electrically or optically pumped). I am also grateful to Dr. M. Davies and J. Stapleton at the National Research Council for SiO_2 depositions.

Finally I would like to thank my wife, Yan Xu, and my parents for their support throughout all aspects of my life. I also thank my little daughter Mingxue (Michelle) for giving me joy, and no trouble, during many very busy days.

TABLE OF CONTENT

LIST OF FIGURES

LIST OF TABLES

CHAPTER 1. INTRODUCTION

One-dimensional semiconductor structures, i.e. quantum wires (QWRs) have attracted great attention in the last several years (Kapon 1989, 1994, Bhat 1990, 1991, Tiwari 1994, Bulitka 1993a, Galeuchet 1988) because of their potential application in lasers and other devices. Quantum wire lasers are expected to show improved performance over quantum well lasers including lower threshold current, reduced temperature sensitivity, higher modulation speed and narrower spectral linewidth. In order to obtain 1-D quantum wire structures, lateral confinement is needed in addition to the confinement afforded by thin layer, quantum well growths. Various approaches have been investigated to obtain the lateral confinement. Among these techniques, growth onto V-grooved substrates by metalorganic chemical vapor deposition (MOCVD) or molecular beam epitaxy (MBE) has been shown to be one of the most promising (Kapon 1994, Tiwari 1994). If the V-bottom is kept sharp after the growth of a lower barrier layer, subsequent growth of a quantum well layer, under appropriate growth conditions, can result in a thickness variation across the V-bottom with largest thickness occurring at the center of the V. Such a thickness variation can produce lateral confinement of the electrons and holes, forming the basis of QWR lasers. Since deposition onto V-grooves is a one-step process (Kapon 1994, Tsang 1977), it has the potential for producing devices that would otherwise be difficult to achieve using post-growth etching or ion implantation techniques for defining the lateral dimensions. The interfaces defining the lateral extent of the structure are extremely important because of the very small size of the structures. Consequently interface states could dominate the carrier recombination process in the wire structures, thus quenching the optical emission. Furthermore, QWRs in V-grooves are buried-in structures, which

provide potential for 2-dimensional optical confinement and corresponding improvement in laser performance.

QWR lasers with very low threshold currents have been grown and fabricated onto V-grooved GaAs substrates (Kapon 1994, Tiwari 1994). Reported threshold currents are as low as 180 μA without facet coating (Tiwari 1994). However, much less progress has been made on InP-based materials (Kapon 1994, Bhat 1990, Bulitka 1993a,, Galeuchet 1988), in spite of their technological importance to lasers with operating wavelength of 1.3 μm or 1.55 μm, which is used in telecommunication system. Before this work, to our knowledge, no attempts to grow any QWRs on V-grooved InP substrates have been successful when evaluated in terms of wire size and shape, defect-free microstructure and optical properties, not to mention InP-based QWR lasers (Bhat 1990, 1991, Bulitka 1993a, Galeuchet 1988). One difficulty in the InP-based materials system relates to keeping a sharp V-groove shape during barrier layer growth, where, unlike the GaAs/AlGaAs system (Kapon 1994), no resharpening has been reported for deposition by either MBE or MOCVD. Another problem in the InGaAsP/InP and InGaAs/InAlAs/InP materials systems is lattice mismatch which is much higher than that in the GaAs/AlGaAs system (Bulitka 1993a Gupta 1997) and results from differential migration of the group III adatom species in a V-groove. For example, Bhat *et al* (1990, 1991) performed MOCVD growth of InGaAsP on non-planar InP substrates, and many defects were observed in the InGaAsP layers. On V-grooves with (211)A facets, a crescent-shaped well region developed, with the central region being approximately 1.5 times thicker than the sidewall. However, such a thickness variation and its lateral extent were not enough to produce significant lateral confinement, and no optical characterization was reported on the quantum wire-like region.

Therefore, in this work we have tried to overcome the above problems and explored the possibility of fabricating QWRs which could be used to produce InP-based lasers. In order to achieve suitable growth conditions, it was necessary to achieve the following

goals: etch appropriate V-grooves onto (100) InP substrates with sharp bottoms and smooth morphology; grow InP buffer layers that maintain the sharp V-bottoms and smooth sidewalls; evaluate InGaAs/InP structures; grow defect-free, thick InGaAsP layers with sharp bottoms; and finally achieve InGaAs/InGaAsP QWR behaviour.

Prior to MBE growth, V-grooves with sharp bottoms and smooth surface morphology need to be formed. This has been done with wet chemical etching. Since a groove profile depends on etchant, mask, native oxide condition, etc., a systematic study has been performed and the InP dissolution process and its dependence on crystal planes has been analyzed. Recipes for producing (111)A and (111)B V-grooves were developed. The (111) V-grooves are preferred to others for this work due to their acute angles at the bottoms.

The first epilayer of an InP-based QWR structure is the InP buffer layer. This may modify the V-bottom sharpness and sidewall smoothness significantly. Thus, its growth behaviour has been studied in order to establish necessary growth conditions for keeping sharp V-bottoms and smooth sidewalls. Having achieved this, InGaAs/InP QWRs were grown and the conditions under which relaxation did not occur were established.

The InGaAs/InP QWR structure, however, cannot serve as the active region of the InP-based laser structure. Instead, an InGaAs(P)/InGaAsP QWR is needed. Here, the InGaAsP layers are used for optical waveguiding. The challenge is to obtain a sharp, defect-free InGaAsP layer at the V-groove bottom, where differential group III (In, Ga) adatom migration and spatial variation in group V incorporation coefficient are seen to occur. The InGaAsP growth behaviour also depends upon the V-groove sidewall planes. Only if the problems associated with the InGaAsP layer can be overcome, is it possible that crescent-shaped InGaAs/InGaAsP QWRs can be achieved.

Detailed characterization of the QWR structures has been carried out. While standard techniques include scanning electron microscopy, transmission electron

microscopy, X-ray energy dispersive spectroscopy and photoluminescence, a selective etching technique has been developed for this study to enable the sources of the observed photoluminescence peaks to be spatially resolved. In addition, a simple QWR model and polarization dependence of QWR photoluminescence have been used to verify QWR formation.

This thesis presents experimental results to establish the conditions necessary for QWR growth, with characterization and analysis to confirm QWR behaviour. In Chapter 2, the theoretical background of QWRs and the current status on QWR research are reviewed. In Chapter 3, epitaxial growth on patterned substrates and its application to QWR fabrication is surveyed; in particular, issues of MBE growth on patterned substrates are discussed. The characterization techniques used are presented in Chapter 4. Chapter 5 contains V-groove etching results and associated analysis. Chapter 6 investigates the growth behaviour of InP in both (111)A and (111)B V-grooves; examines the InGaAs/InP structure; and demonstrates InGaAs/InP QWR formation in (111)A V-grooves. Chapter 7 presents the different growth behaviour of thick InGaAsP layers in V-grooves having (111)A or (111)B sidewalls; demonstrates the formation of InGaAs/InGaAsP QWRs in (111)B V-grooves and shows the characteristics of the QWRs using a simple model and photoluminescence techniques. Finally, conclusions are drawn in Chapter 8.

CHAPTER 2. INTRODUCTION TO QUANTUM WIRES

2.1. Semiconductor Quantum Structures

Since Esaki and Chang (1974) reported resonant electron tunneling across potential barriers and Dingle (1974) demonstrated the quantization of energy levels in quantum wells by optical absorption measurement, quantum structures have been widely applied in modern semiconductor devices, such as lasers and high electron mobility transistors. A semiconductor quantum structure is one involving quantum confinement of carriers. This happens when a low energy bandgap material is surrounded by a high energy bandgap material with one or more dimensions of the low energy bandgap material being less than the De Broglie wavelength of an electron. For example, when a very thin GaAs layer is sandwiched, in the growth direction, between AlGaAs layers, energy level quantization occurs along the growth direction such that the structure is called a quantum well (QWL). When the GaAs layer is additionally bounded by AlGaAs in one or two lateral directions, down to very small sizes, the structure is a quantum wire (QWR) or a quantum dot (QD) respectively.

The quantum confinement will significantly modify the energy band structure and the density of states (DOS) distribution of carriers, thus offering unique features in various structures. Generally, the energy levels of carriers can be obtained by solving the Schroedinger equation with an effective mass approximation,

$$\left[-\frac{\hbar^2}{2m^*}\nabla^2 + V(x,y,z)\right]\psi(x,y,z) = E\psi(x,y,z) \qquad 2.1$$

where $\psi(x, y, z)$ is the carrier envelope wavefunction, m^* is the carrier effective mass, $\hbar$ is Planck's constant, E is the energy and $V(x, y, z)$ is a potential distribution. For infinitely

deep rectangular-shaped potential wells, with dimensions t_x, t_y and t_z, the energy of the confined carriers, with respect to the band-edge, is given by

$$E_l = \frac{\hbar^2\pi^2 l^2}{2m^* t_x^2} + \frac{\hbar^2\left(k_y^2 + k_z^2\right)}{2m^*} \qquad \text{1D confinement} \qquad 2.2$$

$$E_{l,ml} = \frac{\hbar^2\pi^2}{2m^*}\left(\frac{l^2}{t_x^2} + \frac{m^2}{t_y^2}\right) + \frac{\hbar^2 k_z^2}{2m^*} \qquad \text{2D confinement} \qquad 2.3$$

$$E_{l,m,nl} = \frac{\hbar^2\pi^2}{2m^*}\left(\frac{l^2}{t_x^2} + \frac{m^2}{t_y^2} + \frac{n^2}{t_z^2}\right) \qquad \text{3D confinement} \qquad 2.4$$

where l, m, n = 1, 2, ... are quantum level numbers and k_y and k_z are wavevector components along the unconfined directions.

The quantum confinement not only modifies the energy levels, but also changes the density of states dramatically. The DOS (in unit volume) functions (ρ), including spin degeneracy, are

$$\rho_{3D} = \frac{\left(2m^*/\hbar^2\right)^{3/2}}{2\pi^2}\sqrt{E} \qquad 2.5$$

$$\rho_{2D} = \frac{m^*}{\pi\hbar^2 t_x}\sum_l \theta\left(E - E_l\right) \qquad \theta(x)\text{: a Heaviside function} \qquad 2.6$$

$$\rho_{1D} = \frac{(2m^*)^{1/2}}{\pi\hbar\, t_x t_y}\sum_{ml}\left(E - E_{l,m}\right)^{-1/2} \qquad 2.7$$

$$\rho_{0D} = \frac{2}{t_x t_y t_z}\sum_{.ml,n}\delta\left(E - E_{l,m,n}\right) \qquad 2.8$$

for a bulk sample, a quantum well, a quantum wire and a quantum dot respectively. As is seen in figure 2.1, the DOS distribution becomes sharper as the carrier dimensionality is reduced. In particular, a quantum well has step-shaped density of states, a quantum wire has a spike-shaped density of states and the density of states of a quantum dot is of discrete δ-function shape.

The modified energy levels and DOS due to reduced dimensionality affect the material and device properties significantly. Quantum well lasers have shown superior performance to conventional double heterojunction (bulk) lasers in terms of almost all

characteristic parameters (Yariv 1989), quantum wire lasers and quantum dot lasers have been predicted to have even better performance (Arakawa 1982, 1986).

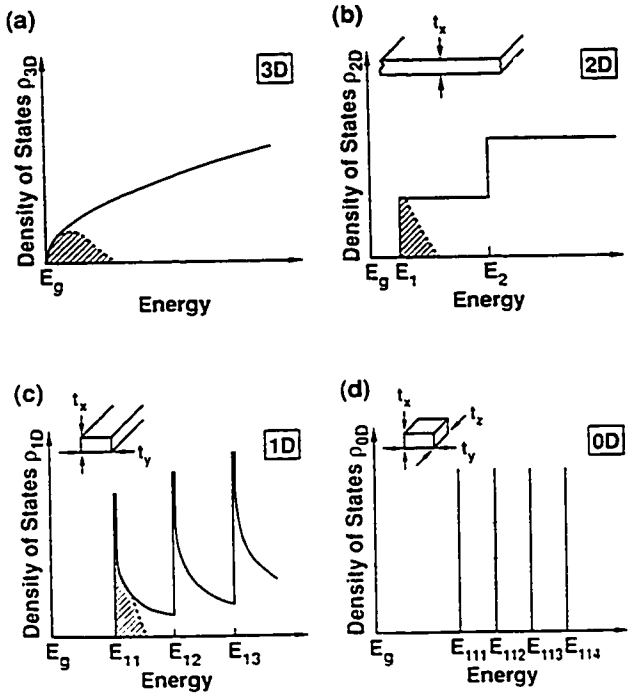

Figure 2.1. Density of states for a). bulk, b). a quantum well, c). a quantum wire, d). a quantum dot. The shaded areas indicate occupied states for similar carrier density. Insets illustrate different quantum structures (Kapon 1993).

The narrowing of the DOS distribution with reducing dimensionality results in confinement of carrier energy distribution to narrower spectral regions, as also shown in fig. 2.1. Hence, higher optical gain at a given carrier density, as well as higher differential gain, can be achieved in quantum confined lasers. The higher optical gain, together with a reduced volume of active regions in quantum confined lasers, can lead to low threshold currents in properly designed devices. For example, quantum wire lasers have been predicted to have micro-ampere threshold currents (Yariv 1989). Also, the temperature sensitivity of the threshold current can be reduced in low-dimensional quantum lasers

because the spectral confinement of carriers in low-dimensional lasers limits the spread in carrier distribution at elevated active region temperatures (Arakawa 1982). Furthermore, the higher differential gain in a low-dimensional laser can increase modulation bandwidth and reduce spectral linewidth. For example, theoretical calculation indicated that the modulation bandwidth of a QWR laser was almost twice that of a QWL laser (Arakawa 1986).

2.2. Quantum Wires

As discussed above, QWRs and QDs have superior properties to QWLs and bulk materials for many applications. However, applications of these low-dimensional structures have been limited by the fabrication techniques necessary to obtain them. The fabrication of either QWRs or QDs has been challenging. This work deals with QWRs only and further discussion will be confined to this topic.

Several techniques have been used to make QWRs. The most direct way has been by etching the wire patterns, usually produced by electron beam lithography, through etching masks placed on QWL wafers. This technique will produce rectangular-shaped QWRs, with the widths of QWRs limited by the resolution of the lithography. Recently 10-nm size InGaAs/InP QWRs have been reported (Notomi 1993), resulting in an approximate effective bandgap energy shift of 50 meV. The major problem of this technique is that the QWR quality is affected by nonradiative electron-hole recombination on the etched surfaces (Clausen 1989, Maile 1989).

QWRs have also been fabricated by patterned QWL disordering (Cibert 1986). In this technique, interdiffusion of group III elements is enhanced through focused ion beam implantation or diffusion of various species through a mask, leading to intermixing of the well and barrier materials and thus form lateral potential barriers. Although this technique avoids interface damage caused by etching steps, it often involves the introduction of defects or impurities to the wire interfaces (Zarem 1989) and the amount of lateral

confinement is limited by the obtainable change in composition (i.e. bandgap) resulted from intermixing.

Side growth of QWL heterojunctions on cleaved, multiple QWL wafers can also be used to form arrays of QWRs (Wegscheider 1994). This technique has the advantage of controlling the lateral dimensions of the QWRs with the layer uniformity and accuracy of epitaxial growth technique. However, this is achieved at the expense of reduced flexibility in structure design and the greater difficulty of growth on (011) surfaces (Allen 1988). In contrast to other QWRs, the resultant potential profile by this technique is T-shaped (Wegscheider 1994).

In addition to the QWRs obtained with above techniques that involve post-growth process steps or regrowth, various configurations of QWRs can also be developed with in-situ growth techniques. These include growth on dielectric mask patterned substrates (Koshiba 1994, Arakawa 1993), growth on vicinal substrates (Petroff 1994), growth on ridge-pattered substrates (Finnie 1995, Sugimoto 1993) and on V-grooved substrates (Kapon 1994). This latter technique will be discussed in more detail in the next chapter. Usually the shapes of QWRs obtained by these techniques are not rectangular, thus, some approximations have to be made in their analysis, such as the QWR subband energy level calculation.

2.3. Crescent-shaped Quantum Wire Model

QWRs realized by growth in V-grooves usually have a crescent-shape. Fortunately, their potential profiles can be approximated by parabolic-shapes in most cases; thus, their QWR subband energy levels can be readily estimated.

As illustrated in fig. 2.2 (a), a crescent-shaped QWR grown in a V-groove is a structure with a sufficiently narrow QWL section laterally bounded by thinner QWL

regions. In fact, it is a tapered QWL. This variation in quantum well thickness forms a QWR and the formation of 1D subbands can be readily modelled.

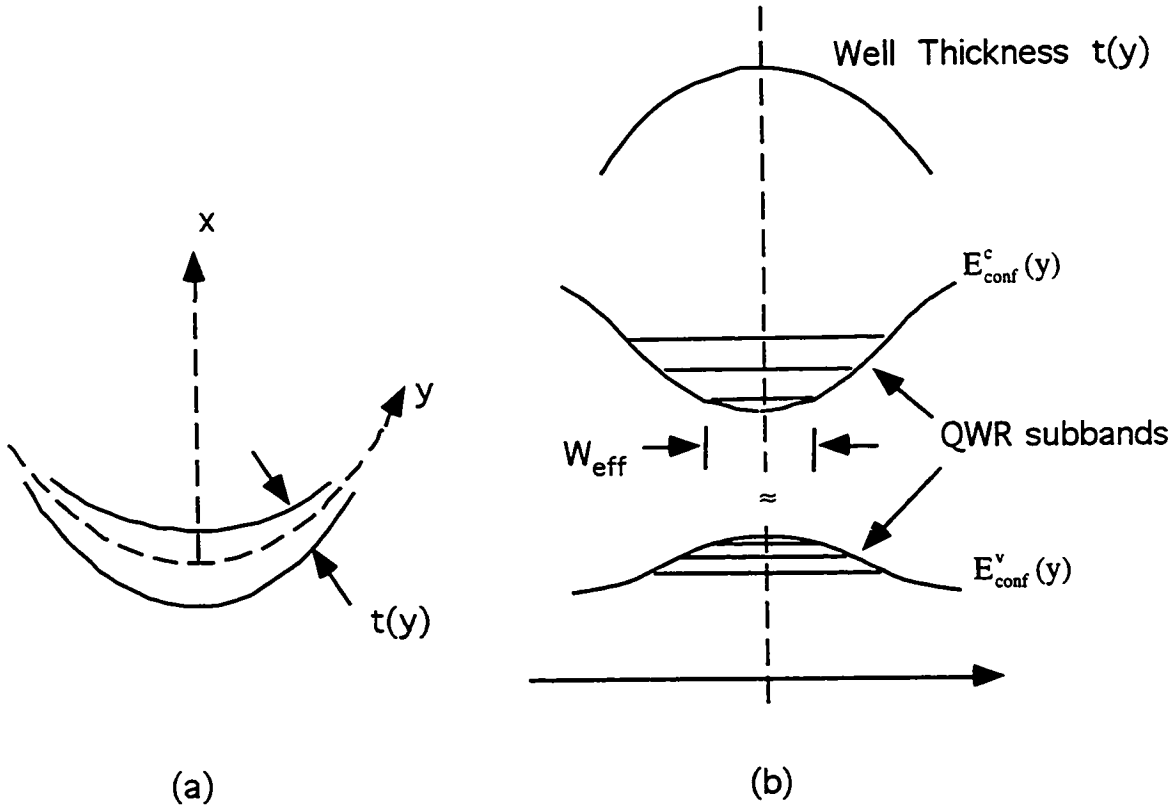

Figure 2.2. (a). A crescent-shaped quantum wire. (b). Lateral distribution of thickness and confinement energies for electrons and holes, as well as energy levels of QWR subbands (Kapon 1994).

The tapered QWL is represented by the 2D potential distribution *V(x, y)*. The QWR subbands in this structure can be found by solving the 2D Schroedinger equation

$$\left[-\frac{\hbar^2}{2m^*}\left(\frac{\partial^2}{\partial x^2}+\frac{\partial^2}{\partial y^2}\right)+V(x,y)\right]\psi(x,y)=E\psi(x,y) \qquad (2.9)$$

Here z is the QWR axial direction, x is the growth direction, as indicated in fig. 2.2. For the tapered quantum well, the potential variation in the lateral (y) direction is usually much

slower than in the transverse (x) direction. Thus this 2D equation can be approximated by the two coupled 1D Schroedinger equations (Kapon 1989a, 1994):

$$\left[-\frac{\hbar^2}{2m^*}\frac{\partial^2}{\partial x^2}+V_y(x)\right]\chi_y(x)=E_{conf}(y)\chi_y(y) \tag{2.10}$$

$$\left[-\frac{\hbar^2}{2m^*}\frac{d^2}{dy^2}+E_{conf}(y)\right]\varphi(y)=E\varphi(y) \tag{2.11}$$

where $\psi(x,y)\approx\chi_y(x)\varphi(y)$, χ_y is a slowly varying function of y, and $V_y(x)$ is the 1D potential distribution in the transverse direction at each lateral position y. In this approximation, the 1D transverse problem (equation 2.10), the Schroedinger equation for a quantum well is first solved for each carrier type as a function of QWL thickness distribution $t(y)$. This yields the effective quantum well band edge energy distributions $E_{conf}^{c,v}(y)$. These energy distributions serve as the QWR lateral potential wells providing lateral quantum confinements. Solving for the eigenstates of these lateral potential wells finally yields the lateral wavefunctions and subband energies. Usually, for a crescent-shaped QWR, the lateral potential wells can be reasonably approximated by parabolic profiles (see fig 2.2(b)),

$$E_{conf}(y)=E_{conf}(0)+\frac{1}{2}py^2 \tag{2.12}$$

where p is a curve fitting constant. Then, the parabolic potentials give harmonic-oscillator-like QWR subband energies of the form

$$E_l=E_{conf}(0)+\hbar\sqrt{p/m^*}(l-1/2),\quad l=1,\ 2,\ \ldots \tag{2.13}$$

where the subband energies are measured with respect to the bulk semiconductor band edge. To represent the lateral dimension of the QWR, the characterization width that describes the lateral energy potential, is named as effective wire width (W_{eff}). In the literature, it is usually defined as the distance between the points where the wavefunction of the fundamental QWR subband decays exponentially (Kapon 1994, Rinaldi 1994).

The above simple model has been widely used to analyze QWRs obtained in V-grooves (Kapon 1989a, 1994, Rinaldi 1994, Maciel 1994). In most cases, valence band mixing is not considered (Kapon 1994), as the mixing is expected to become less important for low-index subbands and/or for wide wires (Rinaldi 1994). The effective masses used in the calculations are bulk values. Even though other sophisticated models have also been used to analyze QWRs with various shapes (Citrin 1990, 1991, Yamauchi 1992, Rinaldi 1993), the above model can conveniently provide estimations on the degree of lateral confinement in terms of subband energy separations. It was found that the first two transitions predicted by the one-dimensional model and a refined model considering a full two-dimensional potential were in good agreement (Rinaldi 1993, 1994). As a matter of fact, good agreements have also been widely reported between calculated results using the model and experimental results (Kapon 1989a, 1994, Rinaldi 1994), indicating the reliability of the simplified model.

The selection rule assumed in the QWR analysis is that transitions are allowed only between conduction and valence subbands that have the same index numbers (Kapon 1989a, 1994, Rinaldi 1994). The transitions are also polarization dependent. Figure 2.3 illustrates the relative band edge transition strength for three orthogonal polarization in four different structures. Obviously, there is no polarization dependence for bulk materials. Also there is no in-plane (xy plane) polarization dependence for a QWL, even though the transition strength for polarization normal to the plane (z direction) is different from the in-plane values for both electron-heavy hole and electron-light hole transitions. However, an in-plane (using QWL notation) polarization dependence for a QWR exists, with the dependence determined by the cross-sectional shape of the QWR. For a QWR with a large cross-sectional aspect-ratio, as shown in fig. 2.3(d)), when a coupling incident or emitted light propagates along z direction, the light should polarize more strongly along the wire direction (y direction) than normal to the wire direction (x direction) for electron-heavy hole

transitions, and vice versa for electron-light hole transitions. This polarization dependence for QWR transitions has been used to verify the existence of lateral quantum confinement (Tsuchiya 1989, Sercel 1991, Sugaya 1993, Pan 1994).

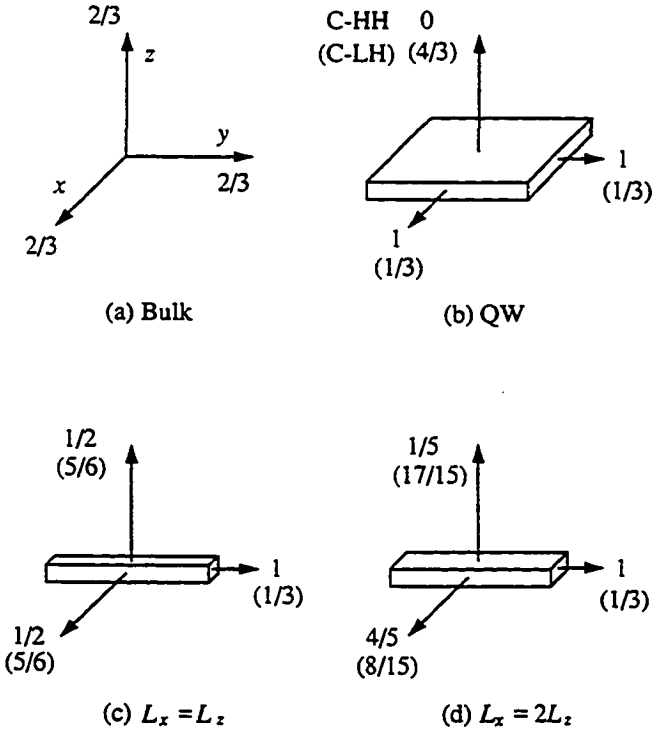

Figure 2.3. Relative strengths of bandedge transition with different polarization for various quantum confinement structures (Corzine 1994)

Various crescent-shaped QWRs have been obtained by epitaxial growth in V-grooves, with different degrees of lateral quantum confinement. Among them, GaAs/AlGaAs QWRs have been most studied. In this type of QWR, subband separations of 21.7, 3.9 and 16.7 meV for electrons, heavy holes and light holes, respectively, and an effective width of 16nm, were reported by Kapon *et al* .(1992b). GaAs/AlGaAs QWRs

grown on V-groove gratings by Rinaldi *et al.*. (1994) also exhibited similar values. However, InGaAs/GaAs/AlGaAs QWRs reported by either Walter *et al.* (1993) or Tiwari *et al.* (1994) had electron subband separations of only a few meV. Crescent-shaped QWRs were also achieved in the GaAs/GaAsP and the GaAs/AlAs systems, but no estimations on subband separations have been offered (Pan 1994, Shen 1993).

2.4. Quantum Wire Laser Structures

As discussed before, the most important application for QWRs is to the laser. To actualize a laser structure, both optical confinement and lateral electrical confinement are required in the structure. Ion implantation and masking techniques have been used to realize the lateral electrical confinement (Kapon 1989a, 1994, Tiwari 1994). Also, 2-dimensional optical confinement is easily achieved in a longitudinal QWR laser configuration (with laser cavity along the wire-direction) simply by the nonplanarity of the V-shaped structure (Kapon 1992c); i.e., the lateral optical confinement is mainly due to the sharp bending of layers in the V-groove bottom. However, the tapering of waveguiding layers along sidewalls also contributes to the lateral confinement. Thus, 2D optical waveguiding can be included just by growing a QWL laser-like structure inside a V-groove, which has almost the same layer structure as a standard QWL laser but with layer thicknesses adjusted to consider enhanced growth at V-groove bottom and with the position of the active region adjusted to obtain an optimal optical confinement factor (Kapon 1992c).

GaAs/AlGaAs lasers with a single QWR (Kapon 1989a, b) or vertically stacked multiple-QWR (Simhony 1991) active regions usually have layer structures: n-$Al_yGa_{1-y}As$ / $Al_xGa_{1-x}As$ / GaAs QWL / $Al_xGa_{1-x}As$ / p-$Al_yGa_{1-y}As$ / p^+-GaAs. A threshold current of 0.6 mA was achieved at room temperature in multiple-QWR GaAs/AlGaAs lasers with high-reflection facet coating (Simhony 1991). A similar structure, but consisting of 3 InGaAs/GaAs QWRs, was reported to have an even lower threshold current, 0.2 mA, even

without facet coating (Tiwari 1994). Although no working QWR lasers have been achieved in the InP-based system, based on the above discussion, it should be possible to fabricate a QWR laser with a layer structure as simple as: n-InP / InGaAsP / InGaAs(P) QWL / InGaAsP / p-InP. Here, InGaAsP layers are used as waveguiding layers.

CHAPTER 3. EPITAXY ON PATTERNED SUBSTRATES AND ITS APPLICATION TO QUANTUM WIRE FABRICATION

3.1. Epitaxy Techniques

Modern semiconductor structures, such as quantum wells, require precise control of layer composition, thickness and interface sharpness. These requirements led to the development of advanced epitaxy techniques, including MBE and metalorganic chemical vapor deposition (MOCVD).

MBE involves a process whereby atomic or molecular beams, generated by evaporation of elements, impinge onto a heated substrate, where, under suitable conditions, they condense epitaxially. Although some early studies on beam-epitaxy had been carried out (Gunther 1958, Davey 1968, Arthur 1968 and 1969), MBE was demonstrated as a practical crystal growth technique in the early 1970's by Cho, after a series of system modifications including: substrate heating; increasing the capacity of the sources; precisely controlling the source temperature; and introducing cryopanels to reduce unwanted impurities (Cho 1970, 1971a,b). Figure 3.1 schematically depicts a typical MBE system. The system requires a high vacuum environment so that atoms or molecules can travel to the substrate from the sources without colliding with other atoms or molecules. With the implementation of a fast acting mechanical shutter in the path of each atomic or molecular beam, the technique has the capability of making extremely abrupt interfaces in heterostructures by quickly switching the fluxes on and off. Through control of the fluxes from the different sources, both layer thickness and composition can be accurately controlled. The ultra-high vacuum environment also allows in-situ substrate preparation, sample surface analysis and growth process monitoring, in addition to the background impurity reduction.

Conventional MBE uses elemental sources, with atomic or molecular beams being generated from effusion cells that contain individual elements. Other variants of MBE are gas source MBE (GSMBE) and metal-organic MBE (MOMBE). GSMBE is also called hydride-source MBE, where, in the growth of III-V semiconductors, the group III species are generated from elemental sources, and the group V species from volatile or gaseous compounds using a gas flow manifold. MOMBE, also known as chemical beam epitaxy (CBE), uses all volatile and gaseous compounds for both group III and group V species. All three techniques are currently used and may have their own advantages over others depending on the materials systems (Panish 1989).

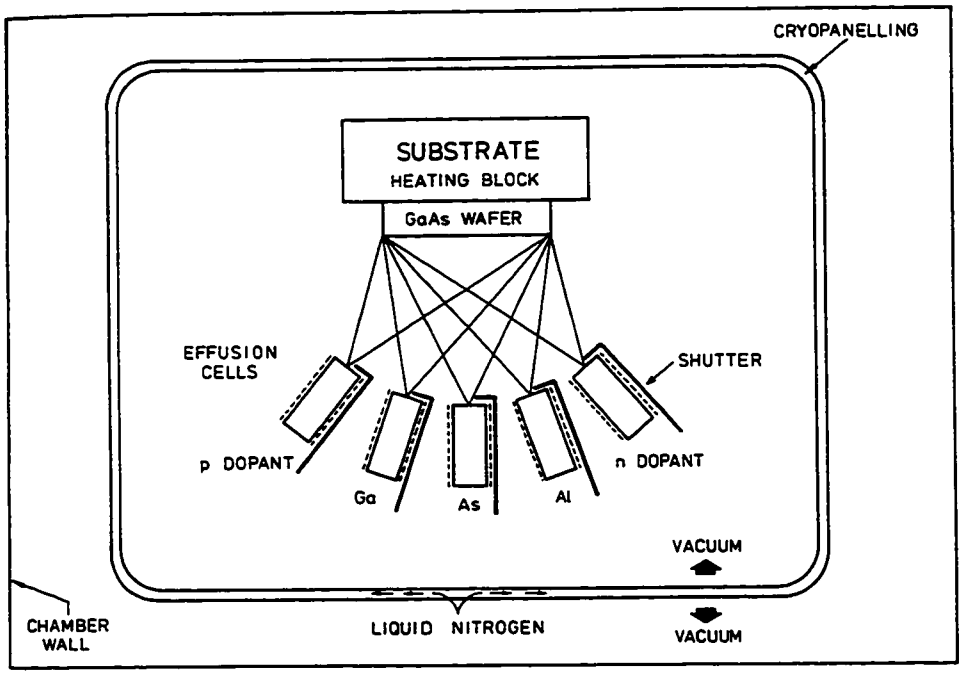

Figure 3.1. Schematic diagram of the MBE system for the growth of AlGaAs/GaAs.

MOCVD is also widely used for epitaxy, especially for large-scale production in industry. There are low-pressure and atmospheric-pressure MOCVD systems. Both involve viscous flow, in contrast to the molecular flow used in the MBE process. The vapor of group III metal-organic sources, such as liquid trimethylgallium, is usually transported to the growth chamber using hydrogen gas. It is then pyrolyzed with the group V hydrides at relative high temperature (550-700 °C) to form an epitaxial layer on a heated substrate. The chemical reaction is irreversible so that control of the growth rate is readily achieved by adjusting the hydrogen gas flow through the liquid sources. Growth rates are typically 1-10 μm/h and layers can be as thin as 2-3 nm. The abruptness of interfaces between different layers is critically dependent on the gas handling system (Grange 1985).

MBE offers some advantages over MOCVD even though MOCVD has higher production capabilities. The reduced growth temperatures used in MBE cause less bulk diffusion at abrupt material interfaces, which is particularly important with some dopant species. Ultra high vacuum (UHV) makes some in-situ analysis on films possible, as previously mentioned. Also, MBE is more suitable for the growth of some complex structures, particularly very thin layers. The slow growth rate of about 1 monolayer per second, or less, easily permits the growth of layers with nanometer thickness which, as seen later, is used in this work.

3.2. McMaster GSMBE System

A GSMBE system is employed at McMaster University for the growth of InGaAsP/InP-based and InGaP/GaAs-based materials and device structures. Ga and In beams are derived from the molten elements contained in effusion cells; P_2 and As_2 are generated from cracking of PH_3 and AsH_3 gases in a cracker cell containing a rhenium catalyst heated to about 1000 °C. Dopant sources are also produced using effusion cells,

with silicon used for n-type doping and beryllium used for p-type doping.

The beam flux of group III or dopant species is controlled by the cell temperature, through the appropriate vapor pressure-temperature relationship. The flux of the group V species is determined simply by controlling the gas flow rate. Under normal growth conditions, the group V flux is greater than the group III flux to compensate for the higher equilibrium group V vapour pressure. The group III species have unity sticking coefficients under normal growth conditions, while the condensation of group V species depends on the arrival rate of the group III species enabling stoichiometric growth. Any excess group V species will desorb. Thus, the growth rate is simply determined by the total arrival rate of group III species and the composition of the grown layer with respect to the group III elements is simply determined by the ratio of their corresponding fluxes. By contrast, the composition of the layer with respect to the group V elements, e.g. As vs. P, is determined by both the ratio of corresponding fluxes and their different incorporation probabilities, as discussed later. Unity sticking coefficients are also assumed for the two dopant species.

The substrate is usually held at a suitable temperature during growth, typically 450 °C for InP, which not only allows the condensation of III-V compound but also ensures adequate surface mobility for epitaxy and which allows the excess group V component to reevaporate from the substrate surfaces. Usually, the substrate temperature is optimized to achieve the desired materials quality and structures with consideration of kinetic factors such as surface migration of adatoms. In this work, MBE growths have been performed with substrate temperatures between 400 °C and 510 °C.

As substrate preparation is an important step for successful MBE growth, an electron cyclotron resonance (ECR) H-plasma source is attached to the MBE system to perform in-situ substrate cleaning prior to MBE growth. Before loading wafers into vacuum, samples are exposed to a UV-ozone oxidation for 2 minutes to remove residual carbon contamination and produce a sacrificial oxide layer. The sample is then heated to

250 °C for 1 hr in vacuum to desorb any water vapour. Subsequently, the sample is transferred to the growth chamber, heated to 450 °C and exposed to a simultaneous P_2 flux and an ECR H-plasma for 5 minutes to remove the oxide layer. This technique is routinely used at McMaster as an alternative to conventional thermal desorption methods requiring higher temperatures.

At McMaster, a wafer with a 15 mm x 15 mm square shape is directly mounted onto a sample holder with Mo clips. Small samples are In-bonded onto a supporting n-type InP wafer. Wafers are rotated at 10 -30 rpm during growth to minimize any growth nonuniformity originating from geometrical factors, such as beam alignment and flux distributions.

Finally, the McMaster MBE system is connected with an ECR-CVD system through a vacuum link.

3.3. Applications of Epitaxy on Patterned Substrates

Epitaxy on a planar substrate can readily produce semiconductor heterojunctions and vertical (one-dimensional) carrier confinement which have been extensively applied to device fabrication such as quantum well lasers. However, two-dimensional or three-dimensional patterning offers additional device potential. To achieve this, without requiring elaborate processing techniques, presents new challenges for crystal growth. Devices such as QWR lasers and integrated laser-modulator structures require either compositional or quantum-well thickness variations laterally across the substrates. Post-growth techniques, such as etching and regrowth, may achieve some of these objectives. However, in-situ formation of two-dimensional patterning is attractive because it may yield passivated and defect-free interfaces. Such interfaces are usually essential for producing structures suitable for studying the intrinsic properties of layered materials and for application in useful devices. In-situ lateral-patterning techniques which have been studied include: growth on

patterned substrates (Tsang 1977, Kapon 1994); selective growth with dielectric masks (Koshiba 1994, Lammert 1995, 1996); and growth on vicinal substrates (Petroff 1994). Selective growth with dielectric masks can be used to change the composition of layered materials using different mask widths. This has been demonstrated in integrated laser-modulator and detector circuits (Lammert 1995, 1996). Faceting with characteristic crystallographic planes, common in such a selective growth technique, can also result in nano-features such as quantum wires on the ridge top (Koshiba 1994). However, the ridge-type geometry makes the application of the QWRs to devices such as lasers very difficult. Growth on vicinal substrates can lead to lateral modulation in the materials' bandgap with a typical periodicity in the sub-10 nm regime, which in principle can be used for the growth of quantum wire superlattices (Petroff 1994). However, controlling the size and compositional uniformity, and relative single quantum wire effects, are difficult to be achieve with this technique.

In contrast with the above two techniques, growth on a patterned substrate, which has received extensive attention, offers the ability both to introduce lateral variation in the materials composition and quantum well thickness such that novel structures such as QWR lasers can be fabricated. As the first step, substrates are patterned with conventional lithographic and etching techniques, using preferential wet etching (Hou 1987, 1988) or dry etching (Tsang 1994), to achieve surface profiles characterized by distinct crystalline facets. Subsequent growth on these substrates may result in various effects. The simplest case is when migration of adatoms can be ignored. In such a case, the growth is simply conformal. Fig. 3.2 schematically shows a quantum well structure, for example a GaAs/AlGaAs quantum well grown conformally on a substrate patterned with trenches. As seen in the figure, the thickness of the quantum well varies spatially, simply because of the different projected flux on different surfaces. The variation in quantum-well thicknesses will give different electron and hole confinement energy levels in different regions, which

will result in different emission wavelengths, with a shorter emission wavelength from the thinner regions of the quantum well.

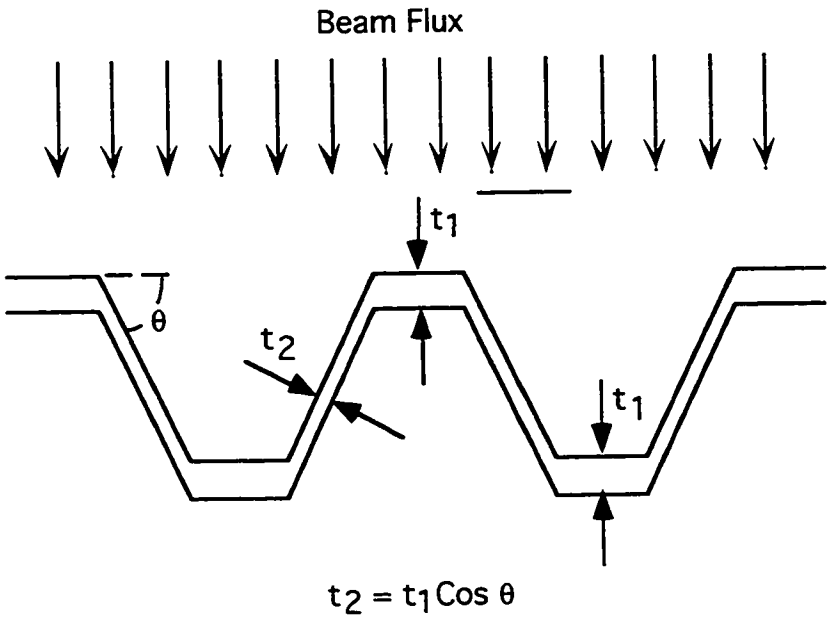

Figure 3.2. A quantum well grown conformally on a trenched substrate.

In most cases, the surface profile will be further modified when preferential migration of adatoms exists. The surface profile evolution will not only change the distributions of physical sizes such as layer thicknesses, but will also be accompanied by compositional variations, as discussed below. Figure 3.3(a) shows a possible result from an InGaAs/InP quantum well structure grown on a mesa. Due to adatom migration from the sidewalls to the planar region, the quantum-well thickness at the mesa top is larger than that on the non-patterned region. Moreover, due to a differential migration of In over Ga, the composition of the InGaAs quantum layer at the mesa top is In rich. Therefore, the emission wavelength of the top quantum well will be red shifted relative to that on the sidewalls and the non-patterned region. The amount of wavelength shift will depend on the

width of the mesa top as long as it is less than the migration length of In adatoms. If a substrate is patterned with different mesa widths on a line, an integrated laser-modulator structure can be formed (Pratt 1994) (fig. 3.3b), where the modulator has a wider bandgap than the laser.

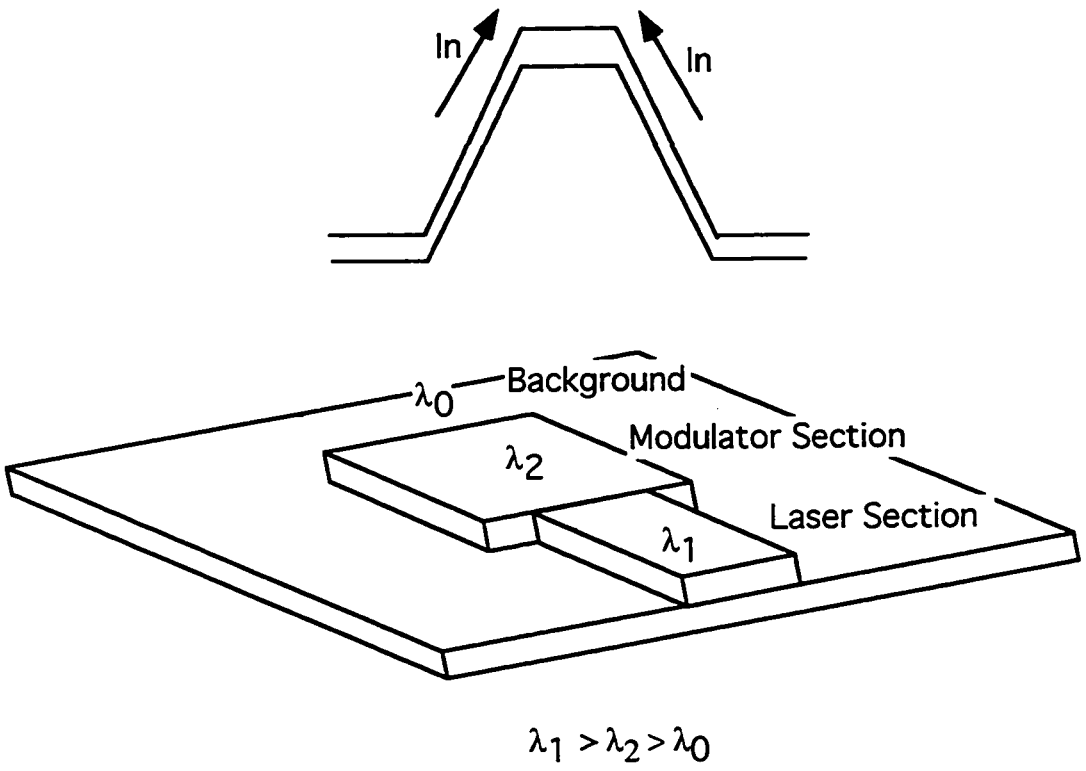

Figure 3.3. a). (top). Cross-sectional diagram of a mesa showing adatom migration and quantum well thickness variation; b). (bottom). A schematic integrated laser-modulator structure grown on a patterned substrate.

3.4. Quantum Wires Fabricated by Growth on V-groove Patterned Substrates

One of the important applications of epitaxy on patterned substrates, in addition to integrated laser-modulator structures, is the fabrication of quantum wires in V-grooves. Figure 3.4 shows a schematic of a quantum well structure grown onto a V-groove with a

sharp bottom. Due to adatom migration on sidewalls and higher incorporation probability at the bottom, as well as the V-shaped geometry, the quantum-well thickness increases significantly in the bottom of the V-groove. As discussed in the previous chapter, a significant variation in quantum-well thickness in a small region will result in lateral carrier confinement; that is, the formation of a quantum wire.

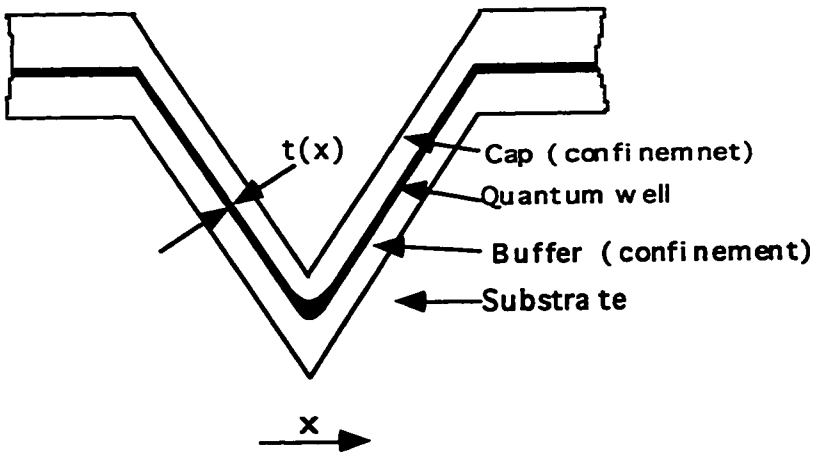

Figure 3.4. A schematic diagram showing a quantum wire formed inside a V-groove.

Both MOCVD and MBE have been used to fabricate various types of QWRs on V-groove patterned substrates. The first reported QWRs grown in V-grooves were GaAs/AlGaAs single wires grown using MOCVD on (100) GaAs substrates patterned with [0$\bar{1}$1] oriented V-grooves (Bhat 1988, Kapon 1989a, b). Vertically stacked arrays of GaAs/AlGaAs crescent -shaped QWRs were subsequently grown (Simhony 1991, Christen 1992). InGaAs/GaAs/AlGaAs strained QWRs were also obtained on 0.25 μm pitch periodic grating substrates using MOCVD (Walther 1993).

MBE has also been applied to the growth on V-grooved substrates. GaAs/AlAs QWRs were obtained using MBE (Shen 1993) after extensive work to establish the MBE

growth behaviour of Al(Ga)As on GaAs V-grooves with (111)A sidewalls. As mentioned before, by comparison to the GaAs-based system, only a few studies have been done on the InP-based system using MBE (Bulitka 1993) and using MOCVD (Galeuchet 1988, Bhat 1990). No QWRs have been reported in the InP material system by either MBE or MOCVD.

In this work, a GSMBE system is employed for extensive studies on QWR growth aiming at an InP-based QWR laser structure.

Successful implementation of a quantum wire laser is dependent on the growth behaviour of all constituent layers inside a V-groove. In addition to the quantum well layers, other layers including the buffer layer, barrier layers and waveguiding layers have to be grown in ways to achieve appropriate geometry, composition and quality. All this requires good control of epitaxial growth on patterned substrates.

3.5. Issues of MBE Growth on Patterned Substrates

The most important issues of MBE growth on patterned substrates include adatom migration, group V incorporation and strained-layer growth. However, to understand these issues, MBE growth on different substrate surfaces which can be contained on a pattern etched substrate, as well as different growth modes, will be briefly discussed.

3.5.1. MBE growth on different types of planar substrates and different growth modes

(100)-oriented substrates are most commonly used for MBE growth. However, an etch patterned substrate may contain (111), (011) or other high-index surfaces, in addition to (100) top and bottom surfaces. The growth behaviour on these non-(100) surfaces may be quite different from that on a (100) surface because of the atom terminations of different surface planes.

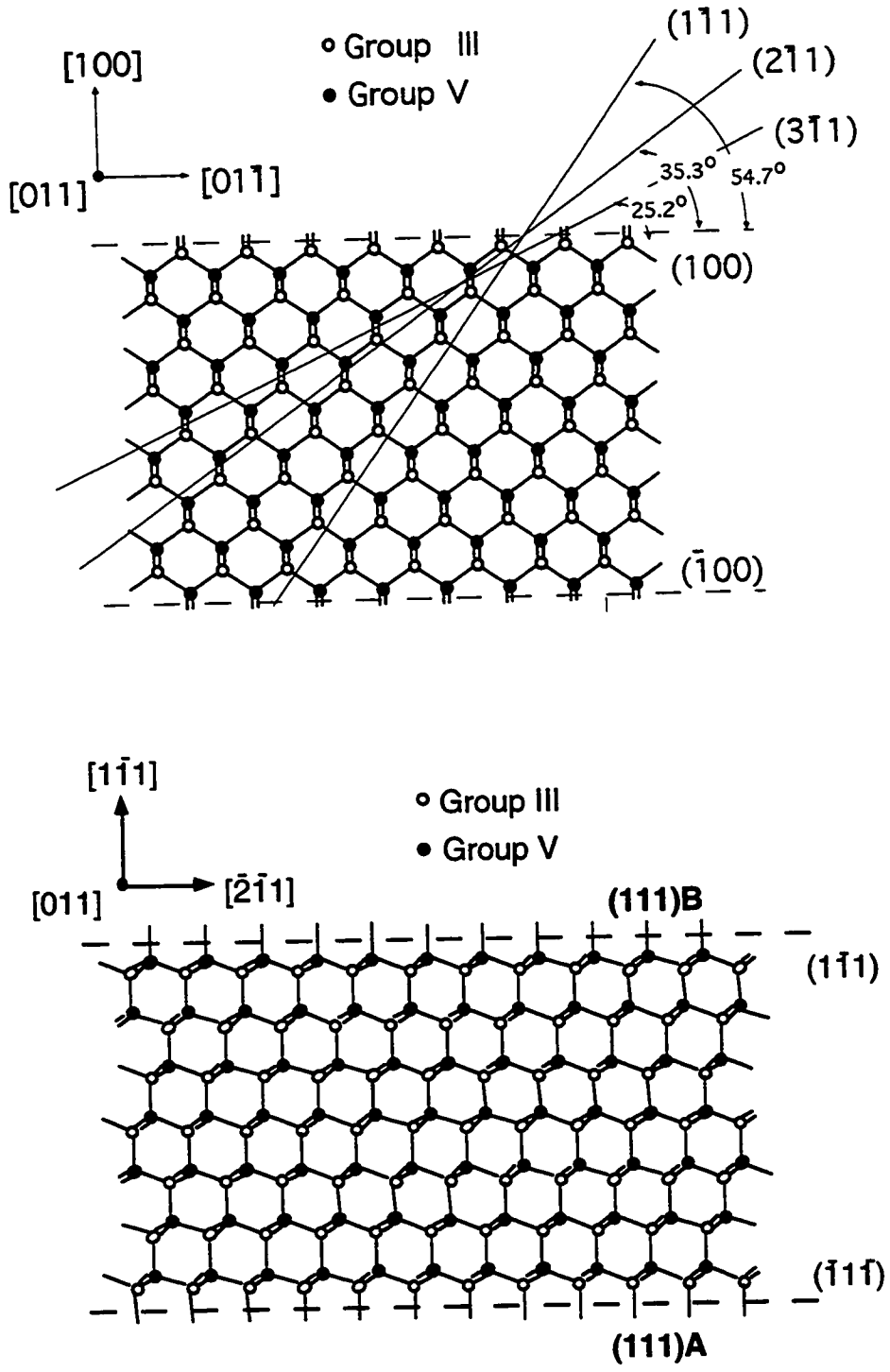

Figure 3.5. Atomic structure of a III-V crystal: a) (top). with (100) surfaces, b) (bottom). with (111) surfaces, viewed along the [011] direction.

Figure 3.5 shows the atomic arrangement of a III-V crystal. As shown in figure 3.5(a), an unreconstructed (100) surface always has double dangling bonds. It can be terminated by either group III or group V atoms depending on growth conditions. However, the surface bond directions of group III atoms are rotated by 90^{o} relative to those of group V atoms. Also indicated in the figure are (111), (211) and (311) planes. Surfaces comprising these planes are further defined as A-type or B-type depending on the terminating atomic species. Figure 3.5(b) exhibits a crystal with (111) surfaces in more detail. A (111) surface can be terminated completely with either group III or group V atoms, labeled as (111)A or (111)B surfaces, respectively. All (111) surfaces have only single dangling bonds. Surfaces between (100) and (111), i.e. (h11) surfaces, can be considered as consisting of fractional (100) and (111) surfaces, with the (211) surface having twice as many single dangling bonds, (111)-like, as double dangling bonds, (100)-like, and the (311) surface having equal amounts of single and double dangling bonds. Among these surfaces, a surface containing (111)A fractions is called A-type, while a surface with (111)B fractions is called B-type.

Growth studies have been carried out on (111) type substrates, while considerably fewer growth studies have been done on other planar non-(100) substrates. MBE growth on a (111) surface has been found to be rather difficult (Cho 1970, Chen 1991, Hou 1993). As reported a number of years ago (Cho 1970), epilayers tend to form pyramids and twins due to more than one possible nucleation site and growth sequence. To solve these problems, methods have been employed which involve enhancing the surface migration length of adatoms (Imamoto 1989) and changing growth modes using vicinal substrates (Hou 1993).

Depending on substrate and growth conditions, as well as the composition of the epitaxial materials, several growth modes can occur. Growth modes are usually classified as layer-by-layer growth (Frank-van der Merwe), 3D island growth mode (Volmer-Weber)

and layer-then-island growth mode (Stranski-Krastanov). Usually the 3D growth mode or Stranski-Krastanov growth mode is not desired except that it has recently been used to grow quantum dots in a lattice-mismatched materials system (Notzel 1996). The layer-by-layer growth mode is usually preferred to ensure materials and interface quality. This growth mode can be further divided into two types: a 2D nucleation mode and a step flow mode. While the 2D nucleation mode is normally seen in MBE growth on planar (100) substrates, a step flow mode can be used eliminate problems involving twins and pyramids that occur on (111) substrates. To achieve step flow growth, vicinal substrates are used (Hou 1993). For MBE growth on patterned substrates, the step flow mode is highly possible because steps may be present on the etched surfaces due to the deviation of surface profiles away from ideal crystal planes before or during growth.

3.5.2. Group III adatom migration

When a group III atom or a group V molecule absorb onto a substrate surface, it is initially in a mobile, weakly bound physisorbed state, in which the atom or molecule is called an adatom. It will either incorporate or desorb after moving around for a certain life-time. Three terms have been used to describe the behaviour of the adatom: surface diffusion coefficient (D); life-time (τ); and migration length (λ). In fact, the migration length is just a function of the diffusion coefficient and life-time ($\lambda = \sqrt{D\,\tau}$). Usually it is the migration length that is used to represent the behaviour of adatoms, which is a constant for a certain crystal plane. It seems that the diffusion lengths of group III adatoms increase with their atomic numbers, even though no explanation has yet been reported. Typically, migration lengths on a (100) surface for Al, Ga and In are < 1 μm, 1-5 μm, and 3-30 μm respectively (Kapon, 1994). The migration length also depends on growth and surface conditions (Shen 1994). Generally, the surface migration length increases with increasing substrate temperature, as well as with decreasing V/III flux ratio. The migration length also depends

on the migration direction and the surface planes. Under similar growth conditions, surface migration lengths along the [011] direction are considerably smaller than along the $[0\bar{1}1]$ direction (Kapon 1994, Hata 1990). Compared to those on (100) surfaces, migration lengths on non-(100) planes should be different, but little data is available.

For growth on patterned substrates, usually there exists an adatom concentration gradient or a spatial variation in surface energy. In such a case, there will be a net flow of adatoms from one region to another. This phenomenon plays an important role in the determination of layer profiles and compositions. To study the migration of group III adatoms, rate equations have been widely used (Ohtsuka 1988, Shen 1994).

The general form of the rate equation for a group III species is

$$\frac{dN_{III}}{dt} = J_{III} - \frac{N_{III}}{\tau_{III}} + D_{III}\frac{\mathrm{d}^2 N_{III}}{\mathrm{d}x^2} \qquad 3.1$$

where J_{III} is the group III net vapor phase flux, N_{III} is the surface concentration of the group III adatom and dN_{III}/dt is total net flux or the change rate of the adatom surface concentration, τ_{III}, is the incorporation lifetime, D_{III} is the surface diffusion coefficient, and x is the in-plane coordinate upon which J_{III}, N_{III}, τ_{III}, and D_{III} depend.

The first term at the right hand side of the equation, J_{III} , is the incident group III flux if desorption of group III adatoms is ignored, which is usually reasonable unless the growth temperature is too high. The second term represents the local incorporation rate or local growth rate, while the third term represents the lateral diffusion flux. Under a steady state, the net flux (dN_{III}/dt) must be zero, so that the rate equation becomes

$$\frac{dN_{III}}{dt} = J_{III} - \frac{N_{III}}{\tau_{III}} + D_{III}\frac{\mathrm{d}^2 N_{III}}{\mathrm{d}x^2} = 0 \qquad 3.2$$

Since the incorporation life-time and the diffusion coefficient are constants for a given crystal plane, the general solution will be

$$\frac{N_{III}}{\tau_{III}} = J_{III} + c_1 e^{\frac{x}{\sqrt{\lambda_{III}}}} + c_2 e^{\frac{x}{\sqrt{\lambda_{III}}}} \qquad 3.3$$

where $\lambda_{III} = \sqrt{D_{III}\tau_{III}}$, is called the migration length, and c_1 and c_2 are constants which depend on boundary conditions. On a planar substrate where the adatom concentration is uniform, c_1 and c_2 become zero and the incorporation rate will simply be equal to the incoming flux. For a mesa-type substrate (fig. 3.6), a net lateral flux can be assumed from a sidewall to the mesa top. When the width of a mesa top is much larger than the migration length , that is, the mesa top can be treated as a semi-infinite plane, then equation 3.3 will become

$$\frac{N_{III}}{\tau_{III}} = J_{III} + c_1 e^{-\frac{x}{\sqrt{\lambda_{III}}}} \qquad 3.4$$

With the understanding that the group III incorporation rate is proportional to the growth rate, for a binary compound, the equation indicates that the growth rate distribution on the mesa top follows an exponential profile. Once the growth rate distribution is measured experimentally by such techniques as microprobe RHEED (Hata 1990), cross-sectional SEM or cross-sectional TEM (Ohtsuka 1988), an exponential curve fitting will yield the migration length. For a semiconductor with two or more group III elements such as InGaAs, each group III species will have a different incorporation life-time (distribution) and diffusion coefficient. The effective incorporation rate distribution for each given group III adatom can be determined through the measurement of composition and thickness variation (Bulitka 1993a). Then the migration length of each adatom can be determined using the curve fitting. Reversibly, estimated migration lengths can be used to predict the composition profile of the ternary with two group III components.

However, in the case of some types of patterned substrates, such as V-grooves, the situation is much more complicated. A surface such as that of a V-groove sidewall, usually deviates away from an ideal crystalline plane with slopes changing continuously along the sidewall. In other words, steps and kinks are introduced non-uniformly along the sidewall. Therefore, the incorporation life-time, which depends on the surface profile, will not be a

constant across the surface. With more complicated boundary conditions, equation 3.2 cannot be simplified to equation 3.3 or equation 3.4 . Nevertheless, equation 3.2 can still be handled with numerical methods, with the understanding that the migration length is now a function of x, the specific plane and intersections between planes. One difficulty involved in using equation 3.2 for modeling is lack of data on τ_{III} and D_{III}. As mentioned before, migration lengths can usually be determined through measurements of composition or thickness profiles using ex-situ techniques (Bulitka 1993a, b, Shen 1994a) or measurements of growth-rate profiles using a RHEED microprobe technique (Hata 1990). Observing the transition of growth modes between a 2D nucleation mode to a step flow mode on vicinal surfaces using RHEED oscillations has also been used to measure migration lengths (Neave 1985). However, obtaining incorporation life-times and the diffusion coefficients is much more difficult. Assumptions are frequently used: in Shen's modeling (1994a), a constant diffusion coefficient was chosen quite arbitrarily.

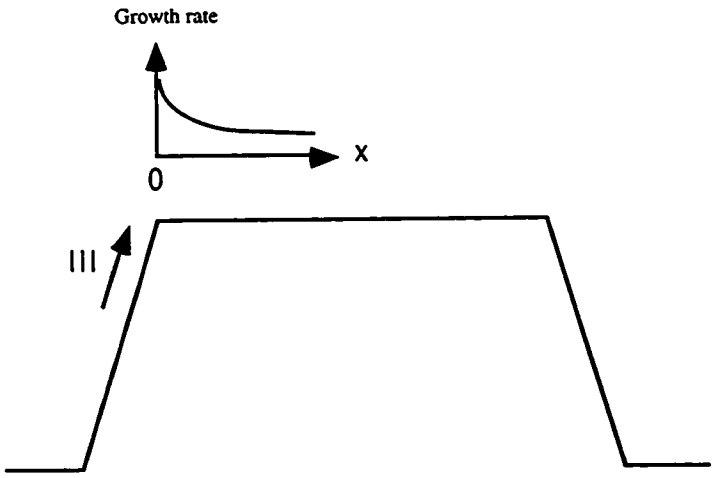

Figure 3.6. Growth rate variation on a mesa top.

In MBE growth on a patterned substrate, especially the growth of a thick layer, the surface profile may evolve throughout the growth. Consideration of the surface profile

evolution makes the solution of equation 3.2 even more complicated. Ohtsuka (1988) tried to simulate the surface profile evolution with a slightly different approach; that is, using a different form of the diffusion equation. He introduced a coordinate s to represent a length along the surface profile. He also modified the differential equation into difference equations which can be used at sharp faceted edges. Then, with the consideration of the variation of the life-time on different planes, as well as desorption of the deposited species, the model was able to qualitatively simulate the growth morphology in multifaceted systems. However, application of the model required data on the dependence of the growth rate on the slope of a surface profile as well as the desorption migration length. These requirements significantly limit the applicability of the model (Madhukar 1993).

Up to now, only phenomenological approaches to adatom migration have been used. Some fundamental issues such as migration anisotropy and the mechanism that drives the interfacet migration are not well understood. Madhukar (1993) believes that the directionality of interfacet migration is determined by the relative balance of the chemical potential gradient arising from the difference in the vapor flux on different faces and the ledge-ledge interaction energies on sidewalls. Molecular dynamics simulations (Choi 1987) show that ledge-ledge interaction is repulsive for a ridge lying along $[01\bar{1}]$ direction, which drives adatoms to migrate opposite to the direction of adatom density gradient, and the interaction is attractive for a ridge lying along a [011] direction, which drives adatoms to migrate in the same direction as the adatom density gradient. However, the ledge-ledge interaction cannot explain some of the experimental observations (Shen 1994a). Other factors, such as surface energies of different planes, bond density and step or kink density should also be considered (Finnie 1995, Asai 1987, Ohtsuka 1988). It is believed that all of these factors could be represented by a spatially-variable incorporation life-time in the phenomenological rate equation.

Another issue related to surface profile evolution is faceting. On the one hand, it

was found that growth on [01$\bar{1}$] -oriented grooves leads to evolution of facets such as (111)A and (311)A (Tsang 1977, Bhat 1988, Bulitka 1993); on the other hand, growth on [011]-oriented grooves is characterized by formation of (100) flat bottoms, with continually-changing slopes, i.e., no facetting, on the sidewalls (Smith 1985, Bulitka 1993a). In particular, resharpening to the original V-groove facet, which is very useful for QWR growth, has been found in AlGaAs grown by MOCVD (Kapon 1994) and AlAs grown by MBE (Shen 1993) on [01$\bar{1}$]-oriented grooves. Generically speaking, faceting, including resharpening, is related to the reduction of surface energy. Other than this, however, our understanding on the issue is only limited to some experimental observations.

Obviously, fundamental modeling is desired to understand the growth behaviour on patterned substrates. However, no atomistic simulations have yet been reported in the literature, even though Monte Carlo simulations, which are believed to be the only practical way to deal with issues such as interfacet migration, have been underway at the University of Southern California since before 1993 (Madhukar 1993). The slow progress is related to the complexity of the issues involved.

3.5.3. Migration and incorporation of group V species

In the studies of epitaxy on patterned substrates, the behaviour of group V species, including migration and incorporation, has received little attention. This is because (1). under normal growth conditions with a V/III flux ratio being much larger than unity, lateral flux originating from the migration of group V species is negligible compared to the flux from the vapor phase; (2). most studies which have been carried out in growth on patterned substrates involve only one group V component such as As in the GaAs-based materials system. However, when growth is performed with the V/III flux ratio close to unity, the migration of group V species may become important. Another complication arises when the

epilayer has two group V components, because the incorporation probabilities of the two group V components may vary spatially. Since this work involves growth under low V/III flux ratios and growth of InGaAsP quaternary layers on V-groove patterned substrates as well, the migration behaviour of group V species will be discussed first, and the general incorporation behavior of As and P in an InGaAsP layer will be addressed later.

The rate equations, with the diffusion terms included, can also be applied to group V species. Similar to that of the group III species, the steady state rate equation of group V species is

$$\frac{dN_v}{dt} = J_v - \frac{N_v}{\tau_{cv}} - \frac{N_v}{\tau_{vv}} + D_v \frac{\mathrm{d}^2 N_v}{\mathrm{d}x^2} = 0 \qquad 3.5$$

where the subscripts v denote the group V species, τ_{cv} and τ_{vv} are the incorporation lifetime and the desorption lifetime of group V species respectively, i.e., a desorption term is involved in the equation.

Obviously, the application of equation 3.5 will depend on the understanding of the desorption lifetime and the diffusion coefficient, as well as the incorporation lifetime. The desorption behaviour of group V species received much attention at the early stage of MBE development. Beam modulation and mass spectrometric detection (Arthur 1968, Foxon 1975) was used to investigate the desorption behaviour of As from GaAs. It was found that the desorption lifetime of either As_2 (Arthur 1969) or As_4 (Foxon 1975) not only decreased exponentially with the substrate temperature, but also increased with the surface concentration of Ga on a surface which can be changed with a change in the flux rate. In other words, the desorption lifetime depends heavily on the MBE growth conditions such as growth temperature, V/III flux ratio and growth rate. Partially because of this complicated dependence of the desorption behaviour on growth conditions and the difficulty in investigating it, little work on the absorption behaviour has been done since the early 1980's. Another reason may be that the initial understanding of growth mechanisms

achieved by these early studies already enables us to grow high quality materials and structures. Hence, existing literature supplies little data on parameters such as the desorption lifetimes of group V species under different growth conditions and different substrate orientations. In particular, no work appears to have been carried out on the desorption lifetime of P_2 (Foxon 1983), even though the desorption lifetime of P_4 on GaP has been measured by Foxon (1980). Also there appears to be no information available on the surface diffusion coefficients of group V species. All these factors make a quantitative modeling of the migration behaviour of group V species, using equation 3.5, quite difficult.

Because the incorporation probabilities of group V species are not unity, the group V composition of a material with more than one group V component is much more difficult to determine than the group III composition. Different components such as As and P have different incorporation probabilities at normal growth temperatures and this is further complicated by the growth conditions such as the total group V over-pressure and the associated under- or over-pressure of each component. The result is a composition of the group V components in the solid, such as InGaAsP, different from that in the incident flux.

For GSMBE growth of an $In_{1-x}Ga_xAs_yP_{1-y}$ layer, the fraction of As_2 (Y) in the vapor phase is represented by

$$Y = \frac{\phi_{As_2}}{\phi_{As_2} + \phi_{P_2}} \qquad 3.6$$

where the Φ_i denotes the dimer flux incident on the InGaAsP surface. If incorporation probabilities of As_2 and P_2 are c_{As2} and c_{P2} respectively, then the group V composition in the solid is related to the vapor flux composition by the following relationship:

$$\frac{y}{1-y} = \frac{c_{As2}\phi_{As2}}{c_{P2}\phi_{P2}} = c_0 \frac{Y}{1-Y} \qquad 3.7$$

where $c_0 = \frac{c_{As2}}{c_{P2}}$ is called the incorporation coefficient.

The incorporation coefficient was originally assumed to be a constant (Panish 1984) with a value larger than a unity, which means a preferential incorporation of As compared to P in the InGaAsP layer. However, more experimental data obtained later on, as well as modeling investigations (LaPierre 1995, Lee 1995), show that the incorporation coefficient is not a constant but varies with the V/III flux ratio, as well as Ga content (LaPierre 1996, Lee 1995). The incorporation coefficient may also depend on the substrate material and substrate surface plane. Incorporation behaviour of InGaAsP on InP substrates with different orientations, (100), (211) and (311) surfaces, but not including (111) surfaces unfortunately, has been studied by LaPierre (1995). It was found that the incorporation coefficient on (h11)B surfaces is slightly higher than that on a (100) surface, while on (h11)A surfaces it is lower. As mentioned before, to our knowledge, no work has been reported about the group V incorporation behavior on patterned substrates. Nevertheless, some experimental results about the incorporation of group V species inside V-grooves will be presented in Chapter 7.

Another issue associated with MBE growth on patterned substrates is related to strain. Strain relaxation can then occur when the thickness of a strained layer exceeds a critical value. While strain will change the physical properties of materials or structures, strain relaxation will generate misfit dislocations. These defects will serve as non-radiative recombination centers and affect the optical and electrical properties of materials and structures. Therefore, the thickness of a strained layer should be kept below its critical thickness to prevent relaxation. For growth on patterned substrates, concern about the relaxation of a strained layer, becomes very important. Even when a nominally lattice matched layer is deposited, the differential migration of group III species and variation of

the group V incorporation coefficients will result in spatial variations in the layer's composition (hence lattice constant) and thickness. Thus, special care has to be taken for ternary and quaternary growths on patterned substrates.

CHAPTER 4. CHARACTERIZATION TECHNIQUES

In this work, the surface morphology, layer morphology, layer composition, defect information, optical properties, etc., of all samples have been examined using various characterization techniques. Their basic principles will be presented and relevant experimental aspects will be included in this chapter.

4.1. Scanning Electron Microscopy

V-grooves used for QWR growth have dimensions about several micrometers wide at the top and less than tens of nanometers at the bottom. In particular, the sharpness at the V-groove bottom is crucial to the formation of a QWR following the epitaxial growth. Also, surface smoothness after growth reveals information about epilayer quality. Therefore, the shape, size, bottom sharpness and surface smoothness of V-grooves, before and after growth, had to be systematically examined in this work. The examination of these features requires high magnification as well as high resolution. These requirements, which cannot be fulfilled with optical microscopes, can be accomplished with a scanning electron microscope (SEM).

SEM is similar to light microscopy, but with electrons used instead of photons. This offers two main advantages: much higher magnification and a much larger depth of field. The electron wavelength (λ_e) depends on electron acceleration voltage (V) as

$$\lambda_e = \frac{12.2}{\sqrt{V}} \text{ (Å)} \qquad 4.1$$

Thus, for an acceleration voltage of 10 kV, the wavelength is 0.12 Å, which is significantly below the range of visible light. Hence the resolution of an SEM is much higher than that of an optical microscope.

An SEM forms its image in an entirely different manner than an optical microscope. In a SEM no true image exists. The image in an SEM is produced by scanning a focused electron beam across the sample and detecting the secondary and/or backscattered electrons. The detected signals are amplified and displayed on a cathode ray tube (CRT) scanned synchronously with the sample beam scan in the SEM. A one-to-one correspondence is thus established between each point on the display and each point on the sample, and the magnification is simply the ratio of the dimension scanned on the CRT to the dimension of scanned sample.

The secondary electron image obtained with a conventional SEM is usually not sensitive to the atomic number, even though strong atomic number contrast has been observed using field-emission SEM (Perovic 1995). The contrast in a conventional SEM image mainly arises from the sample topography. Since secondary electrons are emitted from the top 100 Å or so of the sample surface, when a local surface is tilted at an angle θ from normal to the incident beam direction, the volume for the secondary electron emission (100 Å below the surface) is increased by a factor of $1/\cos\theta$. Then the contrast C, depends on the angle as (Goldstein 1984)

$$C = \tan\theta d\theta \qquad 4.2$$

Thus, the contrast increases with tilt angle. This angle effect is mainly responsible for the 3-dimensional nature of SEM images.

A Philips 515 SEM with a Lanthanum hexaboride (LaB_6) filament has been used in this work. Cross-sectional samples were cleaved and mounted with a slight tilt angle away from the normal direction of the sample stage. The samples were then coated with a thin platinum layer to prevent charging effects. Secondary electron images were taken at various

magnifications using an acceleration voltage of 25 kV. When the sharpness of the V-groove bottoms was examined closely at high magnification (x 80,000), a smaller condenser aperture and a smaller working distance were used.

4.2. Transmission Electron Microscopy

Although the SEM can easily perform examinations on surface morphology at reasonably high magnifications, it cannot be used to examine the microstructure of the as-grown thin QWL structures, nor can it provide information about grown-in defects. In this work, transmission electron microscopy has been used to measure epilayer thickness, to observe the cross-sectional shape of the QWRs and to determine the presence of any extended defects such as dislocations, twins and stacking faults.

TEM uses electrons and a series of electrostatic lenses to magnify the sample. It has extremely high resolution approaching a couple of angstroms. Very thin foil samples, with thicknesses between a few hundred and a few thousand angstroms, are used for the TEM characterization. The transmitted and forward scattered electrons form a diffraction pattern in the back focal plane and a magnified image in an image plane. Image contrast does not depend much on absorption, as it does in optical transmission microscopy, but rather on scattering and diffraction of electrons in the sample (Edington 1976). Images formed using the transmitted electrons are bright-field images and images formed using a specific diffracted beam are dark-field images.

In this work, cross-sectional TEM measurements have been performed. Two cleaved sample bars were placed facing each other with supporting silicon pieces on two sides. This sandwich-like structure was bonded together using Epo Tek H20S silver epoxy. After curing, the block was mechanically thinned to about 150 μm, then cut into a disc of 3 mm diameter using an ultrasound cutter. It was then further thinned and polished with a dimple machine to a thickness of about 50 μm at the center of the disc. After

cleaning, the TEM specimen was sputtered on an ion mill until holes appeared. To prevent damage during the ion milling, such as phosphorus evaporation, the sample was cooled using liquid nitrogen. The final TEM examinations were performed on a Philips CM-12 transmission electron microscope.

4.3. Scanning Transmission Electron Microscopy and X-ray Energy Dispersion Spectrometry

It is required that the spatial variation in the composition of epilayers grown into the V-grooves be evaluated. The usual technique combining double crystal X-ray diffraction and photoluminescence (PL) cannot be used for non-planar structures. Also, scanning techniques, such as cathodoluminescence and scanning PL, have their own limitations in terms of resolution and ability to uniquely identify the composition in a strained quaternary compound without still requiring X-ray diffraction analysis. However, direct micro-compositional analysis can be carried out on a scanning transmission electron microscope (STEM) using X-ray energy dispersive spectrometry (EDS).

In the STEM, an electron beam, with a spot size as small as several angstroms, is rastered across a thin foil TEM sample, while transmitted electrons are detected with an electron detector, producing a high resolution image. The electron beam can also be moved point-by-point or placed at a certain position for other analysis. Compositional analysis can be carried out through detection and energy analysis of characteristic X-rays (William 1984). These characteristic X-rays originate from the ejection of electrons from one of the inner atomic shells through kinetic energy transfer from the incident beam. As electrons from outer shells fill the inner shell vacancy, X-rays of characteristic energies are emitted. These X-rays are labelled according to the electron transitions. For example, X-rays resulting from L shell to K shell transitions are known as K_α X-rays , while L_α X-rays originate from M shell to L shell transitions. The energies of K_α X-rays of the elements P,

Ga and As elements are 2.013, 9.241 and 10.542 keV respectively. The energy of the L_α X-ray of In is 3.286 keV (Loretto 1984). Thus, when the X-ray spectrum of a sample is measured by an energy dispersive spectrometer , the constituent elements can be identified from the characteristic peaks. EDS uses a reverse-biased Li-drifted silicon detector, together with a multichannel analyzer for determining the X-ray energies (William 1984).

From the EDS spectrum the ratios of peak intensities can be used to determine the composition of the sample, since the peak intensities are proportional to the atom density. As proposed by Cliff and Lorimer (1975), a quantitative analysis can be performed using the expression:

$$\frac{C_A}{C_B} = k_{AB}\frac{I_A}{I_B} \qquad 4.3$$

where $C_{A/B}$ is the wt% of elements *A/B* in the analyzed volume, $I_{A/B}$ is the characteristic X-ray intensity above background of elements A/B, and k_{AB} is a proportionality factor, which should be independent of specimen composition and thickness, varying only with operating voltage. The *k*-factor can be calculated, but experimental values determined using standards are preferred. Furthermore, to use equation 4.3 for accurate composition analysis, some corrections are involved. The characteristic X-rays may be absorbed preferentially during their passage out of specimen, or the intensity of one characteristic X-ray line may be enhanced by absorbing other characteristic X-rays, which is called fluorescence. Therefore, absorption and fluorescence correction have to be performed with consideration of many factors including sample thickness, density and composition (Williams 1984).

A JEOL 2010 FX analytical electron microscope with EDS has been used for the composition analysis. The field emission gun used in this microscope, with acceleration voltage of 200 kV, can produce a bright electron beam with spot size as small as 1 nm in the STEM mode. In practice, the actual spatial resolution was affected by beam drifting,

carbon contamination, beam broadening and so on. Hence, the electron beam probe was carefully positioned for each analysis. EDS spectra acquisition and analysis were performed through a microcomputer using a Link ISIS software package of Oxford Instruments Ltd. GaAs, InAs, InP binary standards were used for composition quantification. 3-5 sets of measurements were carried out to establish statistical errors.

4.4. Photoluminescence

Photoluminescence (PL) provides a non-destructive optical technique for the determination of intrinsic and extrinsic properties of semiconductors. A light source is used to excite electrons from the valence to the conduction band, leaving holes in the valence band. These electrons and holes can recombine through radiative processes, emitting photons whose energies provide useful information about the semiconductor structure. While the technique has been extensively used for impurity identification, its most direct application is the determination of the bandgap of bulk material, or the effective energy bandgap of a quantum structure.

Transitions involved in bulk materials may include conduction band to valence band, free exciton, bound exciton, donor to acceptor, conduction band to acceptor, and donor to valence band recombination, depending on impurity concentrations and experimental conditions. The band-to-band transitions usually dominate at room temperature, while the observation of excitonic and impurity related transitions require low temperatures.

The PL intensity is proportional to the carrier densities in upper-energy and lower-energy states (Pankove 1971). For the band-to-band transition in a bulk material, the PL line shape follows

$$I_{CV} \propto \sqrt{h\upsilon - (E_c - E_v)}\exp\left(-\frac{h\upsilon - (E_c - E_v)}{k_B T}\right) \qquad 4.4$$

where I is the PL intensity, E_c, E_v are the conduction and valence band energies, $h\upsilon$ is the emitted photon energy, k_B is Boltzmann's constant and T is the temperature. It can be seen that the peak is broad, with its low-energy edge giving the energy bandgap of the material. In contrast, excitons, which are electron-hole pairs bound in a hydrogen-like state, usually appear at low temperatures and have much sharper spectral lines with well-defined energies. For free excitons, the energies are

$$h\nu = E_c - E_v - E_x \qquad 4.5$$

where E_x is the excitonic binding energy. The exciton has hydrogen-atom-like discrete energy levels with higher-order levels. Typical values of exciton binding energies are 4.1 meV for GaAs and 5.1 meV for InP (Madelung 1991). The transition energies of bound excitons are similar to those of free excitons but the additional binding energy of free excitons to impurity centers should be included. All these characteristic transition lines have frequently been used for material quality evaluation and material composition determination. While the composition of a ternary layer can be simply obtained from the bandgap energy measured by PL, the determination of quaternary compositions, which may be strained, demands a complementary technique such as X-ray diffraction, in addition to PL.

PL has also been extensively used in the studies of quantum structures, where transitions occur predominantly from the low effective bandgap regions. PL from QWs usually has higher intensity and narrower linewidth compared to bulk layers due to the modified density of states and carrier confinement. Also, due to the confinement of both electrons and holes, free exciton transitions usually dominate over conduction band-valance band transitions even at room temperature (Weisbuch 1991).

As seen in Chapter 2, energy levels of quantum structures depend on their dimensions. Thus, when PL is used to determine the composition of a ternary quantum

well layer, the layer thickness is required. This can be measured by techniques such as TEM. On the other hand, if the composition of a quantum well structure is known, the effective bandgap obtained using PL can be used to calculate the quantum well thickness. In the studies of QWRs and QDs, PL is frequently used to demonstrate the effective bandgap modification originating from quantum confinement. In other words, simply by observing peak energy shifting, PL has been used to verify the existence of QWRs or QDs (Gibert 1986, Chen 1993, Ils 1994), providing no composition variation exists. Under some conditions, PL transitions are not always from lowest energy levels (Rinaldi 1994, Maciel 1994). When transitions associated with higher-order energy levels are measured, extra information such as subband separations for the quantum structure can be obtained.

Also, as discussed in chapter 2, transitions between energy levels of quantum structures may be polarization dependent. Hence the polarization of PL emission can also be used to study low-dimensional quantum phenomena. For example, in-plane (normal to growth direction) PL polarization anisotropy was used to confirm QWR effects, when PL was taken from top surfaces of samples (Sugaya 1993, Pan 1994).

PL has been carried out to characterize bulk and QWR structures grown into V-groove etched substrates using the set up shown in fig. 4.1.

Samples were mounted on the cold head of a closed-cycle He-refrigerated cryostat, whose temperatures could be controlled from 11K to room temperature. For most of the work, the 488 nm line from a 20 mW Ar^+ laser has been used as the excitation source, with a spot diameter of about 250 μm on the sample. As discussed later, a 250 mW C-90 YAG laser, with a spot diameter of 1mm on sample and a wavelength of 1064 nm, was also used for excitation in some of the work. The source power was varied using neutral density filters. The emission signals from samples were dispersed by a Czerny-Turner monochromator with 600 lines/mm grating and detected with a room temperature InGaAs p-i-n diode. A long-pass (> 1μm) IR filter was placed before the monochromator to cut off

emission from bulk InP layers, whose 2nd-order diffraction overlaps with the wavelength range of interest. For polarization studies, a sheet polarizer was placed between the cryostat and the monochromator. The spectral response of the system, mainly from the monochromator and the detector, has been measured using a calibrated halogen lamp (Oriel 63358) under different polarization configurations. Based on the spectral response curves (shown in fig. 4.2), all PL spectra obtained in this work have been normalized so that peak intensities at different wavelengths could be compared.

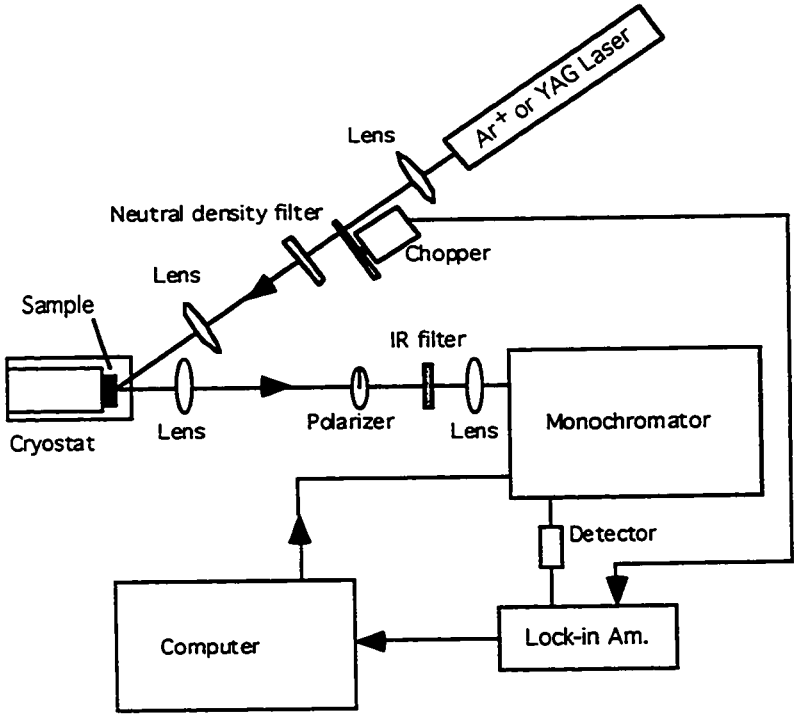

Figure 4.1. McMaster PL system

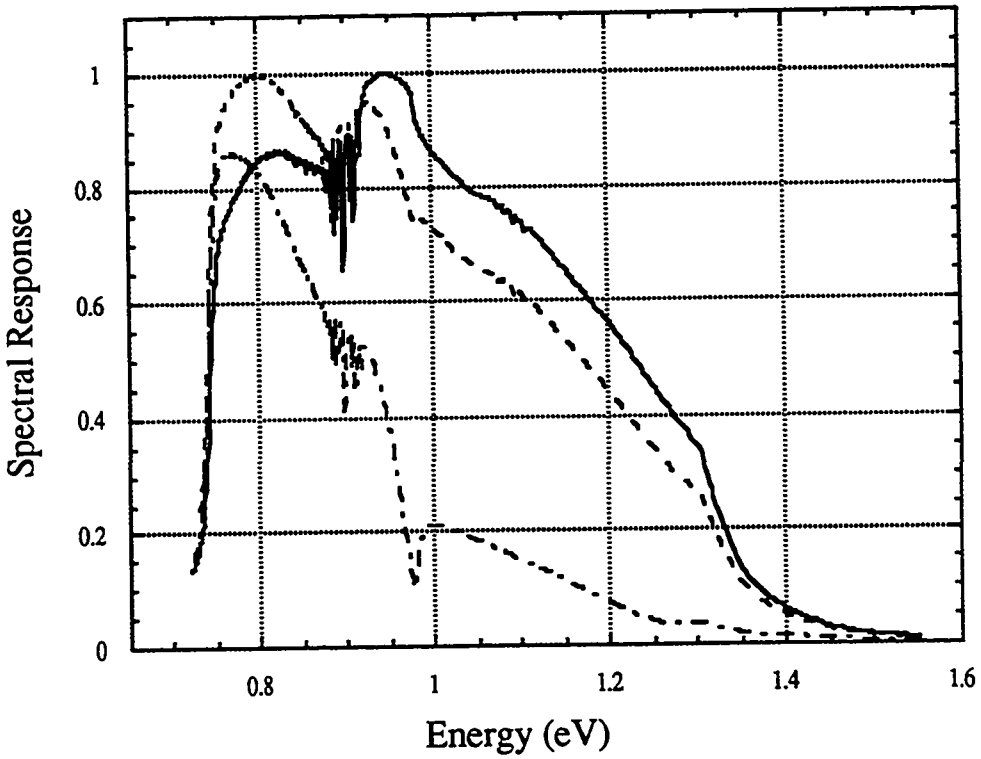

Figure 4.2. Spectral response of the McMaster PL system

Finally, for the study of structures grown on patterned substrates, spatial resolution of the luminescence is required. Cathodoluminescence (CL) and scanning PL have been used for this purpose (Kapon 1994, Grundmann 1994, Pan 1994). However, such equipment was not available at McMaster. Also, there are limitations to these techniques. CL is very convenient to use; however, its spatial resolution, mainly limited by a electron-hole generation volume and carrier diffusion, varies from 0.5 μm to several μm depending on the electron acceleration voltage (Galeuchet 1991). Compared to CL, a scanning PL has a more defined spatial resolution (less than 1μm), but scanning PL at low temperature is difficult to perform. In this work, a selective etching technique has been used to spatially resolve the PL spectral features. This will be discussed later.

CHAPTER 5. V-GROOVE ETCHING

5.1. Introduction to V-groove Etching

V-groove etching is the preliminary step for QWR fabrication using epitaxial growth on V-grooved substrates. Since the profiles will critically affect the final growth structures, understanding the etching process in various solutions and its control is important. V-groove etching is a specific example of preferential etching, and is attributed to crystallographic structure, in particular, the configuration of surface atoms and the bond structure (Kerr 1978). For a semiconductor single crystal, the etch rates may vary with the principal crystallographic directions, depending on the solution used. It is those surfaces with the slowest etch rates that determine the etched profile (Heimann 1982).

Most commonly V-grooves etched into III-V semiconductors have (111)A, (111)B or (211)A sidewalls. Figure 5.1 schematically shows the atomic structure of these grooves. The atomic arrangement and bond configuration of corresponding sidewall surfaces have been mentioned in Chapter 3. V-grooves with (111) sidewalls have angles of 70.5° in the bottom, while V-grooves with (211)A sidewalls have bottom angles of 109.5°. For a (100) wafer, the (111)B sidewall V-grooves lie along a [011] direction, while the (111)A and (211)A sidewall V-grooves orient along $[0\bar{1}1]$.

Both wet chemical etching (Huo 1987, 1988a, 1988b) and dry chemical etching (Tsang 1994, Henle 1993 and Gentner 1995) can be used to make V-grooves. Recently PCl_3 gas has been used to etch InP in a MBE chamber. Etched channels containing (011), (111)A and (111)B facets, even V-shape-like grooves, have been observed. However, a close examination of the sharpness of the groove bottom has not been reported (Tsang 1994, Henle 1993). If sharp bottoms can be achieved, this would provide an in-situ

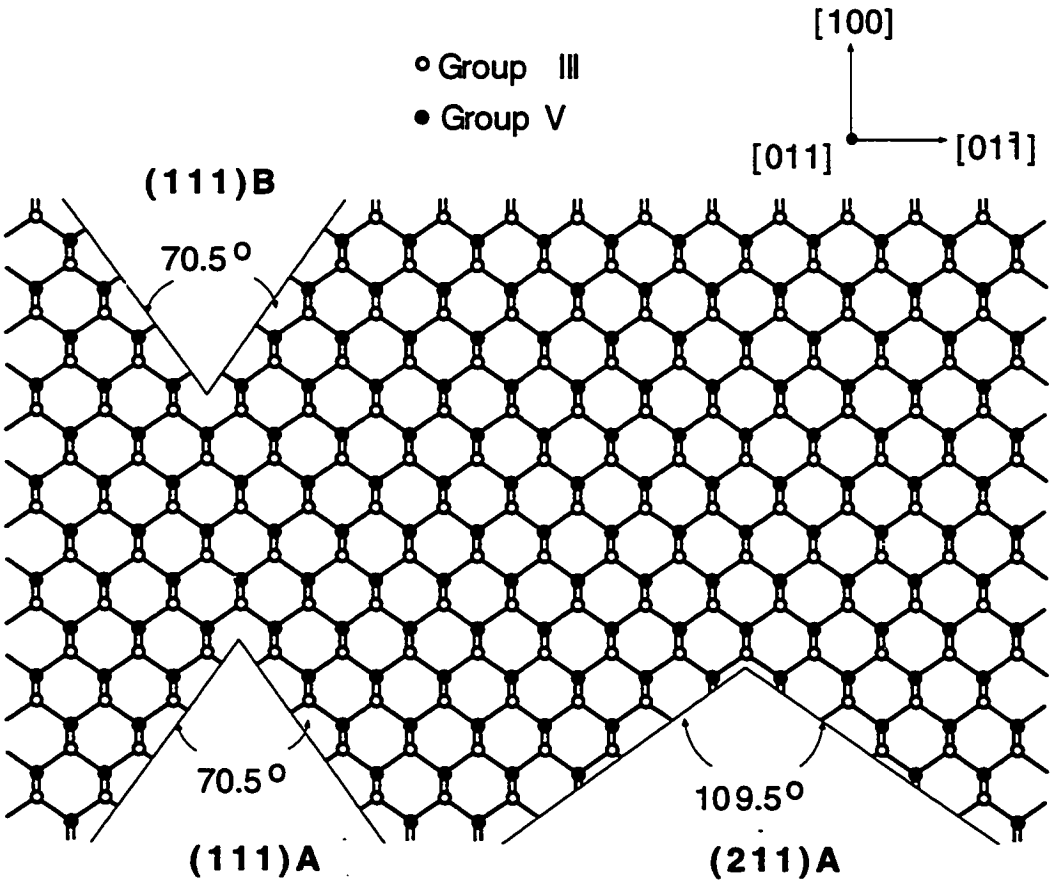

Figure 5.1. Atomic structures of V-grooves

technique for V-groove formation. Nevertheless, up to now, almost all V-grooves used for QWR fabrication have been obtained with wet chemical etching, which is simple, flexible and less demanding on equipment than dry etching. Preferential etching on III-V compounds including InP has been studied for many years; however, the etching process and mechanisms are still not well understood (Adachi 1981 and 1982). Moreover, little work has been reported on etching to produce sharp V-grooves for QWR fabrication (Huo 1987, 1988a, 1988b). Hou studied groove profiles etched on InP using HCl based solutions, but no detailed information was provided on the sharpness, or the profiles of the bottoms of the V-grooves. For QWR fabrication, simple V-grooves with sharp bottoms

and smooth sidewalls are required. To this end, we have conducted etching experiments using different etchants, different mask materials, as well as different degrees of mask misalignment. Also investigated were the etching processes and their dependence on surface orientation, as well as the important role of native surface oxides. Finally, V-groove etching recipes were developed that made the formation of 1-dimensional QWRs possible.

5.2. V-groove Etching Results

N-type and semi-insulating InP substrates have been used in this work. N-type substrates were from Crismatec or Acrotec, while semi-insulating substrates were from Sumitomo. All these wafers follow SEMI Option 1 designation of crystal orientations (Crismatec 1992), as shown in figure 5.2. No differences have been noticed in the etching behaviour of substrates from different sources.

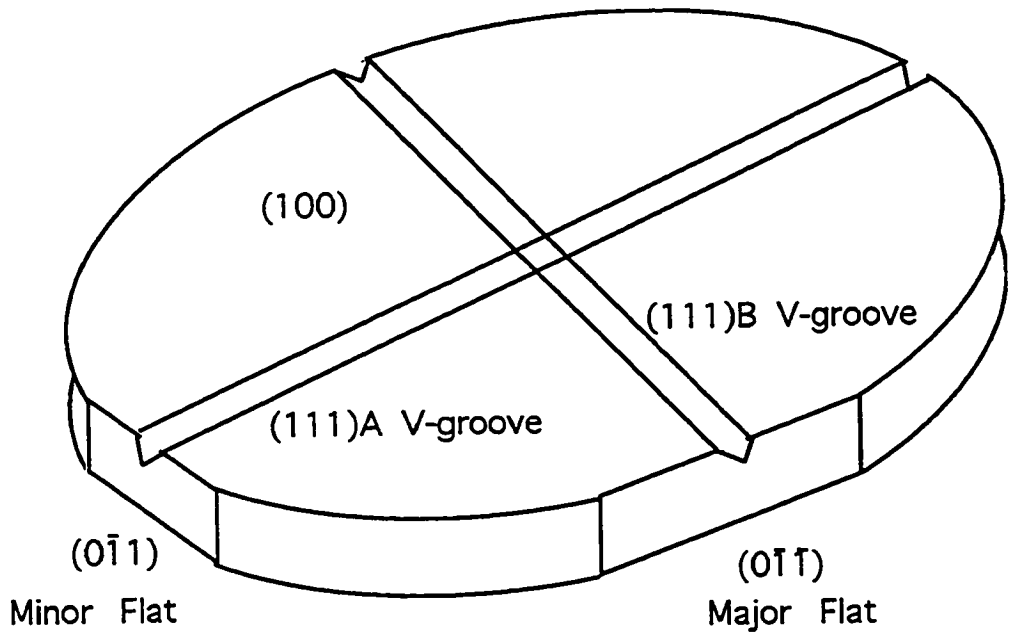

Figure 5.2. Wafer and mask line orientations for V-groove formation.

All wafers used had a final "epi-ready" finish, so no additional cleaning was applied unless wafers had been exposed to air for more than a month. When SiO_2 etch masks were used, the wafers were first coated with 100 nm thick SiO_2 layers at 300 ^oC in a Technics PE-CVD chamber. The etch mask was then defined using standard photolithographic and chemical etching techniques. When photoresist (PR) etch masks were used the wafers, except a few of them, were first etched in pure HF solution to remove native oxides, as proposed by Bulitka (1993b). Then Shipley 1808 positive photoresist was applied immediately, followed by a soft-bake at 85 ^oC in an oven for 25 min. Afterwards, conventional photolithographic techniques were used to define the etch masks. For etch studies, mask openings were 1 or 2 μm wide, separated by 2, 4, 7, 10, 13, 16 μm for grooves along $[0\bar{1}1]$ direction and 7, 10, 13, 16 μm for grooves along [011] direction. For the MBE growth studies, only masks with 1 μm wide openings were used.

Investigated etchants are divided into two groups: solutions containing oxidizing agents and HCl-based solutions. All solutions were prepared from reagent grade chemicals: HCl (37%), H_3PO_4 (85%), HBr (48%), HF (49%), Br_2 (purity > 99%), H_2O_2 (30%), $K_2Cr_2O_7$ (1N), methanol (CH_3OH) (purity > 99.5%). The etching, especially in $1HBr:1H_2O_2$, was only carried out after the mixed solutions had settled down.

5.2.1. Etching in solutions containing oxidizing agents

Three different etch solutions containing oxidizing agents were investigated:

a). Br_2-Methanol (2% by volume),

b). $1HBr:1H_2O_2$,

c). $2HBr:2H_3PO_4:1K_2Cr_2O_7$ (2:2:1).

These were used on substrates masked with either SiO_2 or photoresist.

5.2.1.1. SiO_2 etch mask

With CVD deposited SiO_2 masks, it was found that the resultant groove profiles were similar among these etchants. Typical results, for a 10s etch in $2HBr:2H_3PO_4:1K_2Cr_2O_7$, are shown in figure 5.3. For masks aligned along the $[0\bar{1}1]$ direction, (111)A V-grooves were formed and some mask undercutting, but no (011) vertical sidewalls, was observed. Higher magnification and top view (fig. 5.4) revealed that all had sharp bottoms and very smooth sidewalls. TEM examination further indicated that they had almost ideal point bottoms. For masks aligned along the [011] direction, dovetail-shaped grooves were formed (fig. 5.3b). The dovetail-shaped grooves had (111)A sidewalls in the upper sections of grooves, with dimensions of these sections varying among the three etchants.

5.2.2.1. Photoresist etch mask

Use of photoresist etch masks was also attempted using both Br_2-methanol and $2HBr:2H_3PO_4:1K_2Cr_2O_7$ solutions. These did not attack the PR, whereas $1HBr:1H_2O_2$ destroys the mask. It was found that basic features were the same as those obtained with SiO_2 masks, but mask undercutting was much larger and the (111)A V-grooves were incomplete, with wide, flat bottoms.

5.2.2. Etching in HCl-based solutions

5.2.2.1. SiO_2 etch mask

Etching experiments were conducted in $5HCl:1H_3PO_4$ solution. It was found that etching in this solution resulted in profiles totally different from those obtained in solutions containing oxidizing agents. Figure 5.5 shows etch results using SiO_2 masks. On the one hand, with the masks aligned along the $[0\bar{1}1]$ direction, shallow V-grooves were formed. The angles between sidewalls were consistent with (211) facets. The bottoms were sharp,

Figure 5.3. SEM pictures of grooves etched a). along the [$0\bar{1}1$] direction, b). along the [011] direction, in $2HBr{:}2H_3PO_4{:}1K_2Cr_2O_7$ at 23 °C for 10 sec. with SiO_2 masks.

a

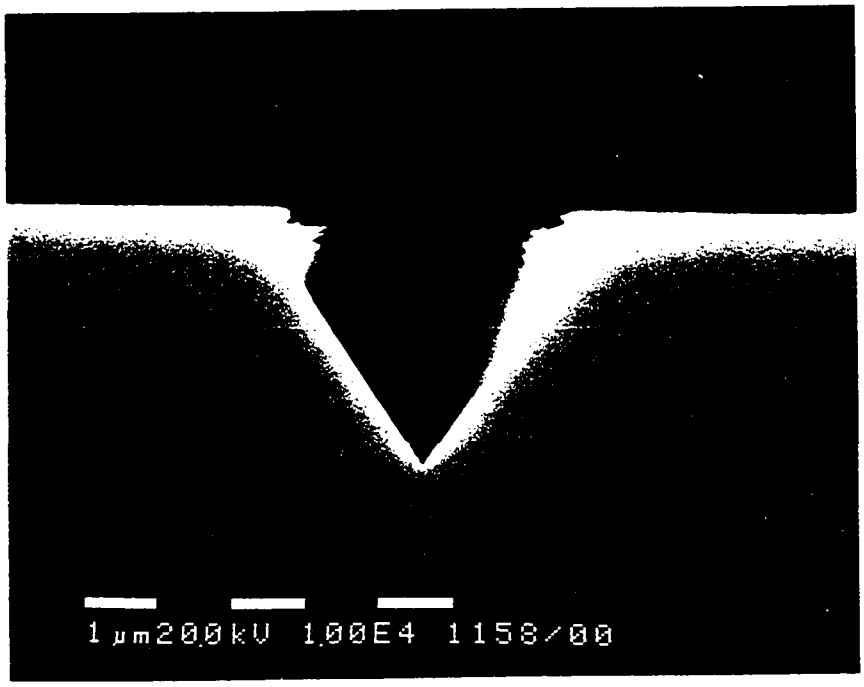

b

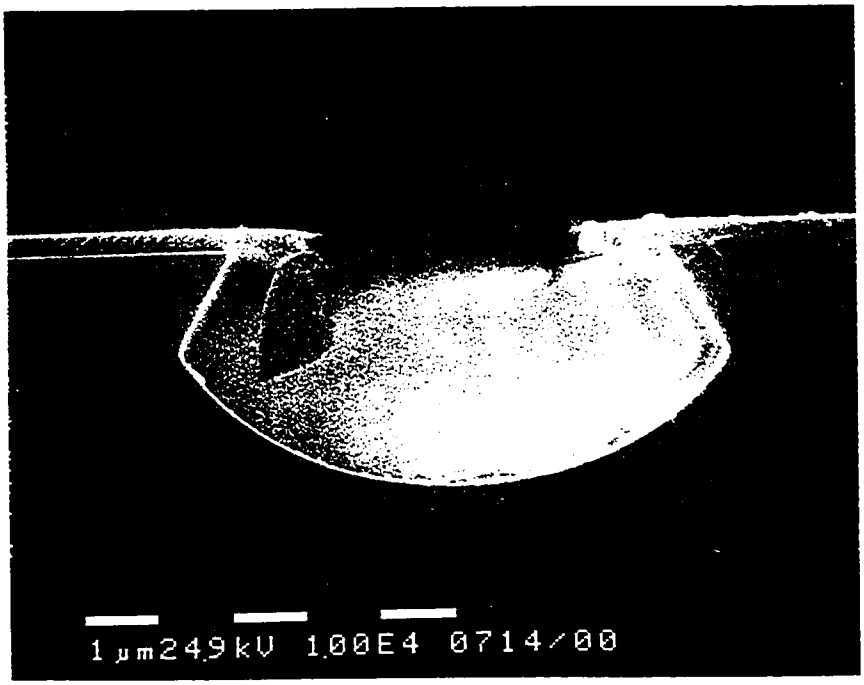

Figure 5.4. SEM pictures of grooves etched along the [0$\bar{1}$1] direction in $2HBr:2H_3PO_4:1K_2Cr_2O_7$ at 23 °C for 10 sec. with SiO_2 masks, a). higher magnification cross-sectional view of image 5.3(a), showing the sharpness at the bottom and smoothness on sidewalls, b). top view, showing smoothness.

a

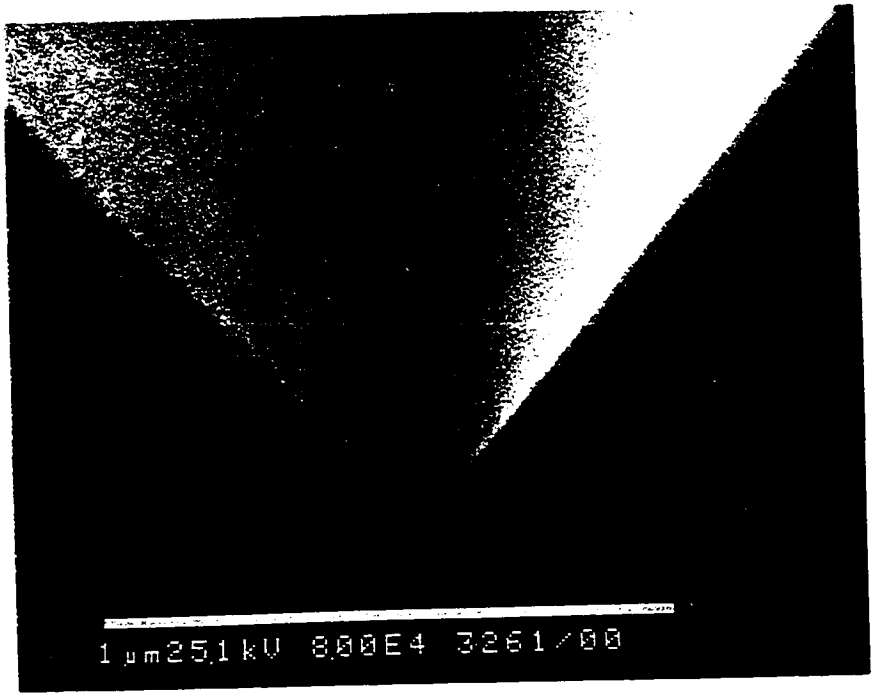

b

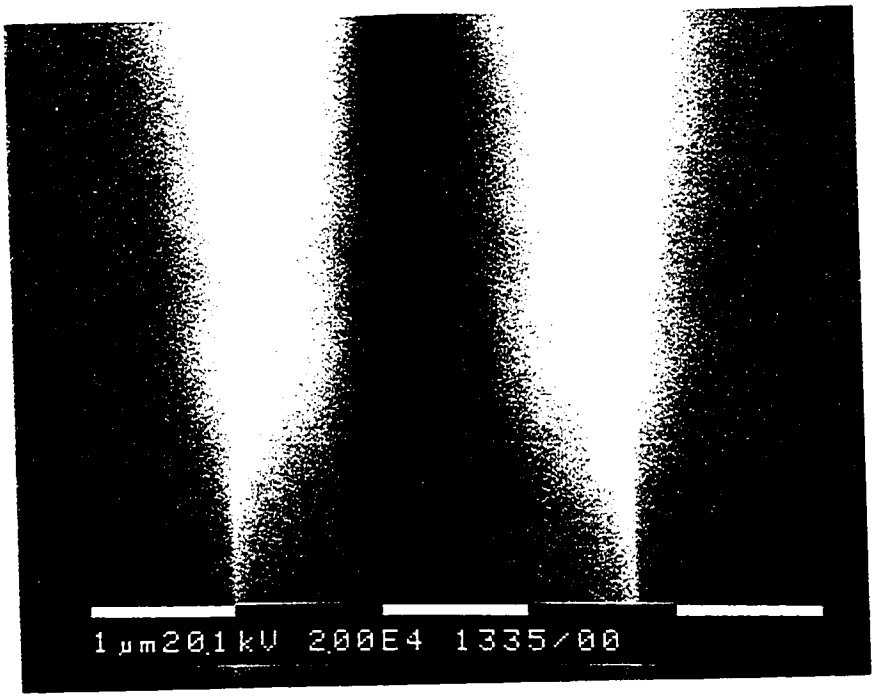

but the sidewalls were very rough and striated. On the other hand, with the masks along the [011] direction, the etched grooves were arrow-shaped, that is, they had $(0\bar{1}1)$-like upper sidewalls and (111)B lower sidewalls. The almost vertical upper sidewalls formed at the beginning of the etching and their length increased with the etch time, while the sizes of (111)B sidewalls did not change much once the V shape formed at bottom. Also, the lower, (111)B sidewalls were quite smooth but upper, vertical sidewalls, were striated.

5.2.2.2. InGaAs etch mask

Similar results were also observed using an $In_{0.53}Ga_{0.47}As$ layer as an etch mask. A 400 nm thick InGaAs layer was grown by MBE directly on a freshly grown InP layer to eliminate any interfacial oxide and selectively etched in citric acid (50 wt%):H_2O_2 (3:1) for 4 min. to form the subsequent etch mask. Some undercutting was observed on the InGaAs layer. As shown in fig. 5.6, arrow-shaped grooves still formed. However, no mask undercutting, between InGaAs and InP, was produced. This will be used later to discuss the effect of a native oxide layer on undercutting in section 5.4. The arrow-shaped profiles obtained, using SiO_2 and semiconductor etching masks, mean that (111)B surfaces have a higher etch rate than $(0\bar{1}1)$ surfaces in $5HCl:1H_3PO_4$.

5.2.2.3. Photoresist etch mask

To achieve ideal V-grooves with (111)B sidewalls, the vertical sidewalls have to be eliminated. This was previously achieved by introducing a certain amount of mask undercutting. Dautremont-Smith (1986) used ozone-generated oxides on the InP surface to increase undercutting of SiO_2 masks and managed to diminish the vertical sidewalls. Hou (1987, 1988a and 1988b) used photoresist masks to achieve only (111)B sidewalls after he found that undercutting of photoresist masks was much higher than that of SiO_2 masks.

Figure 5.5. SEM pictures of grooves etched a). along the [$0\bar{1}1$] direction, b). along the [011] direction in 5HCl:1H_3PO_4 at 23 °C for 30 sec. with SiO_2 masks.

a

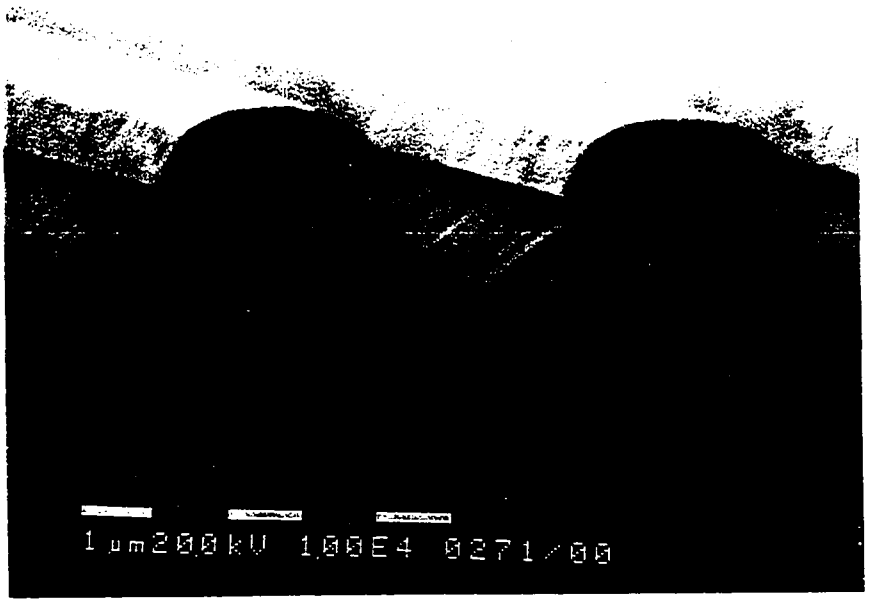

b

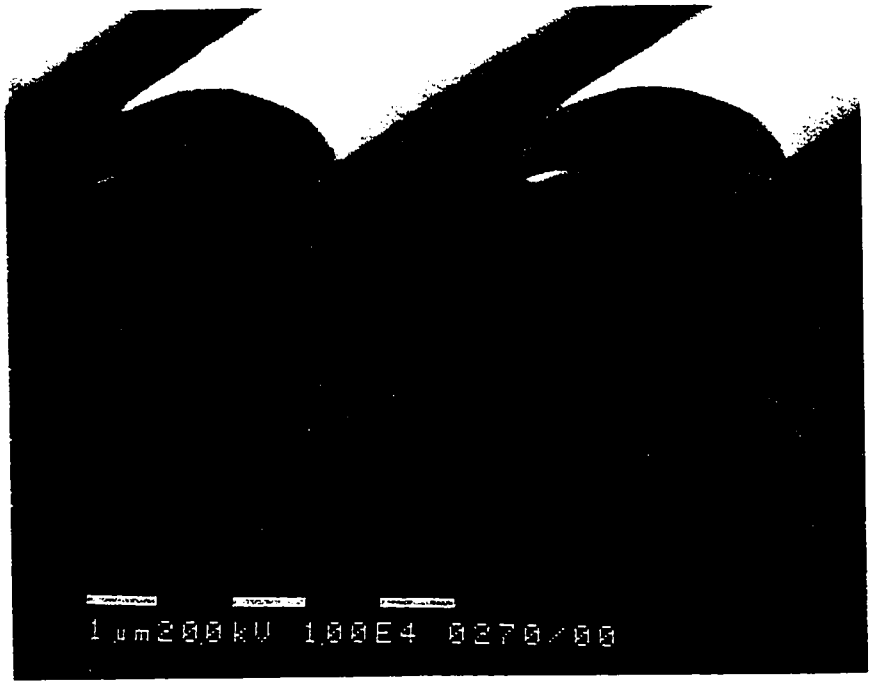

Figure 5.6. SEM pictures of grooves etched along the [011] direction in $5HCl:1H_3PO_4$ at 23 °C for 30 sec. with a 400 nm thick InGaAs etching mask.

Fig 5.6

In this work, we also performed etching in $5HCl:1H_3PO_4$ using photoresist masks, but with minimization of native surface oxide formation, as suggested by Bulitka (1993b). Figure 5.7 shows the etching results. (211)A V-grooves forming along the $[0\bar{1}1]$ direction were similar to those obtained using SiO_2 masks (fig. 5.5a). Grooves etched along [011] directions had only (111)B sidewalls. Also, mask undercutting for (111)B V-grooves was significant (about 50%), while little undercutting was observed for the (211)A V-grooves. This is consistent with the assumption that a certain amount of undercutting is necessary in order to obtain triangular-shape grooves with only (111)B sidewalls. However, the undercutting should not be too large, otherwise the lateral etch rate becomes too large compared to the vertical etch rate, and grooves with flat bottoms are formed. Figure 5.8 shows the dependence of V-groove bottom sharpness on different processing procedures. Without using pure HF to remove native oxides prior to applying the photoresist mask, the V-grooves had wide flat bottoms, no matter how long the wafer was etched (fig. 5.8(a)), as a result of the extensive mask undercutting. With native oxides removed in HF immediately before applying photoresist, the V-groove bottoms were sharp, as shown in fig. 5.8(b). Also seen in figures 5.8, the (111)B sidewalls were always very smooth. Higher magnification SEM or TEM examinations, however, indicated that the bottom of the (111)B V-groove always had a small, 20-40 nm wide, region with a (100) surface. Stirring by hand or ultrasonic agitation during etching helped to minimize the size of (100) region.

5.2.3. Effect of mask misalignment

The etched groove profiles are dependent not only on the etchant and type of etch mask, but also on the amount of mask alignment offset. When photoresist masks were aligned so that the grooves were a few degrees off the [011] directions, groove profiles obtained in $5HCl:1H_3PO_4$ were modified dramatically, as shown in fig. 5.9. When masks

Figure 5.7. SEM images of grooves etched a). along the [0$\bar{1}$1] direction, b). along the [011] direction, in 5HCl:1H_3PO_4 at 23 °C for 30 sec. with photoresist masks.

a

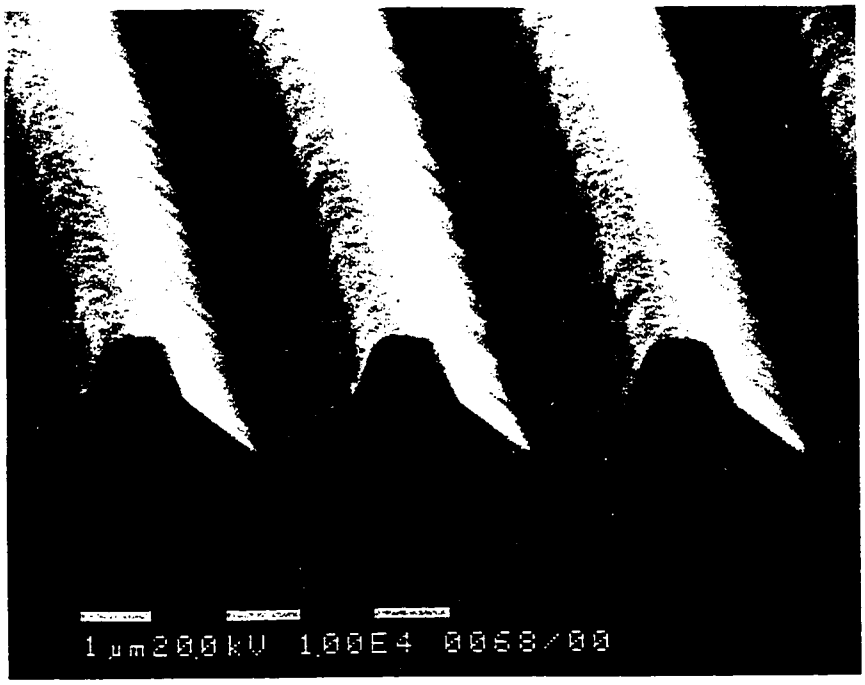

b

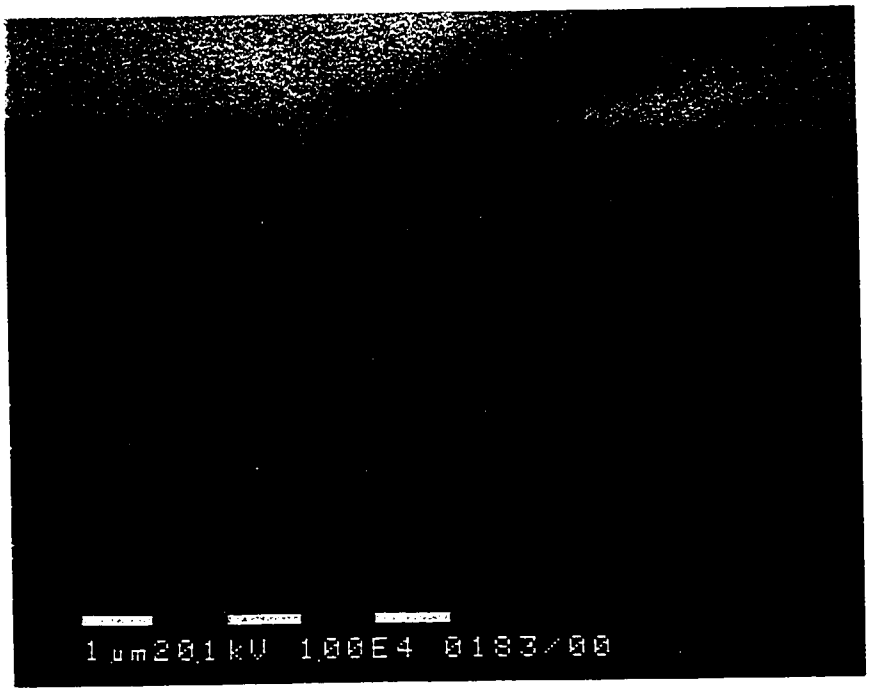

Figure 5.8. SEM images of grooves etched along the [011] direction in $5HCl:1H_3PO_4$ at 23 °C for 30 sec. with photoresist masks, a). obtained without native oxides removal, b). obtained with native oxides removed using HF (a high magnification of fig. 5.7(b)) showing the sharpness at a bottom, as well as the smoothness on sidewalls.

6a
Fig. 5B

a

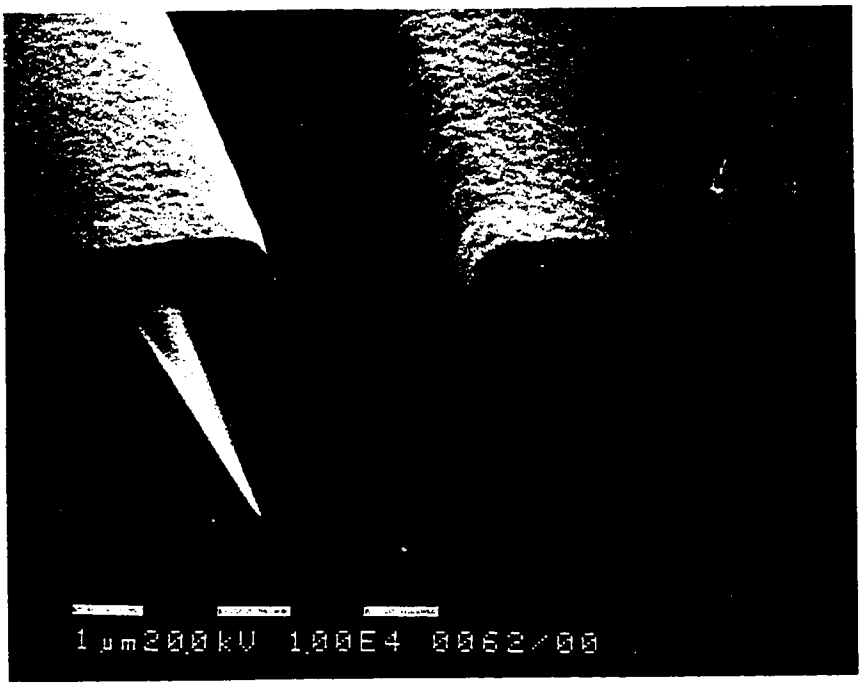

b

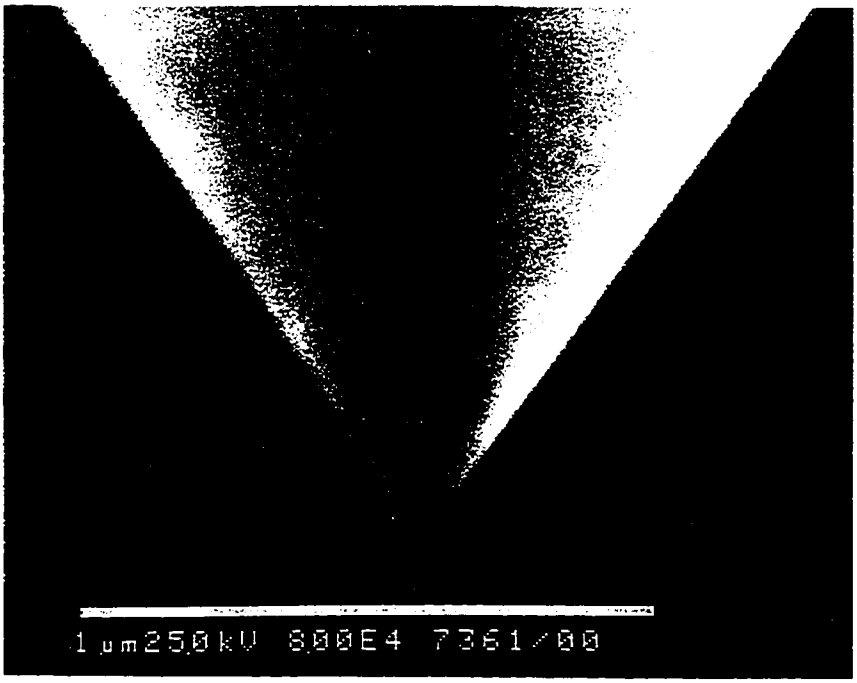

Figure 5.9. SEM images of grooves etched in 5HCl:1H_3PO_4 at 35 °C for 15 sec. with photoresist masks aligned along: a) 0° off; b) 1° off; c) 2° off; d) 3° off, from the [011] orientation.

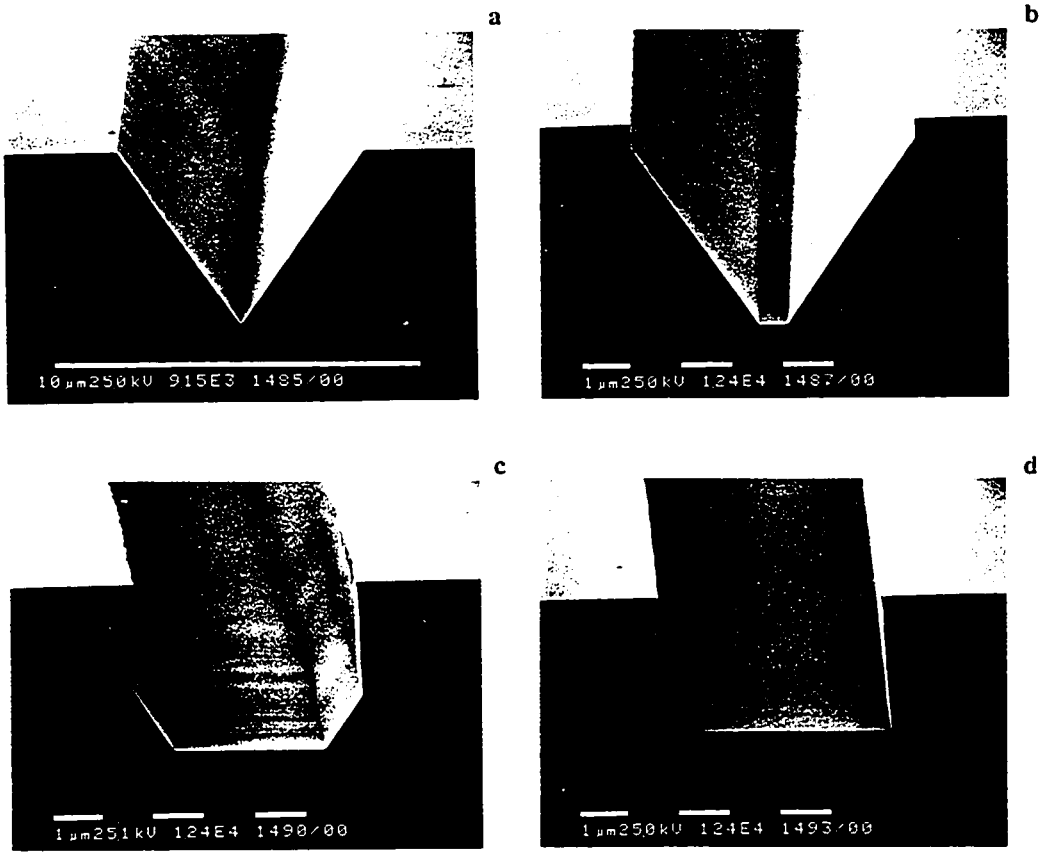
a
10µm250kV 915E3 1485/00
b
1µm250kV 124E4 1487/00
c
1µm251kV 124E4 1490/00
d
1µm250kV 124E4 1493/00

were 1^{o} misaligned, small $(0\bar{1}1)$ vertical sidewalls developed at the top and (100) V-groove bottoms became as wide as 0.6 μm. For a 3^{o} misalignment, the (111)B sidewalls disappeared completely and the grooves had rectangular shape with almost vertical sidewalls and complete (100) bottoms. Obviously, these results cannot simply be explained by undercutting. Nevertheless, they suggest that accurate mask alignment is imperative for good V-groove formation. On the other hand, a few degrees of misalignment could be used to form rectangular grooves or mesas with almost vertical sidewalls.

Similar experiments, using etchants containing oxidizing agents, were also performed with SiO_2 masks aligned along or close to the $[0\bar{1}1]$ direction. In this case, the etched groove profiles did not change with a few degrees of misalignment and the V-grooves always had sharp bottoms.

Finally, there was no difference in the groove profiles etched using different types of substrates, except that semi-insulating substrates showed more defected grooves than n-type ones. This is consistent with higher defect densities usually present in semi-insulating substrates compared to n-type substrates.

5.3. Chemical Etching Processes and Groove Profiles

Chemical etches are routinely used for semiconductor processing; however, the chemical reactions involved in the III-V compound semiconductor dissolution are not well understood (Faust 1962, Adachi 1982, Gatos 1960). In particular, there is little understanding of the etching processes for different crystallographic surfaces.

Usually III-V semiconductor etching involves breaking covalent bonding in the presence of an oxidizing agent. However, a few of the compounds such as InP, which have significant ionic character to the bonds, can be attacked by acids such as HCl (Faust 1962).

5.3.1. Chemical reactions

5.3.1.1. HCl-based solutions

Notten (1984) studied the etching of InP in HCl solutions. He found that significant etching occurs only at high HCl concentrations, and suggested that it is the undissociated HCl molecule that participates the etch process by acting to break the In-P bonds. An exchange type reaction was suggested with a reaction equation given as

$$InP + 3HCl \rightarrow InCl_3 + PH_3 \qquad 5.1$$

Here, $InCl_3$ is hydrolyzed through various possible processes and PH_3 is evolved as a gas. The formation of PH_3 was confirmed by gas analysis. Actual bubbles were observed in our etching experiments involving HCl (+H_3PO_4).

In this work 5HCl:1H_3PO_4, instead of HCl, has been used as the V-groove etchant. While both HCl and HCl:H_3PO_4 solutions, with various ratios, can form similar groove profiles (Adachi 1981, Hou 1987), the H_3PO_4 acts as a buffer agent, decreasing the etch rate (Adachi 1981, Uekusa 1985, Turley 1982) and probably improving the surface morphology. However, excessive H_3PO_4 will decrease the HCl concentration and modify etched groove profiles (Turley 1982, Phatak 1979).

Another reaction process for InP dissolution in HCl was proposed by Hsieh (1990). The suggested mechanism involves a photogenerated hole which attracts Cl^- ions and stimulates the nucleophilic attack of the In in InP which subsequently dissolves via some intermediates. The remaining P might then form PH_3 or H_3PO_4. It seems that this mechanism probably works at relatively low HCl concentration (< 5M) where the etch rate is very low. However, under the high concentrations used for V-groove etching, this mechanism may not be occurring.

5.3.1.2. Oxidizing agent-based solutions

The etching of InP in Br_2, which is usually dissolved in organic solvents such as methanol (Notten 1987), is also believed to be through a chemical reaction. However, an oxidation-reduction reaction is involved, instead of an exchange type reaction. Br_2 is a strong, bifunctional oxidant. It can form two new bonds with the semiconductor surface more or less simultaneously (Gerischer 1968), and similar to GaAs (Gerischer 1968), InP reacts with Br_2 (Notten 1987) as

$$InP + 3Br_2 \rightarrow InBr_3 + PBr_3 \qquad 5.2$$

As expected, no bubble evolution was observed when InP was placed in the 2% Br_2-methanol solution.

The dissolution of InP in HBr is similar to that in HCl solutions (Notten 1987), that is, InP is chemically etched by molecular HBr. However, the reaction processes for InP in $1HBr:1H_2O_2$ and $2HBr:2H_3PO_4:1K_2Cr_2O_7$ are unknown (Adachi 1981, 1982) and H_2O_2 and $K_2Cr_2O_7$ are expected to have significant direct or indirect effects on the reaction processes. Bubble evolution was observed during the dissolution of InP in HBr; however, there was no gas evolution observed in $2HBr:2H_3PO_4:1K_2Cr_2O_7$. Also, fewer bubbles were observed in $1HBr:1H_2O_2$ than in HBr even though the etch rate of InP in $1HBr:1H_2O_2$ was expected to be higher than in HBr (Adachi 1981). These phenomena indicate that the reaction products have been changed by $K_2Cr_2O_7$ and H_2O_2. Since H_2O_2 and $K_2Cr_2O_7$ are oxidants, oxidation of the InP could be directly involved (Notten 1984). However, it was observed that HBr reacted vigorously with H_2O_2, when first mixed, to give off a brown gas, Br_2, thus it is possible that the function of H_2O_2 might only be to generate Br_2 in the solution which is an effective etchant for InP. A similar argument could

also be applied to $K_2Cr_2O_7$; that is, $K_2Cr_2O_7$ ($Cr_2O_7^{-2}$) might oxidize HBr thus producing Br_2, indirectly affecting the etching of InP (Shrobilgen, 1997).

5.3.2. Effect of crystallographic structure

5.3.2.1. Etch rates of different crystallographic surfaces: experimental observations

In the above discussion of the etching processes for InP, crystallographic surfaces are not considered. However, the various etching profiles obtained are certainly due to

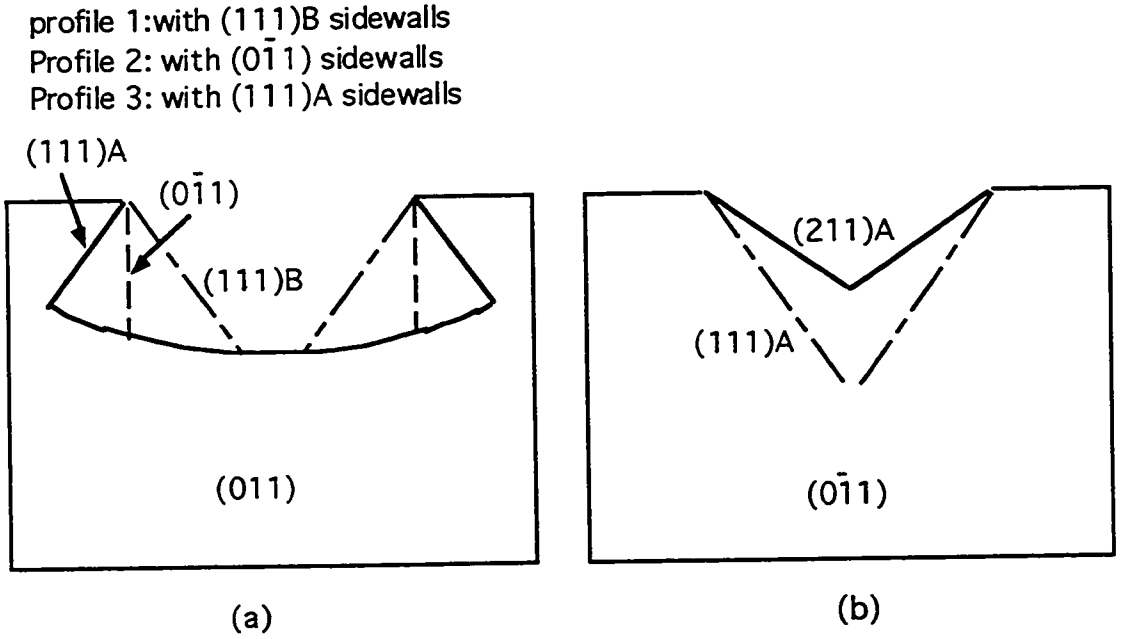

Figure 5.10. Some possible etched sidewalls and groove profiles: a) grooves along the [011] direction; b) grooves along the [0$\bar{1}$1] direction.

different etch rates of various crystallographic planes. For solutions containing oxidizing agents, the attainment of ideal (111)A V-grooves (fig. 5.3(a)), aligned along the [0$\bar{1}$1] direction , indicates that the etch rate of (111)A surfaces is much less than that of (100) and (211)A surfaces. The dovetail-shaped grooves, aligned along the [011] direction, with

(111)A upper sidewall facets (fig. 5.3(b)), indicate that (111)B and $(0\bar{1}1)$ surfaces also have higher etch rates than (111)A surfaces. This is further illustrated in fig. 5.10(a) with the consideration of the locations of different planes relative to the mask openings. If (111)B surfaces etch slowly, compared to a (100) and other surfaces, the profile 1 in fig. 5.10(a) should be realized. If (111)B surfaces etch fast but $(0\bar{1}1)$ surfaces etch slowly, the profile 2 in fig. 5.10(a) should be formed. Only when (111)B surfaces and $(0\bar{1}1)$ surfaces etch fast and (111)A surfaces etch slowly, can the profile 3 (dovetail-shaped), be obtained, which was observed in fig, 5.3(b).

The (111)B V-grooves obtained in the $5HCl:1H_3PO_4$ solution with a photoresist mask opening aligned long the [011] direction (fig. 5.7(b)) indicate that the etch rate of (111)B surfaces is slower than that of a (100) surface. However, the large groove width and the presence of a small flat (100) region at the bottom, suggest that the etch rate of the (111)B surface is not dramatically slower than that of a (100) surface. The arrow-shaped profile obtained with an SiO_2 mask also implies that the etching of the $(0\bar{1}1)$ surface is much slower than the (111)B and (100) surfaces when undercutting is not serious. The (211)A V-groove profiles obtained in the $5HCl:1H_3PO_4$ solution with either photoresist or SiO_2 masks aligned along the $[0\bar{1}1]$ direction indicate that the etch rate of the (211)A surface is much slower than the (100) surface. Also, (211)A surfaces have much smaller etch rates than (111)B surfaces since their width does not increase with etch time as observed for (111)B grooves. However, the formation of (211)A V-grooves does not necessarily mean that (211)A surfaces etch slower than (111)A surfaces. Actually, we found that, the use of HBr leads to (111)A V-grooves, not (211)A V-grooves. It was also reported (Adachi 1981) that the addition of H_2O_2 into the HCl solution would change groove sidewalls from (211)A surfaces to (111)A surfaces. These results suggest that (111)A surfaces have slower etch rates than (211)A. One of the reasons for the formation

of (211)A V-grooves in 5HCl:1H_3PO_4 etchant is that (111)A planes lie underneath (211)A planes, as shown in fig. 5.10(b). As long as (211)A surfaces etch very slowly, there is no chance for (111)A surfaces to be exposed.

In summary, the groove profiles obtained suggest that the etch rates of various surfaces vary as below:

- in solutions containing oxidizing agents:

$$(100) \gg (111)A \qquad 5.3$$

$$(211)A > (111)A \qquad 5.4$$

$$(111)B \text{ and } (0\bar{1}1) > (111)A$$

- in 5HCl:1H_3PO_4 solution:

$$(100) > (111)B \gg (0\bar{1}1) \qquad 5.6$$

$$(100) > (111)B \gg (211)A \qquad 5.7$$

5.3.2.2. Etch rates of different crystallographic surfaces: Phenomenological analysis

The etching behaviour of the different surfaces can be related to their corresponding surface bond and electron configurations. As shown in Chapter 3, (100) surfaces are terminated with either A or B atoms. In either case, atoms on a (100) surface have double dangling bonds. Consequently, they are chemically quite reactive. On the other hand, (111) surfaces have only single dangling bonds, which suggests that they are less reactive than the (100) surface. Also, a significant difference in reactivity can exist between (111)A and (111)B surfaces. For (111)A surfaces, the dangling bonds are empty, while at (111)B surfaces, the dangling bonds are filled with pairs of electrons (Gatos 1960b). Because of the unshared pairs of electrons (Gatos 1960b, Li 1993), (111)B surfaces are more reactive than (111)A surfaces, especially in oxidizing agents. The (011) surfaces have both A and B atoms with single dangling bonds. Therefore, their reactivities lie between (111)A and (111)B surfaces. The (211)A surfaces also have both A and B atoms, but they have twice

as many A atoms compared to B atoms, with A and B atoms having single and double dangling bonds, respectively. Therefore, (211)A surfaces should be less reactive than (100) and (111)B surfaces but more reactive than (111)A surfaces. In etchants containing oxidizing agents, the etch rate difference between (111)A surfaces relative to the others would be enhanced, because the oxidization process takes electrons from the semiconductor. In particular, (111)B surfaces would become more reactive, while (111)A surfaces would not be significantly affected. In summary, the consideration of the dangling bond and electron configurations on the various crystallographic surfaces leads to the following order of surface reactivities:

- in solutions containing oxidizing agents:

(111)B and (100) > (011) > (111)A 5.8

(111)B and (100) > (211)A > (111)A 5.9

- in $5HCl:1H_3PO_4$ solution:

(100) > (111)B > (011) > (111)A 5.10

(100) > (111)B > (211)A > (111)A 5.11

The above order of reactivities are consistent with the order of etch rates induced from the analysis of the groove profiles (eq. 5.3-5.7). Interestingly, from equations 5.6 and 5.10, it can be predicted that V-grooves with (011) sidewalls should be obtained with a mask aligned along the [010] or [001] directions in the $5HCl:1H_3PO_4$ solution. This prediction was actually confirmed experimentally. As shown in fig. 5.11, (011) V-grooves have been formed with very sharp bottoms and smooth sidewalls.

From the above analysis, the following conclusions can be drawn: (1) solutions containing oxidizing agents favour the formation of (111)A V-grooves; (2) oxidizing agents should be avoided when (111)B, (211)A and (011) V-grooves are required.

Figure 5.11. SEM image of a (011) V-groove etched in $5HCl:1H_3PO_4$ at 35 °C for 15 sec. with the SiO_2 mask aligned along the [010] direction.


10µm20.0kV 8.40E3 1241/00

In addition, the off-[011] alignment features of etched groove profiles can be understood from the small difference in etch rates between the (111)B and the (100) surface and the large difference in etch rates between (111)B and (011) surfaces. With etch masks misaligned from the [011] direction, steps would be introduced onto the sidewalls, but not onto the groove bottoms. Introducing steps on the (111)B sidewalls would increase the etch rate to exceed that of the (100) surface. However, the etch rate of the $(0\bar{1}1)$ surface is not increased to a significant value due to very slow etch rate of the surface. Thus, (111)B sidewalls could be totally replaced by $(0\bar{1}1)$ surfaces with a certain degree of off-alignment. In contrast, due to the very slow etch rates of the (111)A surfaces, the off-alignment did not change the (111)A V-groove profile.

5.3.3. Kinetic considerations

Groove profiles also depend on the reaction kinetics. The dissolution processes are either reaction-rate limited or diffusion-limited (Kern 1978). Diffusion-limited dissolution occurs when the process depends on the transport of reactants and products to or from the surface by diffusion through a liquid or gas. It has been reported that the dissolution, in Br_2 based solutions, of a planar (100) surface is diffusion-limited and that of a (111)A surface is reaction-rate limited (Notten 1987). However, the dissolution mechanisms for various surface planes in all the above solutions have not been completely established. Nevertheless, the transport of the etchant by diffusion could be very important for V-groove etching. One the one hand, for (111)B V-groove etching, since both the (100) surface and the (111)B surfaces are very reactive, the transport of reactants could limit the dissolution process at bottom regions of V-grooves, which would make the etch rate of the (100) surface comparable to that of the (111)B surfaces. This would explain why the (111)B V-groove always has a small (100) region at the bottom, even though the planar (100) surface has a slightly higher etch rate than a planar (111)B surface. On the other hand, the etch rate of the (111)A surface is so low that the diffusion of reactants is not the

limiting process for (111)A V-groove etching. Thus, the (111)A V-grooves with perfect point bottom profiles can easily be formed.

5.4. Native Oxide and Undercutting

The above and previous etch studies (Huo 1988a and 1988b, Dautremont-Smith 1986 and Notten 1991) show that V-groove profiles can be significantly affected by mask undercutting. With excessive undercut, wide, flat-bottomed (111) V-grooves are produced and successful etching of (111)B V-grooves depends on control of the undercut. In addition to V-groove etching, an essential step in the production of many InP-based devices requires the etching of features with a well-defined size and shape into multi-layer structures grown on InP substrates. This points out the need to understand the mechanism responsible for the undercutting and to establish possible techniques for its minimization so that the desired control can be obtained.

Many researchers (Bulitka 1993b, Huo 1988a and 1988b, Dautremont-Smith 1986 and Notten 1991) have suggested that the undercutting is due to the native oxide that is present on the InP surface leading to an interfacial layer between the mask and InP. The InP oxide consists of a mixture of various In and P oxides, with the average composition depending upon the specific oxidation process. In many cases the InP surface is first passivated with a UV-ozone-formed oxide in order to achieve a reproducible and stable oxide. Even without the UV-ozone step, a native oxide forms after a very short exposure to air and would be present to various degrees in all previous work. It is found that UV-ozone formed oxide has an average composition of $InP_{0.5}O_{2.75}$, while thermal oxide has a composition close to $InPO_4$ (Hollinger 1991). Also, it has been suggested (Notten 1991) that the first few monolayers of the native oxide may possess an ordered structure that could affect the dissolution process immediately between the photoresist and InP substrate.

One explanation for the undercutting (Huo 1988a and 1988b, Bulitka 1993b, Notten 1991) is based on the proposal that the native oxide reduces the adhesion between the mask and the InP substrate. For the chemicals which exhibit very slow etch rates for (111) or $(0\bar{1}1)$ surfaces, etching of the oxide under the mask exposes some (100) surface, which would then be rapidly etched. Whether or not this explanation is correct, the importance of the native oxide on the InP can be determined only by being able to mask the substrate in a way that results in an oxide-free interface between the mask and the substrate. This has been achieved in this work using an electron cyclotron resonance chemical vapor deposition (ECR-CVD) system which is vacuum-linked to the GSMBE system.

SiN_x films were used as the etch mask defining the grooves. The InP substrates were subjected to two preparation treatments prior to deposition of the SiN_x coating. One treatment involved loading the substrate, covered with a native oxide into the ECR-CVD chamber directly from atmosphere. The alternate treatment involves exposing the substrate to a UV-ozone oxidation, a degas in vacuum for 15 min at 300 ^{o}C followed by removal of the oxide in a MBE growth chamber by heating the substrate to 470 ^{o}C in a simultaneous P_2 flux and ECR H-plasma for 5 min. This removed all trace of oxide (Robinson 1992, Hofstra 1993 and 1995). After oxide removal, the substrate was transferred in vacuum ($\sim 10^{-9}$ Torr) to the ECR-CVD system. The SiN_x films were deposited by ECR-CVD (Boudreau 1993a, 1993b) using tris(dimethylamino)silane (TDAS) as the source of Si and nitrogen as the reactive plasma gas. The deposited films were 20 nm thick. Finally, the conventional photolithographic and SiN_x etching techniques were used to form the mask patterns.

Figure 5.12 shows the etching results of InP substrates having a native oxide between the SiN_x mask and InP. All these groove profiles are basically the same as those obtained using SiO_2 masks (fig. 5.3 and fig. 5.5). The degree of undercut for each sample

is given in Table 5.1 relative to the initial mask opening (1 or 2 μm). Figure 5.12(a) shows a (211)A V-groove etched by $5HCl:1H_3PO_4$ for 30s. The undercut was observed equivalent to ~25% of the initial 2 μm opening in the SiN_x mask. The grooves in figure 5.12(b) were etched with the $5HCl:1H_3PO_4$ solution for 30s resulting in grooves with nearly vertical sidewalls at the top, while facets with smooth (111)B sidewalls formed in the bottom. The undercut was ~23%. Figures 5.12(c) and (d) show (111)A sidewall grooves formed using different etchants. For a 2 min $2HBr:2H_3PO_4$: $1K_2Cr_2O_7$ etch the grooves had smooth sidewalls but very large undercut (~64%), as can be seen in figure 5.12(c). By contrast, the results of a 10s Br-methanol etch give grooves with reduced (~32%) undercut whilst still producing smooth sidewalls.

TABLE 5.1. Measured undercut

Sidewall	Etch	Mask	Degree of undercut	
			Oxide-free	With oxide
(211)A	5:1	2 μm	0%	25%
(111)B	5:1	2 μm	16%	23%
(111)A	2:2:1	2 μm	45%	64%
(111)A	Br-Methanol	1 μm	0%	32%

Results for the same etching procedures carried out on de-oxidized InP substrates are shown in figures 5.13(a-d). Again sharp V-features are obtained in the bottom of the V-groove. The degree of undercut for these samples is also shown in Table 5.1. It is clear from both the figures and the table that the undercut is considerably reduced, and in the case of the (211)A and (111)A (Br-methanol) etched V-grooves the undercut is essentially eliminated. In past work, the native oxide has been given as the cause of the undercutting.

Figure 5.12. SEM pictures of etched InP samples where the substrates were covered with a native oxide prior to coating with SiN_x:
a) (211)A V-groove etched along [$0\bar{1}1$] direction in $5HCl:1H_3PO_4$ at 23 °C for 30 sec.;
b) (111)B V-groove etched along [$01\bar{1}$] direction in $5HCl:1H_3PO_4$ at 23 °C for 30 sec.;
c) (111)A V-groove etched along [$0\bar{1}1$] direction in $2HBr:2H_3PO_4$: $1K_2Cr_2O_7$ for 2 min.;
d) (111)A V-groove etched along [$0\bar{1}1$] direction in Br_2-Methanol (2% by volume) for 10 sec. after stripping the photoresist.

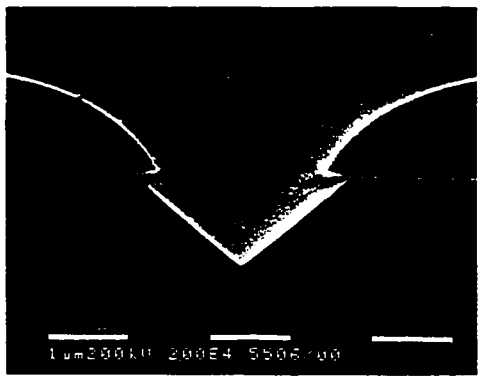
1um200kV 200E4 5506.00

a

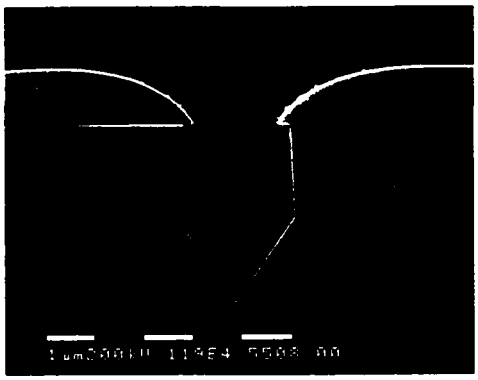
1um200kV 119E4 5508.00

b

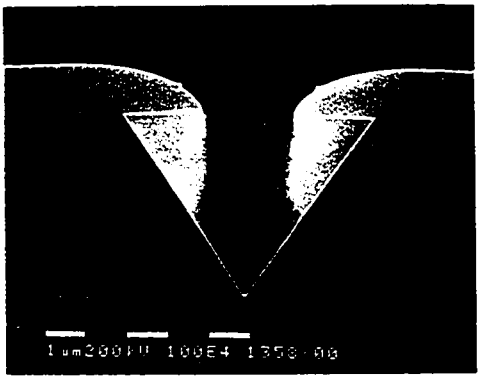
1um200kV 100E4 1350.00

c

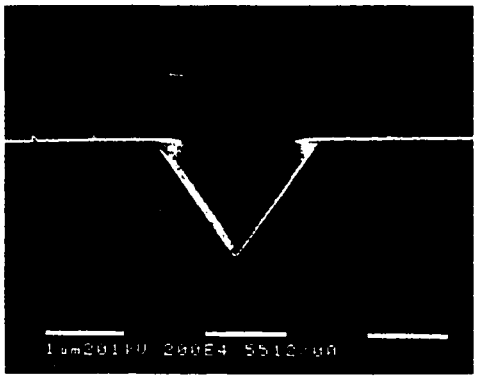
1um201kV 200E4 5512.00

d

Figure 5.13. SEM pictures of etched InP samples that had been de-oxided in the MBE chamber and transferred in vacuum for SiN_x deposition:

a) (211)A V-groove etched along [$0\bar{1}1$] direction in $5HCl:1H_3PO_4$ at 23 °C for 30 sec.;
b) (111)B V-groove etched along [011] direction in $5HCl:1H_3PO_4$ at 23 °C for 30 sec.;
c) (111)A V-groove etched aligned along [$0\bar{1}1$] direction in $2HBr:2H_3PO_4:1K_2Cr_2O_7$ for 2 min.;
d) (111)A V-groove etched along [$0\bar{1}1$] direction in Br_2-Methanol (2% by volume) for 10 sec. after stripping the photoresist.

Fig 5

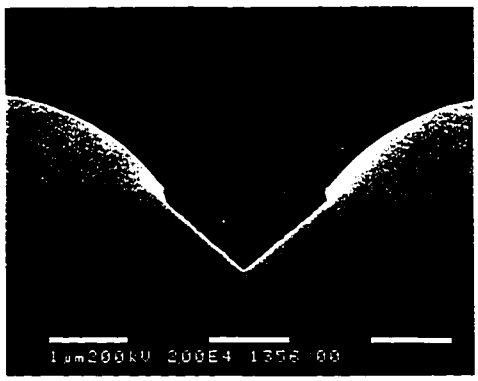
1um200kV 200E4 1356 00

a

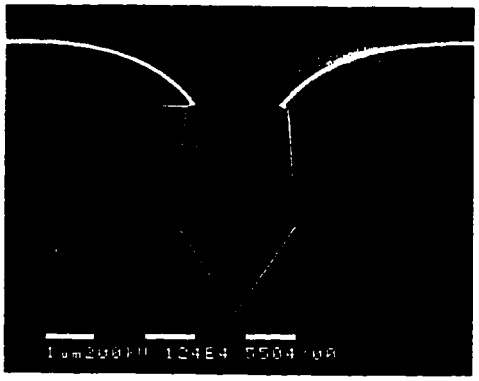

b

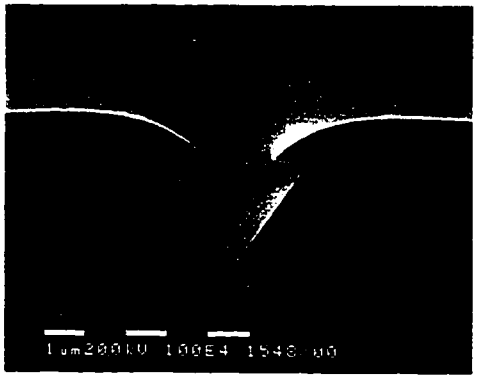
1um200kV 100E4 1548 00

c

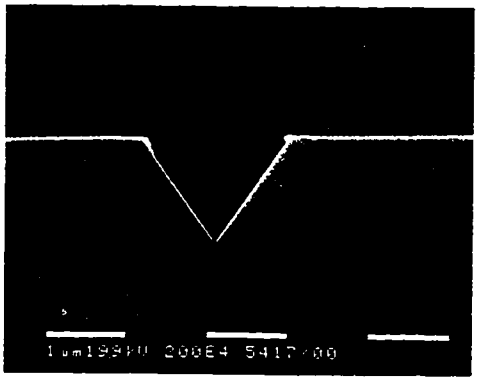
1um199kV 200E4 5417 00

d

Hou (1988a, 1988b) found that it was necessary to minimize the thickness of the native oxide on the InP in order to minimize the degree of undercut when using a photoresist mask.The result of the work reported here provides evidence that the presence of a native oxide at the SiN_X/InP interface is not an exclusive factor responsible for the undercutting but it is responsible for a significant contribution to the amount of undercut. It is clear from Table 5.1 that the etch solution and direction of the groove ([011] or [$0\bar{1}1$]) are also important.

Photoresist masks result in much larger undercut than dielectric masks, as clearly indicated in section 5.2. Notten (1991) argued that this is because mask layers induce changes in the native oxide structures, which have different etch rates. However, the small amount of undercut observed on oxide-free samples implies that the interface structures between the mask and semiconductor, including but not exclusively native oxides, determine the undercutting. It is believed that the different masks may lead to modified bond configuration and electron states at the semiconductor surface, resulting in different undercutting behaviour even without the presence of native oxides. Defect production during the mask deposition process, such as ECR-CVD, could also occur on the semiconductor surface and be responsible for some undercutting. The only situation where undercutting can be completely avoided is by using epitaxial semiconductor etch masks which should have an ideal interface with the substrate. An example of this is shown in figure 5.6 using an InGaAs mask. The result shows that while some undercutting resulted during the mask definition etch, no undercut occurs at the mask-substrate interface as was seen for dielectric and photoresist mask.

In summary, using vacuum interconnected MBE and ECR-CVD chambers it has been possible to deposit a SiN_x etch mask onto an oxide-free (100) InP substrate. In subsequent etching of V-groove features into the InP, mask undercutting is found to be significantly reduced. However, some undercut still occurs depending on the etch solution

and the direction of the etched grooves. The only way to completely eliminate the undercut is to use epitaxial InGaAs deposited onto oxide-free InP as the etching mask.

5.5. Summary

From the above results and analysis, chemical etching can be used to produce different types of grooves on (100) InP substrates, depending on etchant, mask material, mask-substrate interface, mask orientation, etc. (111)A V-grooves can easily be obtained with a dielectric etch mask in etchants containing oxidizing agents. They are extremely sharp at the bottom and smooth on sidewalls. (111)B and (211)A grooves can be formed in $5HCl:1H_3PO_4$, but not in etchants containing oxidizing agents. A certain amount of undercutting is necessary in order to obtain exclusive (111)B sidewalls, but having too much undercutting results in wide flat bottoms. Photoresist etch masks with careful control of the native oxide have been used. (111)B V-grooves with smooth sidewalls, but a small (100) flat bottom can routinely be achieved.

(111)A and (111)B V-grooves have been used for growth studies and QWR fabrication, while (211)A V-grooves were discarded due to the large angle between the sidewalls, compared to the (111) V-grooves. (011) V-grooves were not used either, because of the 45^0 angle between the grooves and (011) habit cleaving planes making them unsuitable for laser fabrication. Finally, the recipes used to etch (111)A and (111)B V-grooves in this work are given in Appendix A.

CHAPTER 6. GROWTH OF InP AND InGaAs/InP QUANTUM WIRES

6.1. Introduction

Homo-epitaxy is usually used to provide a buffer layer to shield the subsequent layers for device structures from the effect of defects in substrates and at interfaces. For QWR growths carried out in this work, an InP buffer layer is required. The growth behaviour of this InP layer is very important to the formation of subsequent crescent-shaped QWRs, especially InGaAs/InP QWRs.

As mentioned in chapter 3, creating a sharp bottom when growing on a rounded or higher-index (e.g. (411)A) faceted bottom is called resharpening and has been observed in the GaAs-based system (Kapon 1994, Shen 1993 and 1994, Pan 1994). However, resharpening is not a trivial process and the conditions for its occurrence are not understood. Indeed, the resharpening process depends on such factors as the growth method, growth conditions, epilayer material, substrate orientation and sidewall plane. For example, the first observation of resharpening was reported for AlGaAs grown by MOCVD (Bhat 1988, Kapon 1994). By contrast, while it has been observed to occur for MBE growth of AlAs, it is not seen for AlGaAs (Shen 1993 and 1994). Resharpening for GaAsP on (111)A GaAs V-grooves has also been reported (Pan 1994). Since resharpening is possible in AlGaAs, significant progress on GaAs-based QWR devices has been achieved (Kapon 1994, Tiwari 1994). However, in the InP-based system, for which fewer studies have been done, it has been reported that deposition on a V-groove etched substrate results in a significant planarization of the structure, the development of a rough sidewall surface, and no resharpening (Bulitka 1993, Bhat 1990 and 1991, Galeuchet 1988 and

Fujikura 1994). Therefore, it is possible that the resharpening is not attainable in the InP-based materials system. Hence, a systematic study on the morphology over a wide range of growth conditions needs to be carried out to determine whether the growth conditions required for maintaining and redeveloping a sharp bottom before and after QWR growth can be established. A second requirement is that a smooth surface morphology be obtained since rough sidewalls near the bottom of a groove will result in irregularities in the dimensions of the QWR.

In this work gas source molecular beam epitaxial growths of InP/InGaAs single quantum well structures or single InP layers have been performed on InP substrates patterned with etched (111)A and (111)B V-grooves. The dependence of the bottom sharpness and the roughness of the sidewall plane, as a function of growth temperature, V/III flux ratio and growth rate has been investigated. Sharp bottoms and smooth sidewalls for both (111)A and (111)B V-grooves have been achieved under certain growth conditions. The growth behavior is discussed considering the incorporation of both group III and group V elements.

Established growth conditions for InP layers would allow crescent-shaped InGaAs QWRs to be formed. Thus, TEM has been used to examine the shape of the InGaAs layers and to observe the existence or absence of extended defects. For the crescent-shaped InGaAs layer formed, a one-dimensional parabolic potential model was used to calculate lateral subband separations. Finally, a simple but unique selective etching process has been used to verify the PL emitted from InGaAs quantum wires.

6.2. MBE Growth Specification

All growths were done in the McMaster GSMBE system. For the deposition of InP, growth temperatures ranged from 400^{o}C to 510^{o}C, V/III flux ratios ranged from 1.4 to 23.2 and growth rates ranged from 0.2 μm/h. to 2 μm/h. Single quantum well

structures were grown, with a 500 Å thick InP buffer, a 50 Å thick, nominally lattice-matched, InGaAs layer and a 500 Å or 1000 Å thick upper InP layer. The InGaAs layer was grown at 490^{o}C with V/III flux ratio of 1.5 and growth rate of 1 μm/h. It is sufficiently thin that its effect on surface morphology can be neglected when surface morphologies of different samples with the same structure are compared.

6.3. The Effects of InP Growth Conditions on the Morphology.

6.3.1. Observation

Figures 6.1 to 6.6 are the SEM images showing representative results of after-growth morphology for variations in the growth temperature, V/III flux ratio and growth rate.

a) Growth temperature

Figure 6.1 (a) and (b) show the effect of growth temperature for a V/III flux ratio of 2.3 and a growth rate of 1 μm/h for (111)A grooves. This flux ratio is typically used for producing good quality deposition on (100) InP substrates. As can be seen, there is less facet development at the bottom for a low growth temperature of 400 ^{o}C (fig. 6.1(a)) compared to a growth temperature of 475 ^{o}C (fig. 6.1(b)). At both growth temperatures, sidewall roughness extends uniformly up the sidewalls, but at the higher temperature the roughness displays a larger periodic scale along the groove direction.

For a (111)B faceted groove, as shown in figs. 6.2 (a) and (b) for growth temperatures of 400 ^{o}C and 475 ^{o}C respectively, a V/III flux ratio of 2.3 and a growth rate of 1 μm/h, a small flat region occurs at the bottom of the groove. The size of the lateral width of this flat bottom increases slightly with growth temperature, while the sidewall roughness decreases significantly at a higher growth temperature.

Figure 6.1. SEM images of (111)A faceted V-grooves with InP grown at a V/III flux ratio of 2.3 and a growth rate of 1 μm/h: a) 400^{o}C, b) 475^{o}C. Epilayer structure: 500Å InP/50Å InGaAs/500Å InP.

a

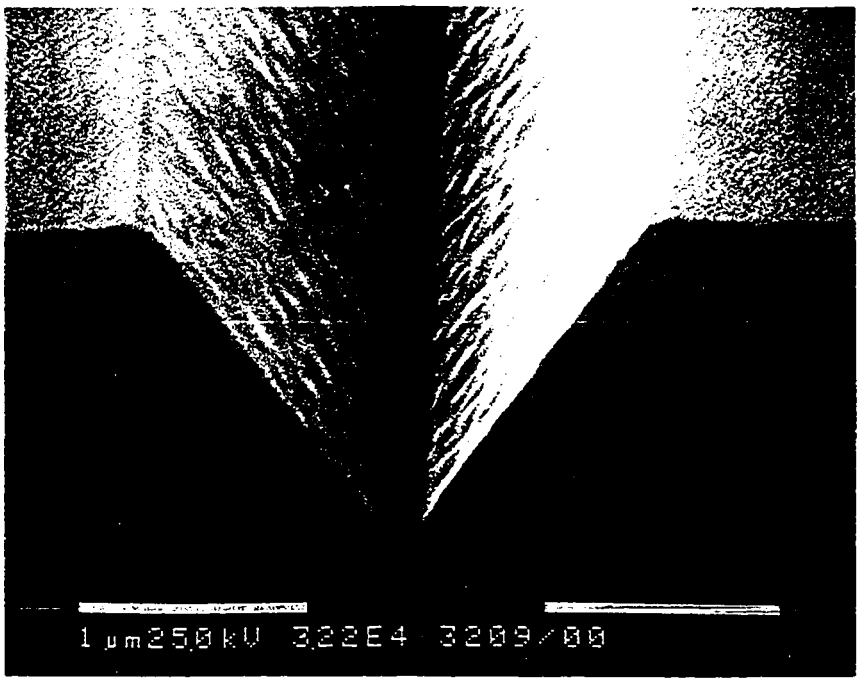

b

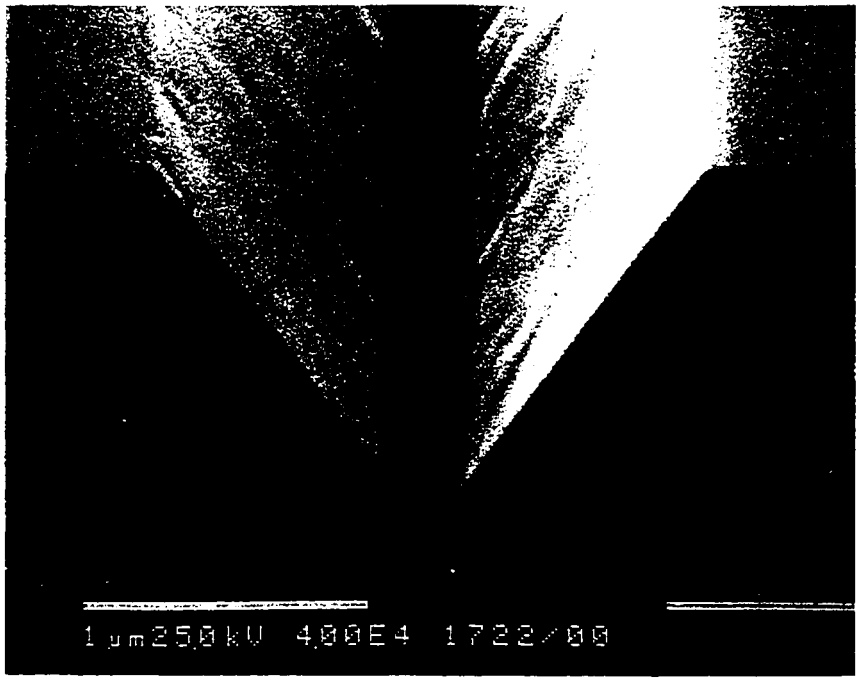

Figure 6.2. SEM images of (111)B faceted V-grooves with InP grown under a V/III flux ratio of 2.3 and a growth rate of 1 μm/h and at: a) 400^{o}C, b) 475^{o}C Epilayer structure: 500Å InP/50Å InGaAs/500Å InP.

Fig. 62

a

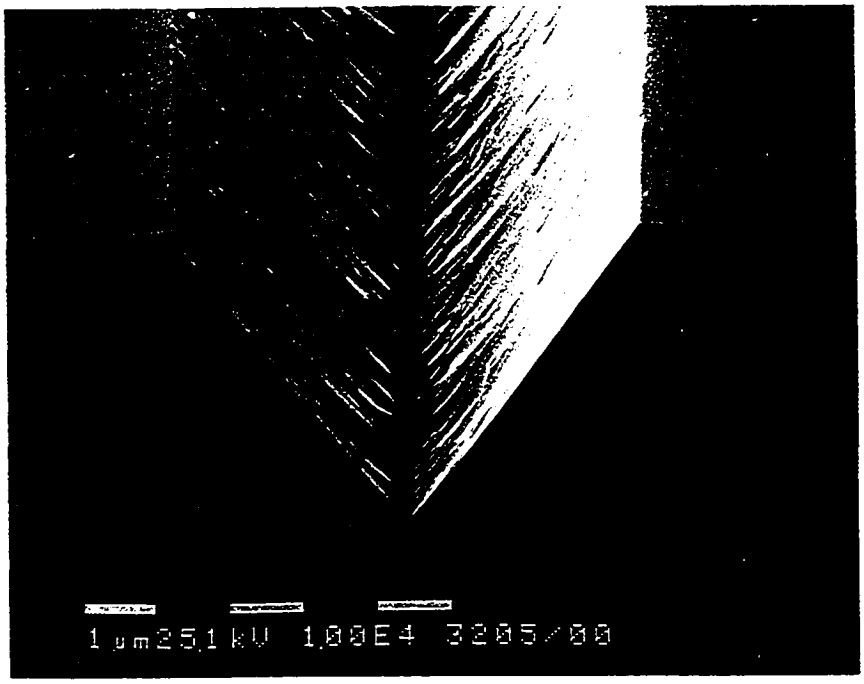

b

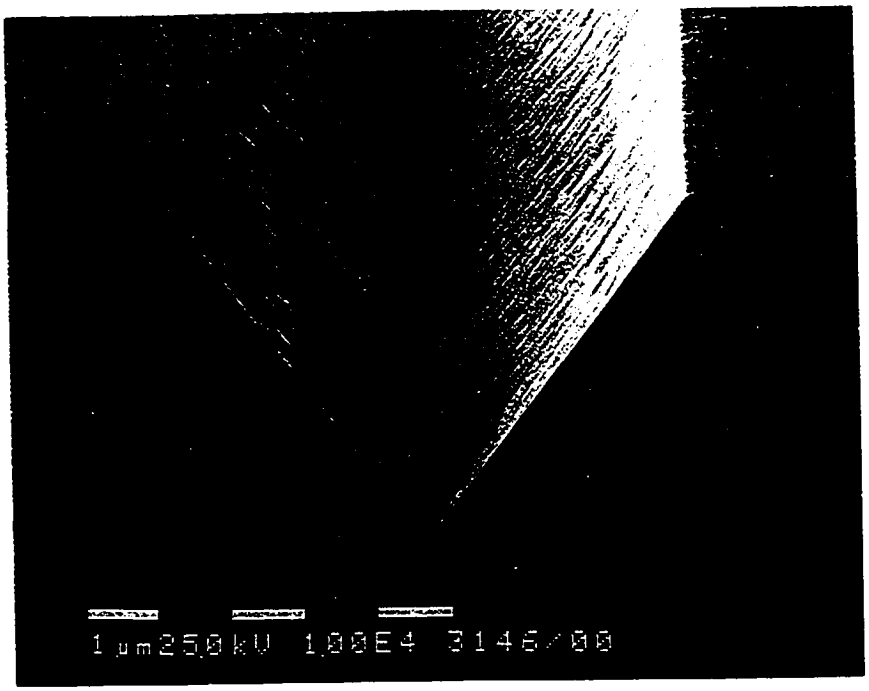

The growth behavior at the bottom of the (111)B grooves is markedly different from that of (111)A V-grooves, i.e. the bottom of a (111)B groove is (100)-like which is seen more clearly at a higher magnification, while that of (111)A groove is composed of high index facets which will be further displayed in TEM cross sections.

b) V/III flux ratio

The surface morphology variation with V/III flux ratio for (111)A V-grooves is shown in fig. 6.3, for a growth temperature of 450^{o}C and a growth rate of 1 μm/h. As seen in fig. 6.3, the shape of the (111)A V-groove bottom, especially the angle of the faceted bottom, is significantly changed by the V/III flux ratio, as is the sidewall roughness. Compared to an almost flat bottom observed for a flux ratio of 3.7 (fig.6.3(a)), the facets in the groove bottom only deviate slightly from (111) and the sidewall is quite smooth at a low V/III flux ratio of 1.4 (fig 6.3(b)).

The effect of the V/III flux ratio on the morphology of (111)B V-grooves is shown in fig. 6.4 for a growth temperature of 450^{o}C and growth rate of 0.5 μm/h. In fig. 6.4(a), the growth displays a strong tendency to accumulate near the bottom of the groove for a higher flux ratio of 12.1. However, when the flux ratio is decreased to 1.4 (fig. 6.4(b)), the bottom of a V-groove is small and the sidewall is smooth.

c) Growth rate

The growth rate also has an effect, even when all other growth conditions are kept constant. Figure 6.5(a) shows the V-groove shape and morphology of a (111)A V-groove for a growth temperature of 480^{o}C, a V/III flux ratio of 1.5, and a growth rate of 0.2 μm/h. The bottom is rough and deviates from (111) facets similar to that shown in fig 6.3(b) for a growth rate of 1 μm/h. Increasing the growth rate to 1.5 μm/h (fig. 6.5(b))

Figure 6.3. SEM images of (111)A faceted V-grooves with InP grown at a growth temperature of 450^{o}C, a growth rate of 1 μm/h. with a) V/III flux ratio of 3.7; b) V/III flux ratio 1.4. Epilayer structure: 2000Å InP.

8U
Fig. 6.3

a

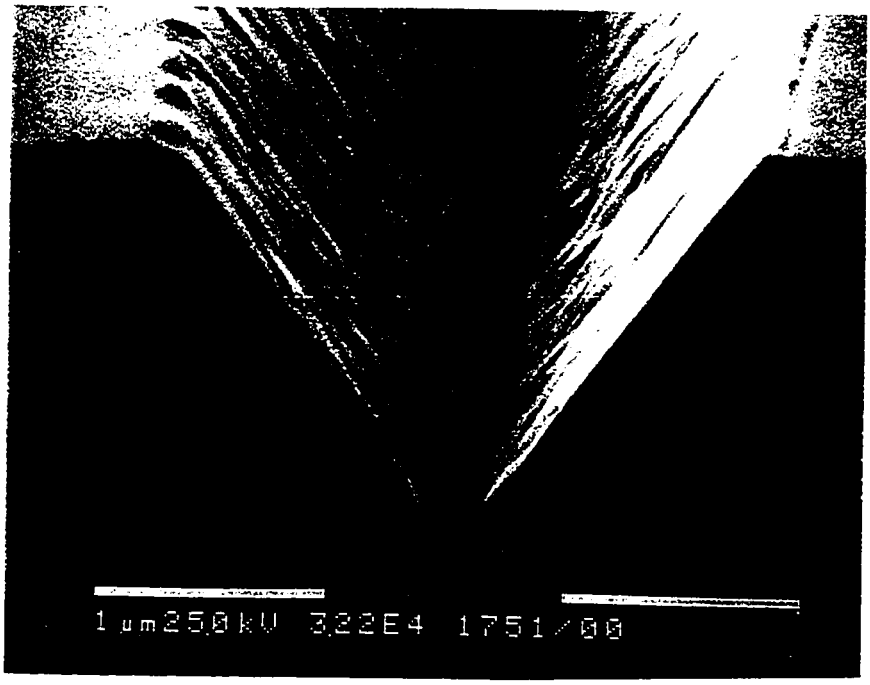

b

Figure 6.4. SEM images of (111)B faceted V-grooves with InP grown at growth temperature of 450^{0}C, a growth rate of 0.5 μm/h. with a) a V/III flux ratio of 12.1; b) V/III flux ratio of 1.4 . Epilayer structure: a) 500Å InP/50Å InGaAs/500Å InP; b) 500Å InP/50Å InGaAs/1000Å InP.

85

Fig. 6 a

a

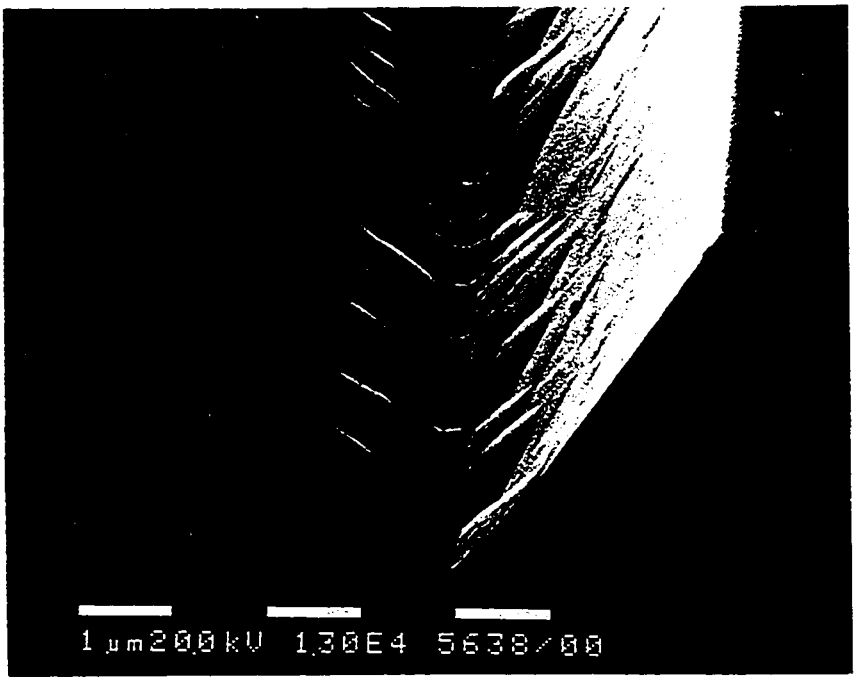

b

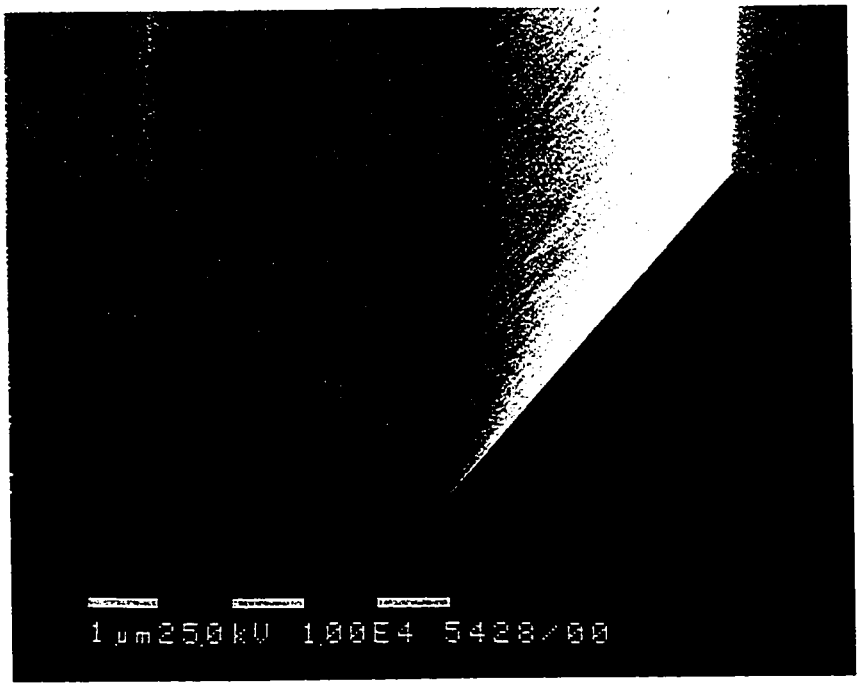

results in smooth, (111) sidewall facets near the bottom and a small higher order faceted region ≈700 Å wide at the very bottom.

By contrast, for a (111) B V-groove with a growth temperature of 450^{o}C and a V/III flux ratio of 1.4, the trend is opposite to that of (111)A V-grooves, as seen by comparing figs. 6.6 and 6.4(b). That is, a lower growth rate improves the sharpness, such that if the growth rate is reduced from 1 μm/h to 0.5 μm/h, the size of the V-groove bottom decreases from 1200 Å to less than 450 Å. In addition, a much smoother sidewall is obtained with the lower growth rate.

The above results can be summarized in the following way,

1. For both (111) A and (111)B V-grooves, a higher growth temperature results in smoother morphology, but more planarization.
2. For (111)A V-grooves:
    2.1 (111)A grooves always have faceted bottoms (approximately (311), (411) or (511) planes) after growth.
    2.2 The width of the bottom region decreases with decrease in V/III flux ratio.
    2.3 Sharper V-bottoms are obtained at a higher growth rate.
3. For (111)B V-grooves:
    3.1 (111)B V-grooves do not display high index facets but possess a flat (100) bottom.
    3.2 The width of the bottom region decreases with a decrease of the V/III flux ratio.
    3.3 Sharper V-bottoms are obtained at a lower growth rate.

Figure 6.5. SEM images of (111)A faceted V-grooves with InP grown at a growth temperature of 480^{o}C, V/III flux ratio of 1.5 and: a) a growth rate of 0.2 μm/h; b) a growth rate of 1.5 μm/h. Epilayer structure: 500Å InP/50Å InGaAs/500Å InP.

Fig. 6-5

a

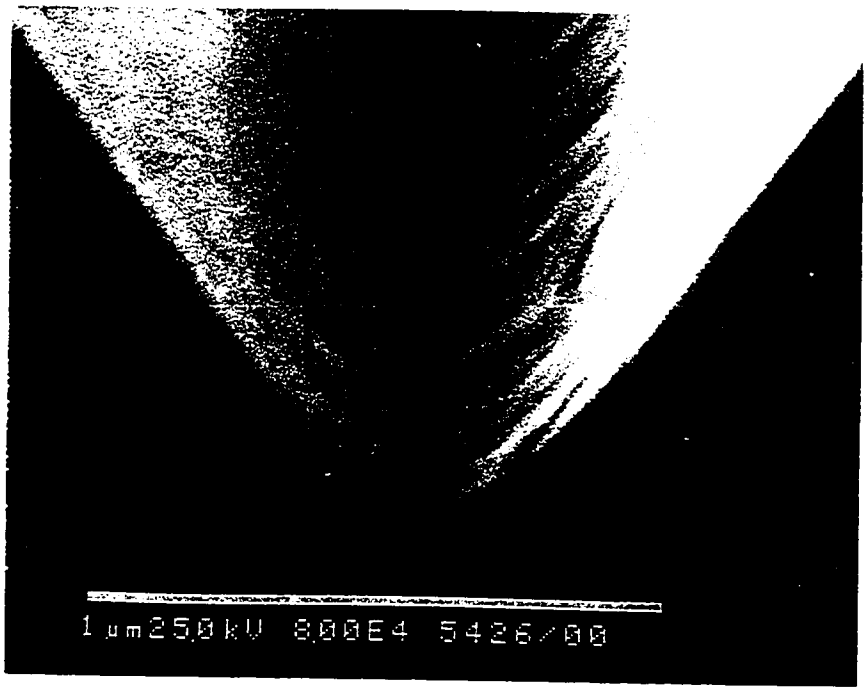

b

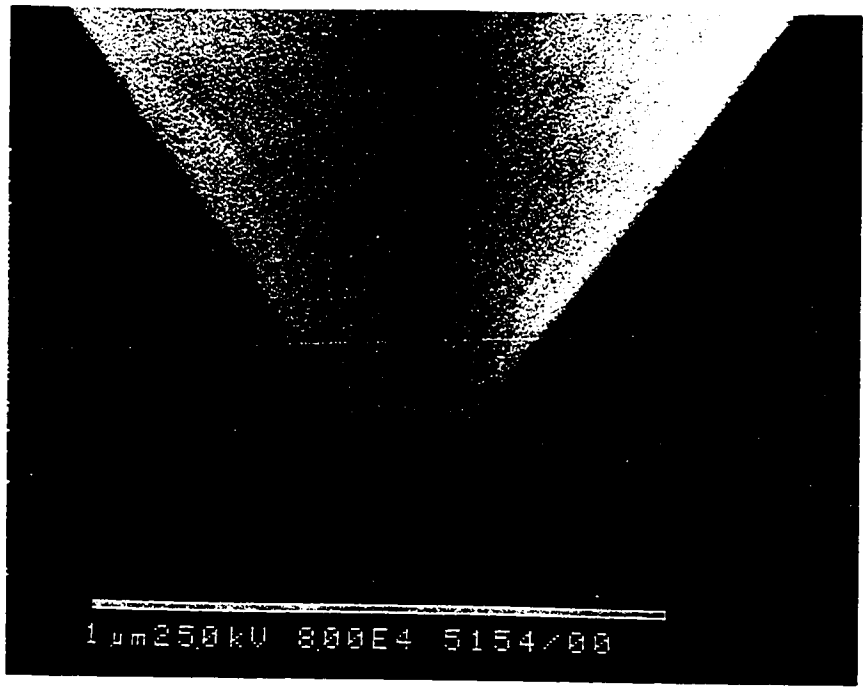

Figure 6.6. SEM images of (111)B faceted V-grooves with InP grown at a growth temperature of 450^{o}C, a V/III flux ratio of 1.4 and a growth rate of 1 μm/h. Epilayer structure: 500Å InP/50Å InGaAs/1000Å InP.

Fig 66

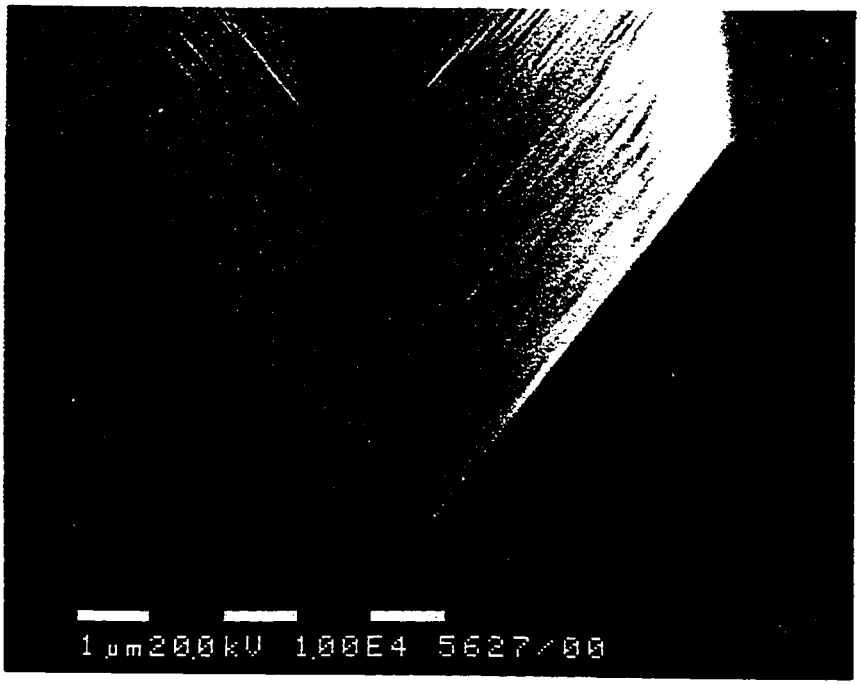

6.3.2. Discussion

Several mechanisms have been proposed to explain growths on patterned substrates. These consider the relationship between the number of dangling bonds and the incorporation of group III elements (LaPierre 1995, Finnie 1996, Asai 1987); step and/or kink density (Finnie 1996, Asai 1987); ledge-ledge interaction (Guha 1993) and the number of unbonded valence electrons (LaPierre 1995, Li 1993). However, these models do not fully explain the current experimental results. In particular, they cannot answer why planarization happens on both (111)A and (111)B V-grooves under some growth conditions (observations 1, 2.1 and 3.1 above).

Consideration of both the diffusion behaviour of the adatoms and the change in local incorporation rate on the different exposed planes, and at regions where different planes intersect, can be used to explain some of the experimental observations. Both diffusion and incorporation rate are functions of position, e.g. the incorporation on a (100)-like V-groove bottom is significantly different from that on a (111) sidewall. Also, changes in the incorporation rate and the lateral diffusion flux are always correlated, as expressed by equations 3.2 and 3.5, and both are influenced by the growth parameters. For example, the incorporation life-time of group III species will be coupled to group V incorporation and the local growth rate will be limited by the supply of group V species. Also, changes in the local growth rate will result in the development of concentration gradients in the adatom distribution. A quantitative analysis on adatom migration and incorporation behaviour using equations 3.2 and 3.5 should be very useful towards understanding the InP growth behaviour; however, this has been buffered by the complexity of experimental observations and boundary conditions, as well as the availability of parameters such as diffusion coefficients. Nevertheless, some qualitative analysis can be performed.

Smoother sidewalls and a flatter bottom at a higher growth temperature (observation 1) are consistent with a higher adatom surface diffusion coefficient on sidewalls, and a

higher incorporation probability at the V-groove bottom leading to a higher growth rate in this region. Hence, in order to ensure a sharp bottom to the groove, the growth conditions need to achieve a balance between limiting the adatom migration to the V-groove bottom such that the growth rate in this region is not too high, whilst also allowing sufficient migration to yield a smooth morphology on both the sidewall and bottom.

Consider initial (111)A InP sidewalls terminated with indium atoms. These have only single dangling bonds for phosphorus incorporation, which presumably does not favour P_2 dissociation/incorporation compared to a (100) plane. In contrast, the incorporation of indium on an initial (111)A sidewall after regions have been covered with P atoms will be encouraged, since no dissociation is involved and each In atom will become triply bonded to the phosphorus covered surface regions. Therefore, the dissociation of P_2 and incorporation of P will be the determining factor for growth on (111)A V-grooves. In an ideal (111)A V-groove, assumed to have atomic-level sharpness in the bottom, 2 dangling bonds are available for the incorporation of phosphorus at the bottom of the V-groove. This will enhance incorporation of phosphorus at the bottom relative to the sidewalls. The higher P incorporation at the bottom will consequently increase the incorporation rate of In in that region and induce a net migration of In from sidewalls to the bottom, to develop a (100) planar or high index faceted region. This region expands during subsequent growth due to the higher incorporation probability of P on the (100) vs. (111)A surfaces (double dangling bond vs. single dangling bond). Since the incorporation of In, and hence the growth rate, at the bottom of the V-groove will be dependent on the availability of phosphorus, the use of a low V/III flux ratio would decrease the maximum possible growth rate, increase the indium lifetime to incorporation at the V-bottom and decrease the net diffusion of group III adatoms to the V-bottom by decreasing the adatom concentration gradient. Therefore, as in observation 2.2, the low

V/III flux ratio would limit the (100)-like growth and minimize the facet formation, leading to a sharper V-groove.

For an initial (111)B V-groove, there are single dangling bonds for indium to incorporate and subsequent triple dangling bonds for P_2 dissociation and P incorporation after the (111) surface is covered with indium. Since no dissociation is required for indium incorporation, the effect of the number of dangling bonds on its incorporation is less important than for phosphorus on a (111)A V-groove. However, the (111)B V-groove always has a small, flat (100) region at the bottom, where there are double bonds for In incorporation. Compared to the sidewalls, the higher number of dangling bonds at the V-bottom will shorten the local incorporation lifetime of indium. Hence, under most growth conditions the growth rate in the bottom region would be expected to be higher than on the sidewall. The V-groove bottom becomes narrower when the V/III flux ratio is low (observation 3.2), which is consistent with the incorporation at the bottom being limited by the supply of phosphorus. Also, at a low V/III flux ratio, the migration of In on both surfaces is essentially enhanced. Hence, its incorporation at the plane intersection would produce a ledge-like nucleation site for subsequent step-flow growth both across the bottom and up the sidewalls. Under these conditions, with long-range step-flow growth dominating, the small (100) flat region should get no bigger.

The bottoms of (111)A and (111)B grooves show different facet development (observation 2.1 and 3.1). The cause of the difference is probably due to the difference in groove direction with respect to the direction of P-dimer bonds on the reconstructed P-stabilized (100) surface existing in the bottom of the groove. In particular, the P-dimer direction is perpendicular to the (111)B groove direction. Thus, for (111)B V-grooves, higher index facet (e.g. (311)B) development would result in undimerized monatomic P on the (100)-like sections - an energy cost which would prevent facet formation. For (111)A grooves, however, the P-dimers are oriented along the groove direction and high index

facet development can proceed with dimerized coverage on the (100)-like sections of the facets.

The opposite effect of the growth rate on growth behaviour of (111)A and (111)B V-grooves, observations 2.3 and 3.3, is difficult to understand in terms of a simple qualitative argument, and no explanation to account for the observation is provided in this thesis.

TEM examination of InP layers grown in either (111)A or (111)B V-grooves, e.g. fig. 6.7 and 6.8, showed that there were no twins and stacking faults formed in the layers when they were not too thick and the substrates were properly cleaned. This is in contrast to the results obtained on planar (111) substrates grown under normal conditions (Cho 1970, Chen 1991 and Hou 1993). As discussed in section 3.5.1, the InP layers grown in V-grooves being free of twins and stacking faults implies that a step-flow growth mode was invloved in the process.

6.4. InGaAs/InP Quantum Wires

As demonstrated in the above section, good surface morphology could be achieved in either (111)A or (111)B V-grooves under different optimized InP growth conditions. Samples grown under those conditions should have the best chance for forming crescent-shaped InGaAs/InP QWRs. Hence the microstructure and properties of InGaAs/InP quantum well stuctures are further investigated.

6.4.1. TEM examination

Corresponding to fig. 6.5 (b), fig. 6.7 is a cross-sectional TEM image of the 50Å thick InGaAs quantum well structure grown in a (111)A V-groove, in which a crescent-shaped InGaAs wire is clearly shown. The maximum thickness of the wire is 22 nm and the width of the wire is about 60 nm. The maximum thickness is about 6 times that of the

Figure 6.7. Cross section TEM image (on [$0\bar{1}1$] axis) showing the crescent-shaped InGaAs/InP quantum wire formed in the (111)A V-groove, corresponding to fig. 6.5(b). Epilayer structure: 500Å InP/50Å InGaAs/500Å InP.

93
Fig 67

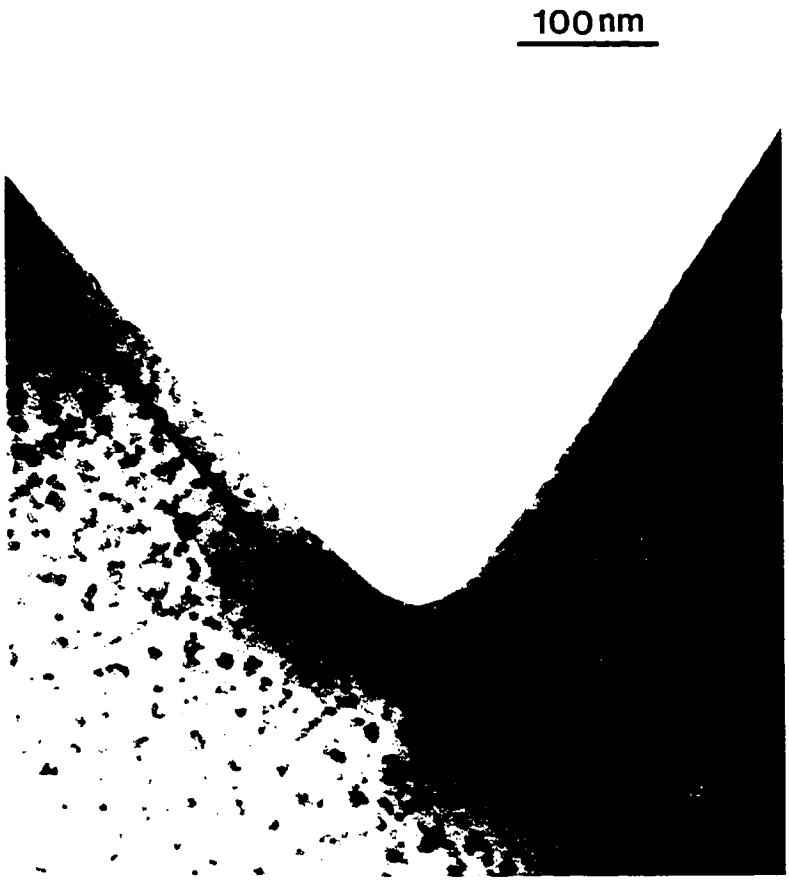

Figure 6.8. Cross section TEM image (on [011] axis) showing the InGaAs/InP layers grown in the (111)B V-groove, corresponding to fig 6.4 (b). Epilayer structure: 500Å InP/50Å InGaAs/1000Å InP.

9/11

Fig. 6a

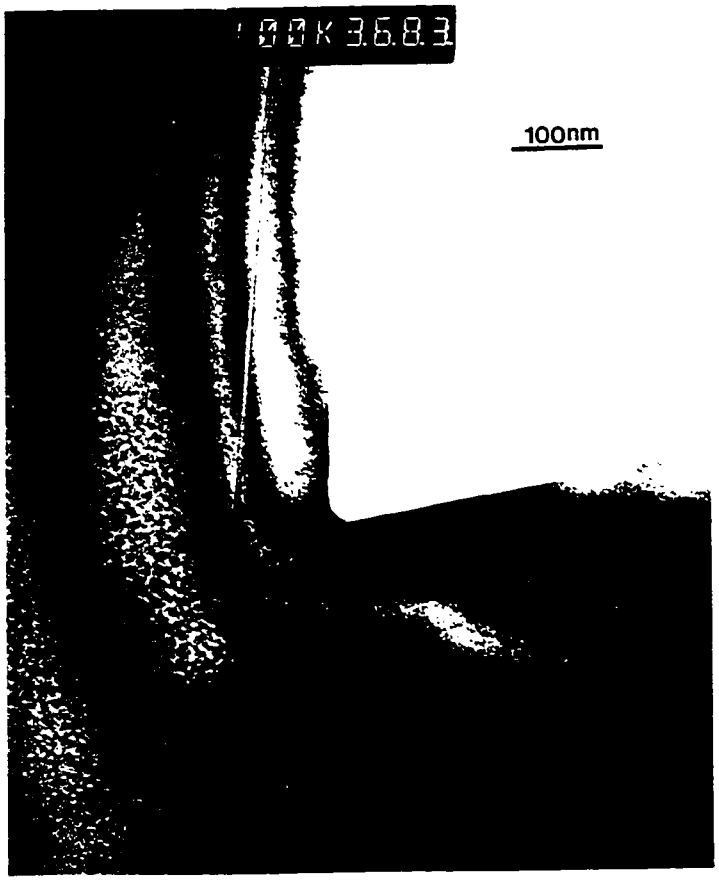

3.5 nm thick quantum wells on the surrounding sidewalls. These dimensions are about the same as those achieved on GaAs-based materials (Kapon 1989a, 1994). The size of the wire could be further decreased by decreasing the nominal InGaAs quantum well thickness. In addition to providing the shape and size of the wire, the TEM examination indicates that there are no defects such as dislocations, stacking faults or twins in either the bottom of V-grooves or on the sidewalls of the grown sample. The defect-free character is important for the optical and electrical properties of devices made with such quantum wires. TEM examination also confirms that InGaAs and InP layers have grown uniformly on the (111)A sidewalls, in contrast to growth by low-pressure MOVPE reported by Galeuchet *et* al (1988) in which no InGaAs growth occurred on the sidewalls. A close inspection of the micrograph in fig. 6.7 reveals faceting evolution in the bottom of the groove. In the bottom of the V-groove, as the InP buffer layer develops, facet formation occurs resulting ultimately in (311)A facets being formed, while the final surface of the cap layer in the V-groove bottom exhibits (411)A facets. There is no resharpening effect observed.

Figure 6.8 is a cross-sectional TEM image of the 50Å thick InGaAs quantum well structure grown in the (111)B V-groove, corresponding to fig. 6.4 (b). In contrast to that of the (111)A V-groove, extended defects form in the bottom. The formation of defects is due to excessive indium migration from sidewalls to the bottom which results in strain and relaxation. This can be eliminated by growing a thinner InGaAs layer, as seen in the next chapter. In the image, the InGaAs layer at the V-bottom, as well as its surrounding region, exhibits the defect contrast, nevertheless, it is clearly seen that the top surface at the V-bottom is flat. Also the top InP layer is very uniform along the sidewalls, confirming SEM observations. The TEM image shows no defects in either the InGaAs or InP layers on the sidewalls.

Thus, the TEM results show that InGaAs/InP QWRs have been obtained in (111)A V-grooves, while the InGaAs/InP shows defects in the (111)B V-groove bottom.

6.4.2. Estimation on lateral quantum confinements

For the InGaAs/InP QWRs obtained in the (111)A V-grooves, the simplified lateral one-dimensional parabolic potential model, as discussed in Chapter 2, is used to estimate the lateral quantum confinement. This involves determining the InGaAs layer thickness at different positions from the TEM images in order to calculate the associated confinement energies. EDS results, in the next chapter, show that the composition variation at the very bottom region is quite small, so that an averaged composition of $In_{0.65}Ga_{0.35}As$ is used for the confinement energy calculation, with the effect of strain included. As shown in fig. 6.9, the confinement energy distributions follow parabolic shapes near the center of the wire, for which the lateral subband separations are calculated as 12.3±0.4 meV, 2.5±0.1 meV, 15.7±0.5 meV for electrons, heavy holes and light holes respectively. The effective widths, W_{eff}, of the wire for electrons, heavy holes and light holes are 20.6±0.7 nm, 20.9±0.9 nm and 21.9±0.8 nm respectively. These values are about the same as those obtained on GaAs/AlGaAs QWRs (Kapon 1994). Also, lateral subband separations reported for GaAs/AlGaAs QWRs range from several meV to 22 meV (Kapon 1994, Tiwari 1994), as mentioned in Chapter 2. For InGaAs/InP, the ratio of conduction band offset to valence band offset is 40/60, while the ratio for GaAs/AlGaAs is 60/40. These different band offset ratios result in different relative subband separations among electrons, heavy holes and light holes between InGaAs/InP and GaAs/AlGaAs systems. Therefore, there is less lateral confinement for electrons, and larger lateral confinement for holes, for the InGaAs/InP system compared to the GaAs/AlGaAs system. Also, the light holes have even larger subband separation than electrons for the InGaAs/InP QWRs.

According to the model, a thinner InGaAs layer will increase lateral confinement due to the nonlinear dependence of confinement on well thickness. This could be easily achieved. A thinner InGaAs well will also increase the lateral confinement. Decreasing the

buffer layer thickness could also decrease the size of QWR by increasing the sharpness of the bottom. However, a minimum buffer layer thickness is required for reasonable optical properties.

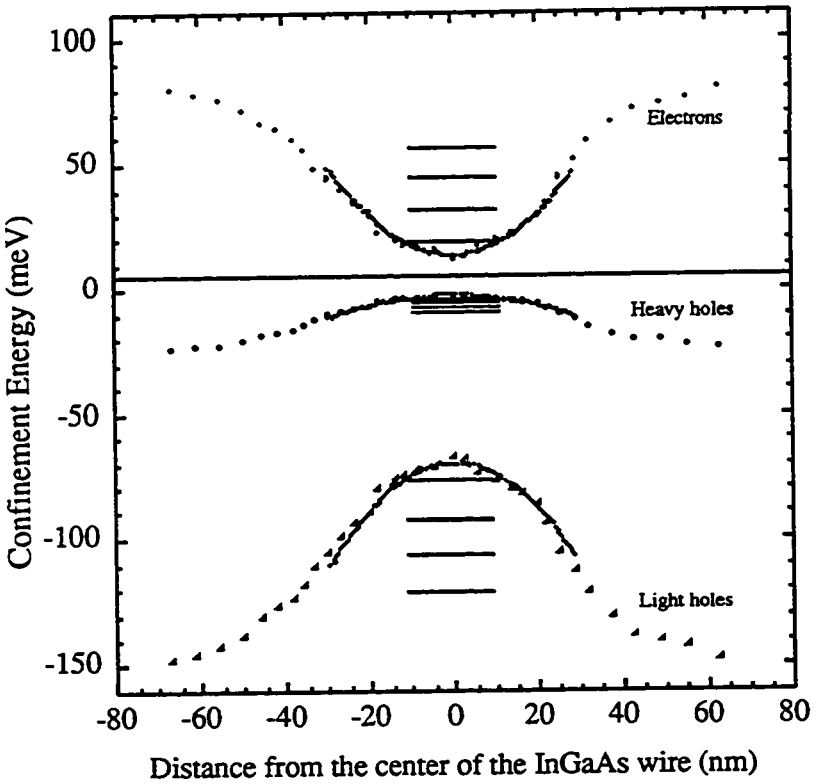

Figure 6.9. Calculated lateral confinement energy distributions and schematic QWR subband energy levels for the InGaAs/InP QWR. (Solid lines are curve-fitted parabolic profiles)

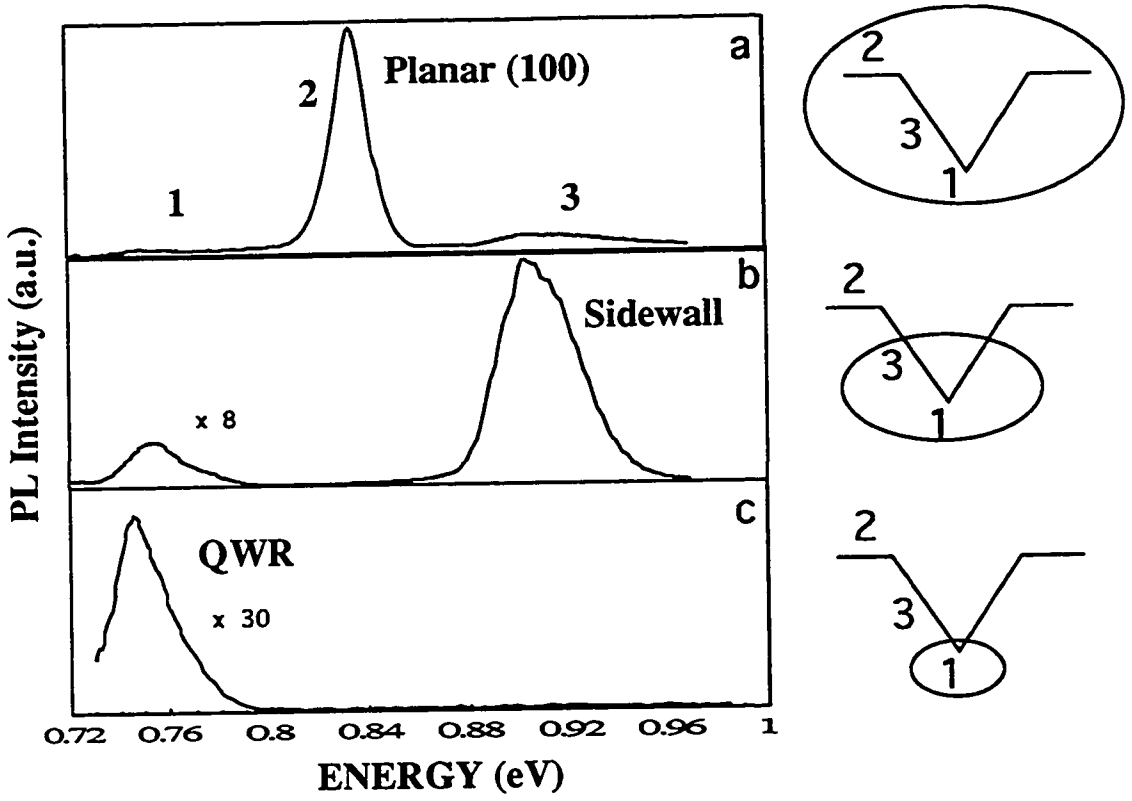

Figure 6.10. Photoluminescence spectra at 11K from the InGaAs/InP QWRs grown in (111)A V-grooves (a) a sample before selective etching; (b) a sample with quantum well on a (100) planar region partially wet-etched away; (c) a sample with all quantum wells etched away except close to the InGaAs wires at the bottom of the V-grooves.

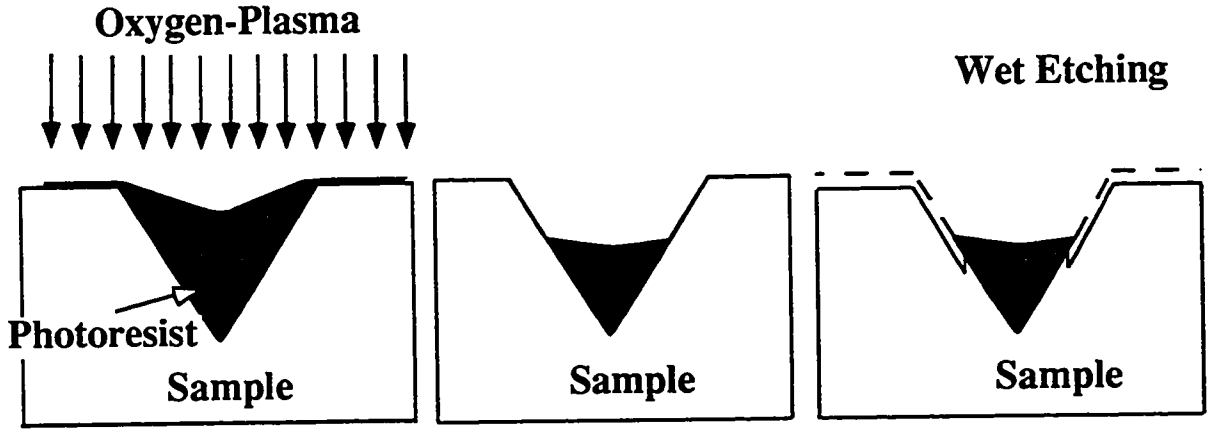

Figure 6.11. Schematic diagrams showing selective etching for photoluminescence.

6.4.3. A selective etching technique and photoluminescence from QWRs

Conventional low temperature PL measurements on the QWR sample with groove period of 5 μm were performed at 11 K. The Ar^+ laser with a spot diameter of about 250 μm typically covers 50 grooves. Figure 6.10(a) is the PL spectrum from a patterned region, displaying multiple peaks labeled 1, 2 and 3.

To clearly identify the sources of these PL emission peaks, a selective etching technique has been developed, as schematically shown in fig. 6.11. Photoresist (PR) was applied onto the grown sample so that the grooves were filled. The PR layer on the sample was baked at 130 ^{o}C for 5 min and then thinned down using an oxygen-plasma, such that the PR on the planar region and part of sidewalls was removed. When the PR in the lower parts of V-grooves reached a certain width, $2HBr:2H_3PO_4:1K_2Cr_2O_7$ was used to etch the planar (100) region and successively remove more groove sidewalls from the top down. To further decrease the size of the non-etched region in the very bottoms of the grooves, controlled undercutting, together with a very small photoresist width at the groove bottoms was used. This makes possible direct examination of the PL emitted from the V-groove bottom, with the quantum wells removed from all other locations.

Figure 6.10(b) is the PL spectrum obtained after the top (100) planar regions were selectively etched away. Peak 2, with energy of 0.832 eV on curve 6.10(a), is absent, indicating that it originated from the planar quantum well region between the V-grooves. The remaining peaks, 1 and 3 in fig.6.10 (b) originated from the V-groove bottom and the sidewall. Additional controlled etching to remove the sidewalls removed peak 3 and left peak 1, as shown in fig 6.10(c). The slight energy shift of peak 1 in fig. 6.10(c) from that in fig. 6.10(a) and 6.10(b) is due to growth nonuniformity across the wafer. Therefore, peak 3, with an energy of about 0.902 eV, arises from the sidewall quantum wells, and peak 1, with an energy of 0.75 eV, is identified to be from quantum wires in the bottom of the V-grooves.

The PL from the planar quantum well regions between V-grooves (peak 2) has a lower energy (0.822 eV) than that of a (100) quantum well region far away from the V-grooves (0.872 eV). This energy shift (50 meV) is due to either thicker quantum wells or higher indium content, or both, in the quantum wells near the V-grooves and results from adatom migration off the (111) groove sidewalls onto the (100) planar regions between grooves. The much higher energy of the sidewall quantum well peak (peak 3) compared to that at a planar region is due primarily to a much thinner quantum well, as well as reduced In content. As far as the InGaAs QWR peak (1) is concerned, its 25 meV full width at half maximum is large compared to that of the planar (100) quantum well peak (2). This broad peak is due to local compositional variation, as well as dimensional and compositional variations of the InGaAs QWRs across the laser spot size. Small lateral subband separations could also generate a high energy tail and broaden the PL peak. Moreover, the 0.75 eV QWR emission has a significant red-shift from both the sidewall quantum well and planar (100) quantum well emission. This is consistent with the expectation that indium is a more mobile adatom than gallium (Kapon 1994). However, the much thicker InGaAs layer in the V-groove bottom indicates that both indium and gallium migrate to the bottom, so the red-shift arises from both greater thickness and increased indium content. A quantum well calculation for a well thickness of 22 nm suggests that the $In_xGa_{1-x}As$ wire composition is $x \approx 0.65 \pm 0.02$. This means that the InGaAs wires are compressively strained, indicating that a gallium rich MBE growth should be employed in order to achieve lattice-matched QWRs.

6.5. Summary

The surface morphology of the InP/InGaAs/InP quantum well structures grown in (111)A V-grooves is significantly different from that in (111)B V-grooves. However, the surface morphology appearing in both types of V-grooves could be improved by

optimizing the InP growth conditions; that is, sharp V-bottoms and smooth sidewalls could be achieved. Extended defects were observed at the bottom of (111)B V-grooves, but not in the (111)A V-grooves. Finally, crescent-shaped InGaAs/InP QWRs have been achieved in (111)A V-grooves with their energy subbands being estimated and their photoluminescence peak being identified using a selective etching technique.

CHAPTER 7. GROWTH OF InGaAsP AND InGaAs/InGaAsP QUANTUM WIRES

7.1. Introduction

The simple crescent-shaped InGaAs/InP QWRs demonstrated in the last chapter, are not directly applicable to the fabrication of diode lasers. To make a laser, it is necessary to grow barrier and waveguiding layers with sufficient thicknesses to supply sufficient carrier and optical confinement. In order to achieve this, InGaAsP layers are needed in the InP-based system, and they must be defect-free and produce a sharp V-groove bottom for the quantum well layer (Bhat 1990, 1991). The subsequent quantum well layer should then form a crescent-shape profile with sufficient lateral confinement to act as a QWR and also be free of defects.

A limiting condition is associated with the variation in ternary or quaternary composition and thickness. Of the group III adatoms, indium has higher surface diffusivity than gallium. Thus, in V-groove geometries, it tends to migrate and accumulate in the V-groove bottom, resulting in a thicker layer with higher indium content than on the sidewalls and adjacent (100) planar regions at the top of the groove, as shown in both current and previous works (Bhat 1991, Galeuchet 1988). This would be expected to produce not only planarization but also compressive strain in the bottom of the groove. However, it is important that the critical thickness not be exceeded in this local region at the bottom of the groove or relaxation and defect production will occur eliminating any possibility of device operation (Bhat 1990, Bulitka 1993, Galeuchet 1988). Hence, thick layer growth represents a greater problem for ensuring that the critical thickness is not exceeded than for the thinner quantum well layers. It has been discussed in section 6.4.1. that a thin,

nominally lattice-matched InGaAs layer with a nominal thickness of 5 nm, grown in a (111)B faceted InP V-groove, usually does exhibit lattice relaxation in the bottom of the groove. It might be expected that an InGaAsP layer would result in a similar effect. In addition, as discussed in section 3.5.2, the incorporation of group V elements could also vary across the wafer and this would result in composition variations of group V components which could further increase or decrease the amount of strain.

In this work, using GSMBE we have grown thick quaternary structures on V-grooves with both (111)A and (111)B sidewalls, which are expected to show different growth behaviour. TEM has been used to examine defect formation and layer morphology while energy dispersive X-ray analysis has been used to measure the composition variation along the sidewalls and at the bottoms of the V-grooves. Based on the measured spatial distribution of composition, the strain and energy-bandgap distributions are calculated. These are compared to low-temperature photoluminescence energy-bandgap measurements.

TEM has also been used to examine quantum well morphology and to determine the dimensions of the crescent-shaped InGaAs/InGaAsP quantum wires in (111)B V-grooves. Based on the measured quantum well thickness variation and barrier information from above, the quantum-wire model has been used to estimate lateral subband separations. Optical characterization included spatially resolved photoluminescence (PL) and PL polarization.

7.2. MBE Growth Specifications

A bulk InGaAsP quaternary layer and an InGaAs/InGaAsP quantum well structure were grown by GSMBE onto (111)A and (111)B V-grooves. The quaternary layer sample has a nominal composition of $In_{0.72}Ga_{0.28}As_{0.61}P_{0.39}$ (with a bandgap wavelength of 1.3 μm) and a nominal thickness of 40 nm. In the quantum well structure, the InGaAs layer is nominally lattice-matched to InP and has a nominal thickness of 1.2 nm, much thinner than

the 5 nm used in InGaAs/InP structures in the last chapter; the lower and upper InGaAsP barrier layers, also having a nominal composition of $In_{0.72}Ga_{0.28}As_{0.61}P_{0.39}$, and are nominally 20 nm thick. All InGaAs and InGaAsP layers were grown at a growth rate of 1 μm/h, a substrate temperature of 450 ^{o}C and a V/III flux ratio of 2.6. For the growths of InGaAsP layers, the gas flow rates of AsH_3 and PH_3 were 1.26 and 3.7 sccm respectively. Along with the quaternary and ternary layers, InP layers, serving as buffer and capping layers in the above structures were also grown, under conditions previously shown to give sharp V-groove bottoms and smooth morphology. Buffer layers were 50 nm thick, while capping layer thicknesses varied from 50 nm to 500 nm.

7.3. Results on InGaAsP

7.3.1. TEM examination

Figure 7.1 is the TEM image of the InGaAsP layer, sandwiched between InP buffer and capping layers, grown on a (111)A V-groove. It shows no extended defects at the V-groove bottom, but a dramatic planarization at the V-bottom region is evident. After the growth of the InP buffer layer, the V-groove bottom is faceted with (311) planes and is only 20 nm wide. Subsequently, the top surface becomes flat and expands to 80 nm width after the growth of the InGaAsP layer. This result implies that the growth behaviour of an InGaAsP layer in a (111)A V-groove is an obstacle to the formation of QWRs. This is further demonstrated in fig. 7.2, which is the TEM image of a 3-quantum well structure grown on a (111)A V-groove. It is seen that all three InGaAs layers not only are wide at the bottom, but also have no significant thickness variation, which is necessary to produce lateral quantum confinement. Thus, InGaAs/InGaAsP QWRs cannot be obtained in a (111)A V-groove, even though InGaAs/InP QWRs have been achieved in such a type of V-groove.

Figure 7.1. The cross-sectional TEM image of InGaAsP/InP structure at the bottom of the (111)A V-groove.

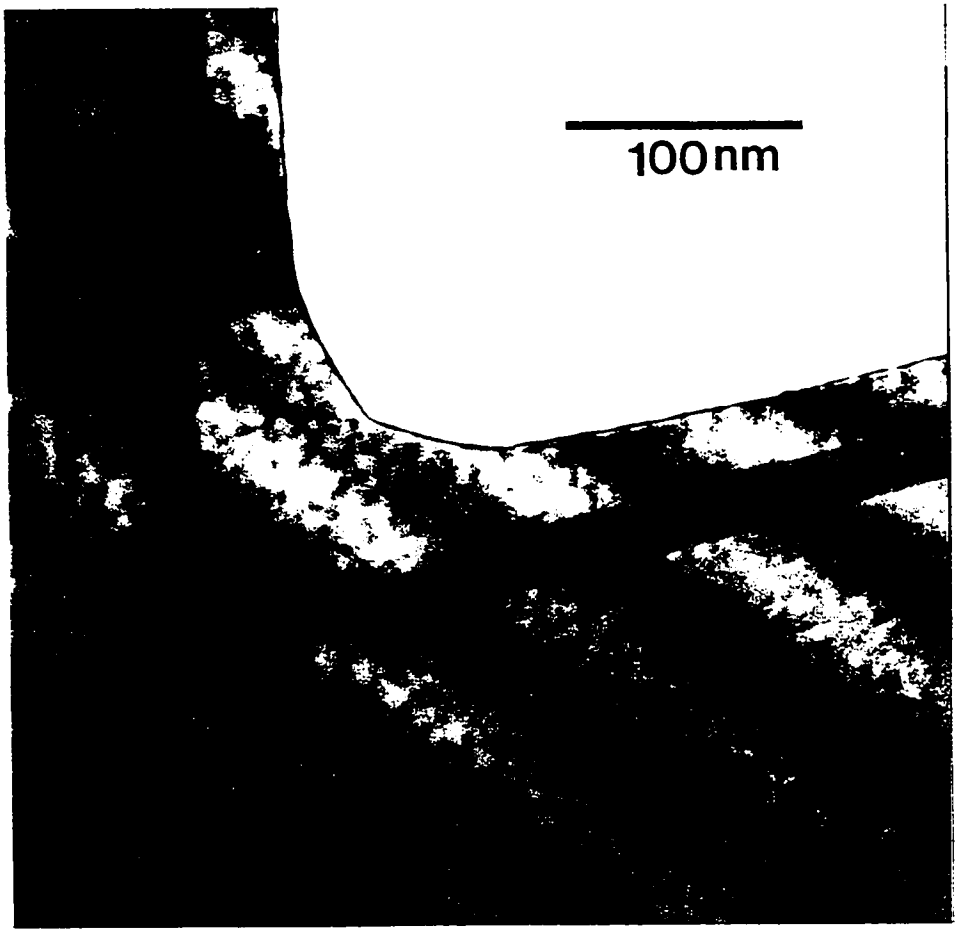
100nm

Figure 7.2. The cross-sectional TEM image of InGaAs/InGaAsP 3 quantum well structure at the bottom of the (111)A V-groove.

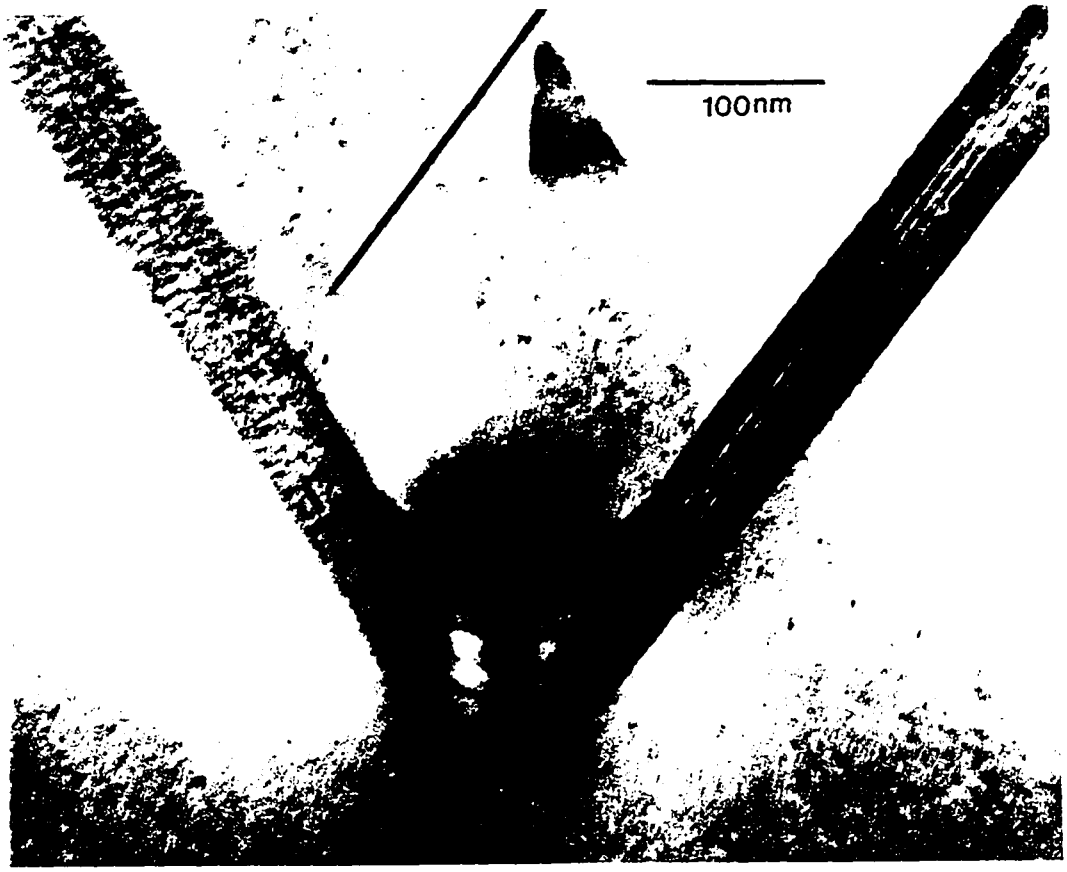
100nm

Figure 7.3. The cross-sectional TEM image of InGaAsP/InP structure at the bottom of the (111)B V-groove.

Fig 7.3

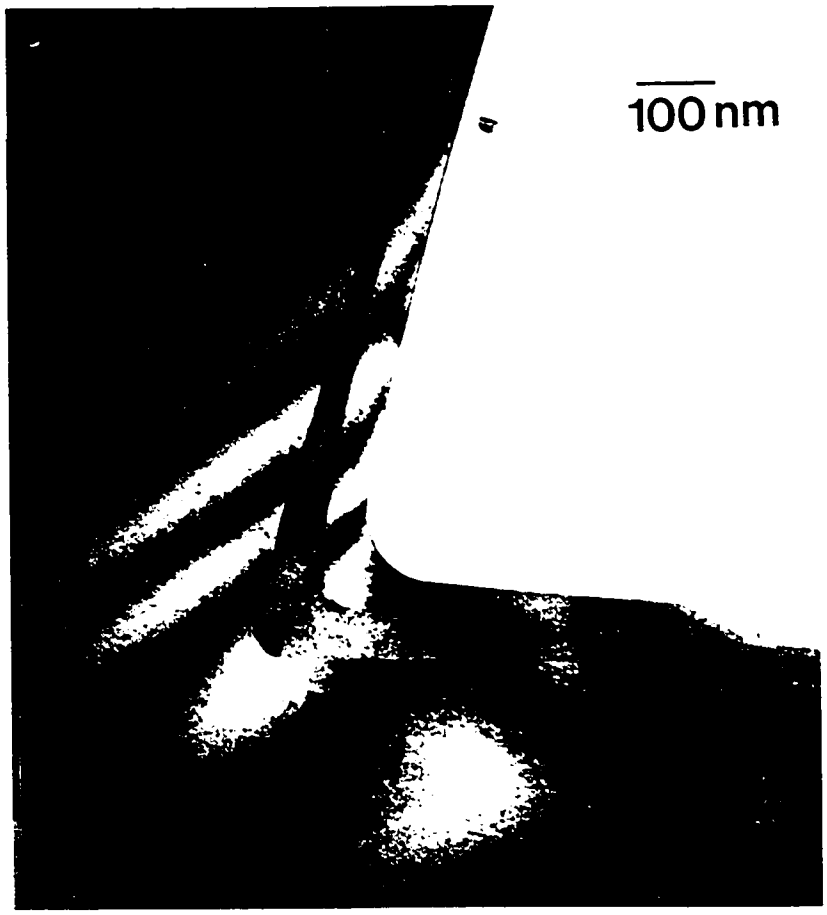

In contrast, the InP and InGaAsP layers grown on a (111)B V-groove show a quite different layer morphology (see fig. 7.3). After the growth of the InP buffer layer, the V-groove bottom is fairly flat (about 30 nm wide). However, the subsequent InGaAsP quaternary layer evolves during growth so that its top surface in the V-groove bottom is quite sharp; i.e. it develops into a rounded bottom with a small radius of curvature. This feature indicates that the InGaAsP growth behaviour on a (111)B V-groove is different from that on a (111)A V-groove, in a way which could be used for quantum-wire formation. Other features can also be seen in the figure. The InGaAsP layer is seen to become thicker towards the V-groove bottom and is free of any extended defects. Assuming no adatom migration, the expected thicknesses on a (100) plane and a (111) sidewall are 40 nm and 21 nm respectively. However, the thickness of the layer is about 100 nm at the bottom of the groove while on the sidewalls far from the bottom, it is thinner than 20 nm, indicating significant migration of the group III species during the growth. Note that the thickness of the InP capping layer on the sidewalls is much more uniform and the top InP capping layer flattens the V-groove bottom again, implying differences in surface diffusivity and incorporation life-time between InGaAsP and InP under their different growth conditions. The causes for the different growth behaviour of InGaAsP on (111)A and (111)B V-grooves and the cause for the different growth behavior of InGaAsP to that of InP are not currently understood. However, the cause for the thick InGaAsP layers being defect-free has been studied through composition analysis.

7.3.2. EDS composition analysis and photoluminescence

EDS was performed on the sample of InGaAsP grown in (111)B V-grooves. The EDS probe spot positions are shown schematically in figure 7.4. Figure 7.5 shows the measured InGaAsP compositions at these positions, with standard deviations labeled. As

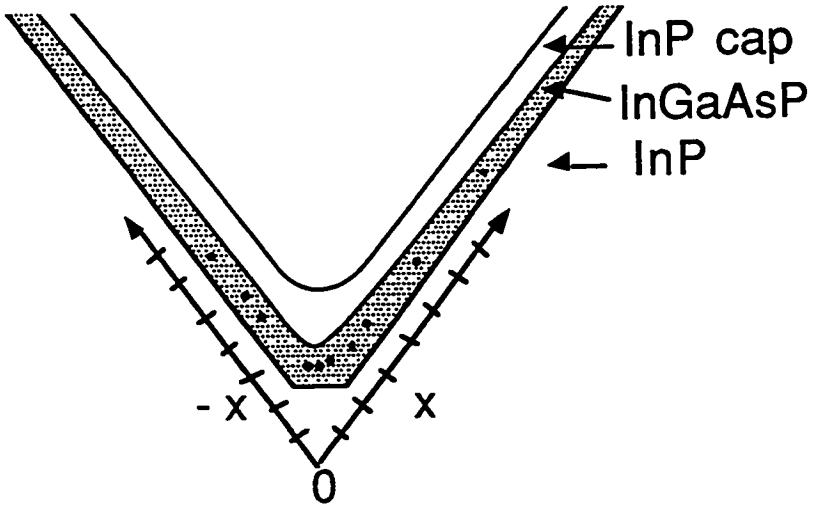

Figure 7.4. A schematic graph showing EDS probe positions (represented by small solid dots)

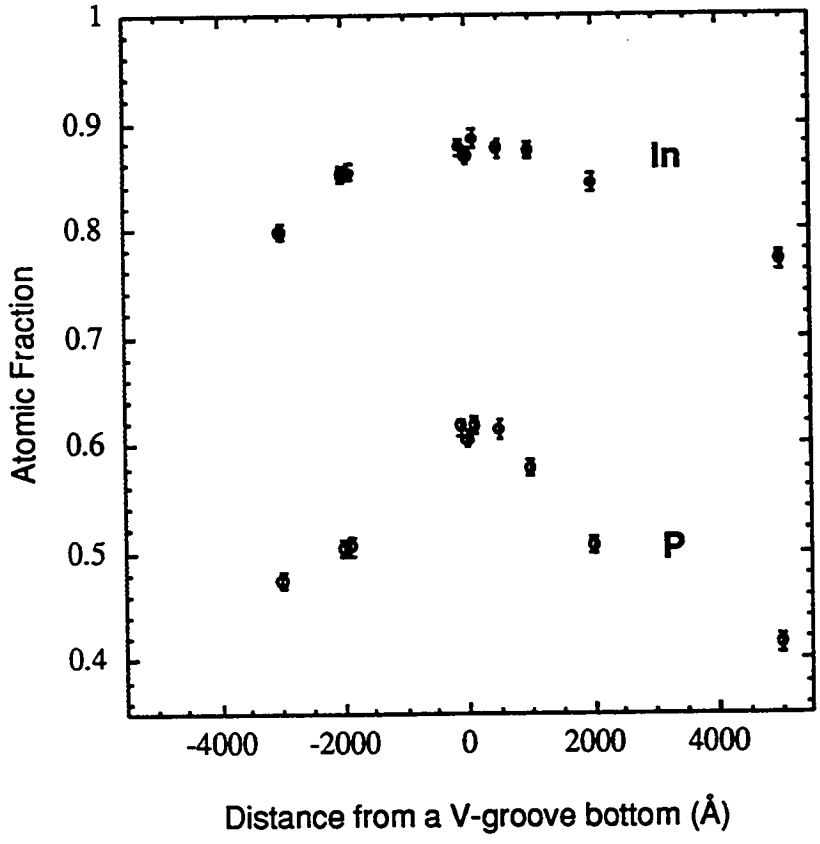

Figure 7.5. Variation of the InGaAsP composition near a (111)B V-groove bottom.

can be seen, the composition in the bottom of the V-groove is In-rich, confirming greater In surface diffusivity. At the bottom of the groove the In content is ≈ 88.0±0.8%, considerably higher than the nominal 72 % which was confirmed on a large area (100) surface region on the substrate. As well, the figure shows that the P concentration is also significantly increased near the bottom of the groove, rising to ≈62.0±0.7% compared to the nominal amount of 39%.

Direct measurement of the strain variation was not possible on the patterned substrate; however, it can be calculated from the measured compositions. Figure 7.6 gives the

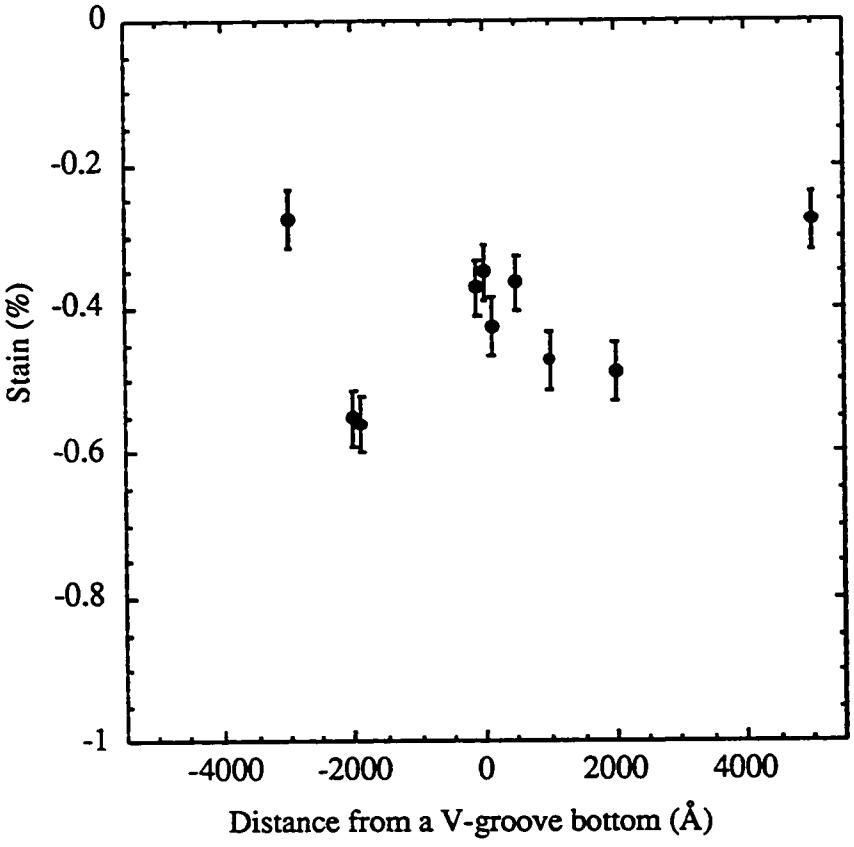

Figure 7.6. The strain calculated from measured composition.

calculated strain distribution near the V-groove bottom. As depicted in the figure 7.6, both the V-groove bottom and lower part of the V-groove are compressively strained. However, the amount of strain is less at the V-groove bottom than that on the nearby sidewalls due to the increased incorporation of P. The lower amount of strain (about -0.36±0.04%) at the V-groove bottom would result in an increased critical thickness allowing a thicker coherent layer.

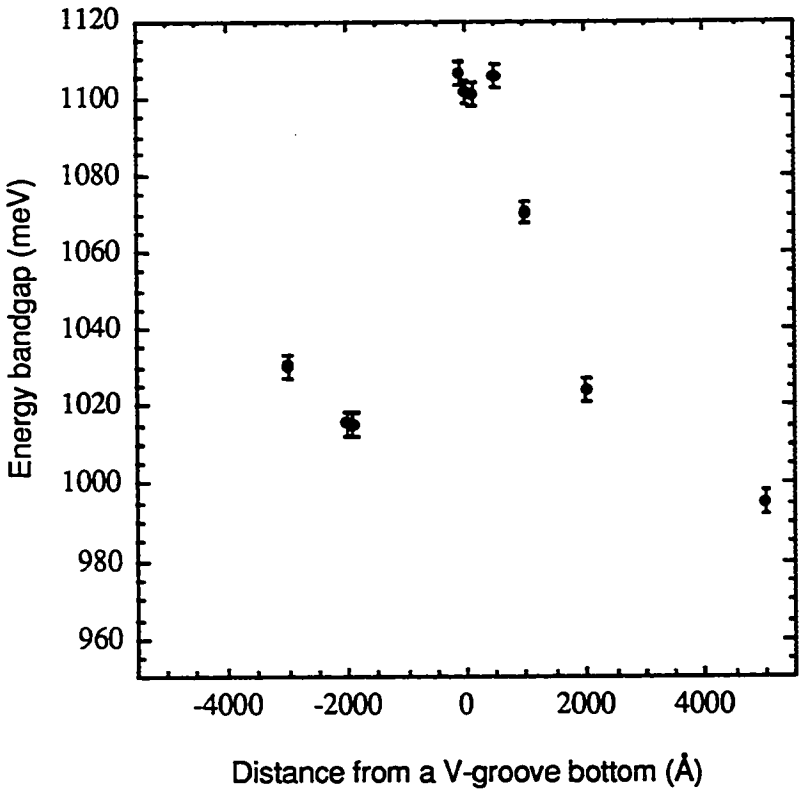

Figure 7.7. The low-temperature energy bandgap calculated from the measured composition.

The energy bandgap at low temperature, for the strained bulk InGaAsP layer (on an InP substrate) near the bottom has been calculated from the measured InGaAsP layer

compositions, including the effects of the strain. This is shown in fig. 7.7. It is seen that the energy bandgap has a value of 1103±3 meV near the V-groove bottom, while the bandgap on sidewalls is smaller and varies from 995±3 meV to 1070±3 meV. The higher energy bandgap at the V-groove bottom has been verified using photoluminescence (16K). Figure 7.8 shows the low-temperature PL spectrum of a selectively etched sample with the planar (100) regions and upper parts of sidewalls removed, (i.e. all but the bottom ~1.5 μm of sidewalls was removed). The intense and broad peak centered at 1.035 eV, with a full width at half maximum of 22 meV, is from the sidewalls, while the small peak at 1.085 eV is identified with the V-groove bottom. Considering the uncertainty of the EDS measured compositions, exciton effects at low temperature, as well as the uncertainty of the energy-bandgap calculation, the energy bandgaps calculated from the measured compositions are in excellent agreement with the low-temperature PL results.

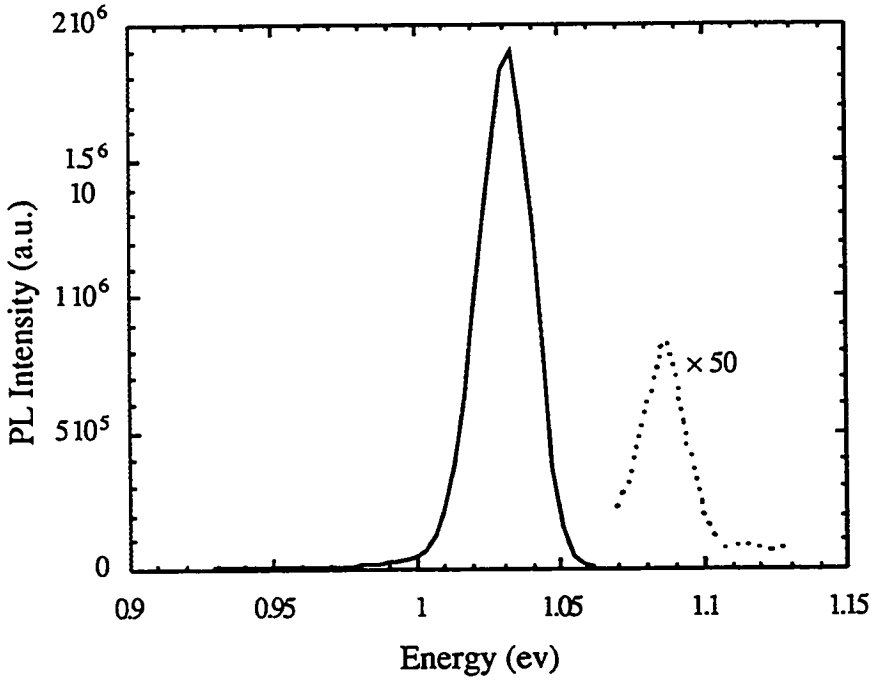

Figure 7.8. Photoluminescence spectrum of the selectively etched sample at a temperature of 16 K.

The thicker InGaAsP layer at V-bottom can be qualitatively understood through the analysis applied to InP growth. Each group V atom on the (111)B sidewall contains a single filled dangling bond for group III adatom incorporation. By contrast, the flat bottom of the V-groove, after deposition of the InP buffer layer, is a (100) surface containing double dangling bonds. This, plus steps and ledges in the bottom region result in more efficient incorporation sites. Therefore, the growth rate near the V-groove bottom would be higher as the incident vapour flux is supplemented with a flux of adatoms diffusing off the (111) B sidewalls to the bottom. The higher indium content measured at the V-groove bottom is consistent with indium having a higher surface diffusivity than gallium.

The higher P concentration of the InGaAsP layer at the V-groove bottom could arise from several effects. From an energy point of view, an increase in the P/As incorporation ratio would act to decrease the amount of compressive strain in the indium rich region. Although Lee *et al* (1995) did not consider this a significant effect, we examined the effect experimentally. Two 30 nm thick InGaAsP layers were grown on a planar (100) InP substrate with different nominal In contents of 70% and 82% but with the same group V fluxes, which ware expected to give a P content around 39.3 % and to produce layers with strain of 0.139% and -0.7% respectively. These InGaAsP layers were analyzed using EDS. However, no differences in group V contents between these two samples were observed, suggesting that the speculation by Lee *et al.* is valid and strain plays no role in the incorporation ratio of the group V species. The next possible explanation is due to the difference in group V incorporation on different surface planes, as mentioned in section 3.5.3. From LaPierre *et al.* (1995), the (100) bottom surface is expected to have slightly lower incorporation coefficients than those on (h11)B sidewall surfaces. However, this factor is not significant enough to account for the observed group V composition variation across the V-groove bottom region. Another explanation for enhanced P incorporation at

groove bottoms derives from the growth-rate variation. At the bottom of the V-groove, the observed growth rate is much higher than that on the sidewall. Assuming a uniform group V gas phase flux across the wafer, the local change in growth rate would be equivalent to a local change in the V/III flux ratio, with a lower ratio at the V-groove bottom than on the sidewall. From Lee *et al* (1995) and LaPierre *et al* (1996), a lower V/III flux ratio results in an As under-pressure situation and a higher incorporation of P at a fixed $As_2/(As_2+P_2)$ flow fraction. This is consistent with the current observation. In addition, it is interesting to notice that the amount of As from incident vapour flux is only 67% of that in the InGaAsP layer at the V-groove bottom, which suggests that the excessive As in the InGaAsP arises from the migration of As or As_2 adatoms from sidewalls to the bottom.

7.4. InGaAs/InGaAsP Quantum Wires

7.4.1. TEM examination and QWR energy level estimation

Due to the growth behaviour of InGaAsP in (111)B V-grooves, crescent-shaped InGaAs/InGaAsP QWRs could be achieved. This is confirmed in figure 7.9, which is the TEM image of an InGaAs/InGaAsP quantum well structure grown on a (111)B V-groove. As seen in the image, all ternary and quaternary layers are free of any extended defects at V-groove bottoms. Moreover, the InGaAs layer at the V-groove bottom clearly shows a crescent-shape. The thickness is about 7 nm at the center of V-bottom, which is nearly 6 times the nominal thickness on a planar (100) region and more than 10 times the estimated thickness on the sidewall. The physical width of the crescent-shaped InGaAs region is about 50 nm. The large thickness variation in such a small width is an indication of possible quantum wire formation. Furthermore, even the top of upper InGaAsP layer is sharp, which implies promise for the formation of multiple InGaAs/InGaAsP QWRs.

Figure 7.9. The cross-sectional TEM image of an InGaAs/InGaAsP single quantum well structure at the bottom of a (111)B V-groove, showing a crescent-shaped InGaAs/InGaAsP quantum wire sandwiched between two InGaAsP layers.


100nm

To estimate the lateral quantum confinement for the InGaAs/InGaAsP QWR, the simplified lateral one-dimensional parabolic potential model was used again. While a constant InGaAs (68% In) QW composition and band-offset ratio of 40/60 are used in the calculation, the barrier composition is the average value ($In_{0.88}Ga_{0.12}As_{0.39}P_{0.61}$) measured in the bottom region by EDS (fig.7.5). The confinement energy distributions also follow parabolic shapes near the center of the wire, for which the lateral subband separations are calculated to be 17.0±0.6 meV, 5.7±0.2 meV and 22.2±0.8 meV for electrons, heavy holes and light holes respectively. The effective widths, W_{eff}, of the wire for electrons, heavy holes and light holes are 22.0±0.8 nm, 13.6±0.6 nm and 20.0±0.7 nm respectively. These subband separations are slightly higher than those of the InGaAs/InP QWR grown on (111)A V-grooves presented in the last chapter and are about the same as those obtained on GaAs/AlGaAs QWRs (Kapon 1994, Rinaldi 1994). Due to different band offsets, there is less lateral confinement for electrons and larger lateral confinement for holes in the InGaAs/InGaAsP system compared to the GaAs/AlGaAs system (Kapon 1994, Rinaldi 1994). The larger light-hole subband separation compared to that of electrons is due to the valence band offset being larger than the conduction band offset. The large subband separation of light holes is of importance to applications such as QWR lasers which require sufficient lateral hole confinement.

7.4.2. Photoluminescence of the InGaAs/InGaAsP QWRs

Conventional low temperature photoluminescence was carried out on the InGaAs/InGaAsP QWR sample grown on (111)B V-grooves to examine the electronic properties of the QWRs. Figure 7.10(a) gives the spectrum from the patterned region of the as-grown sample, displaying multiple peaks, at 0.756 eV, 0.776 eV, 0.892 eV, 0.946 eV (with a shoulder at 0.93) and 0.982 eV. Figure 7.10(b) is the PL spectrum obtained with top planar (100) regions and upper sidewalls selectively removed by etching. These show

that the PL peaks at 0.946 eV and 0.892 eV were from the region removed and suggest that these two peaks arise from a composition and a quantum well thickness variation in the region removed. The peak at 0.982 eV is assigned to the lower part of the sidewalls, which has a high energy due to a reduced quantum well thickness compared to the (100) regions. Thus, peaks at 0.756 eV and 0.776 eV are from the V-groove bottom. Their low energies, compared to that on the planar region, are consistent with the composition (about 70±2% In) as measured by energy dispersive X-ray analysis. The FWHM of the peak at 0.756 eV is about 15 meV, which is narrower not only than that of the quantum well peak on the non-patterned (100) region but also that of InGaAs/InP QWRs grown on (111)A V-grooves (fig.6.10). Also, the broad peak with a high energy tail which was observed on a (111)A V-groove (fig. 6.10) is resolved into two peaks in the spectra on the (111)B V-grooves, suggesting the formation of a quantum wire. The peak at 0.756 eV would then arise from the QWR ground state energy level (1e-1hh), while the peak at 0.776 eV is assumed to be from the higher QWR subband transition (2e-2hh). The 20 meV separation between these two peaks is consistent with the calculated estimate of the energy separations (22.7 ±0.8meV) between 1e-1hh and 2e-2hh transitions. The low PL intensity from QWRs, compared to that of quantum wells on the lower part of sidewalls, is due to its small dimension. The size of the lower part of the sidewalls is about 60 times of that of QWRs. In addition, the QWR PL peaks have relatively long wavelengths. However, they can be tuned towards shorter wavelength through the QWR composition. Decreasing the In content of the InGaAs layer or adding P into the quantum well layer have been successfully used to achieve this. Alternatively, InGaAsP/InGaAsP QWRs, with lower P content in the quantum well layer, can achieve the same QWR effect.

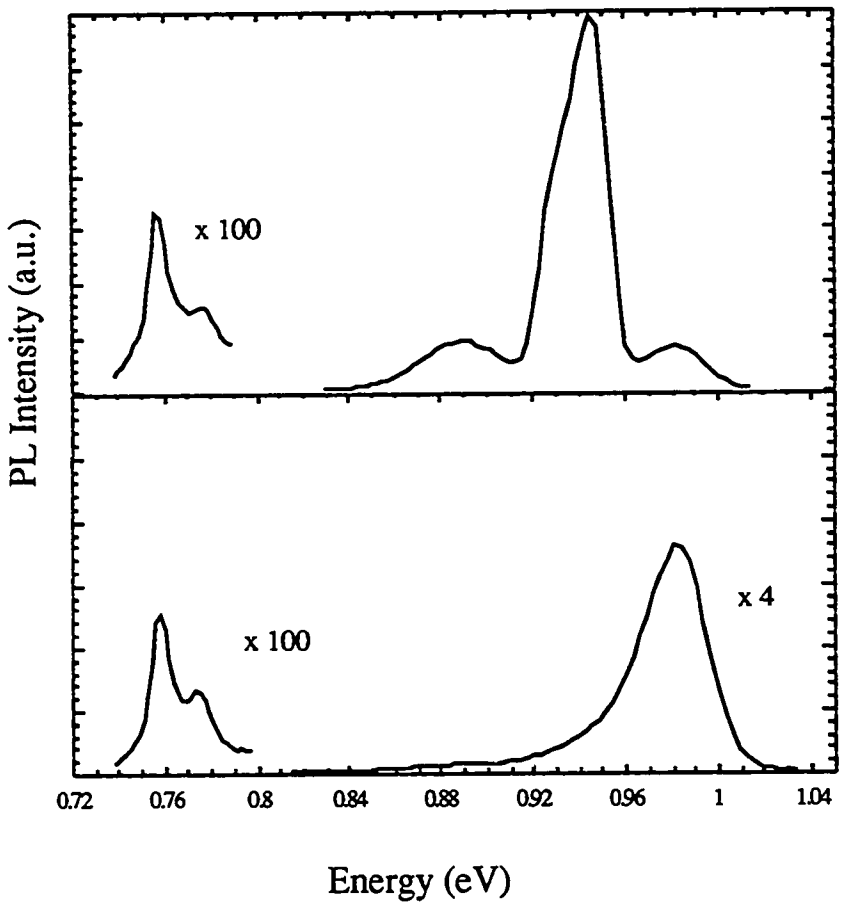

Figure 7.10. 15K photoluminescence spectra of InGaAs/InGaAsP grown in (111)B V-grooves: a) without selective etching; b) with quantum well on a (100) planar region and upper sidewalls partially wet-etched away.

7.4.3. Temperature and pumping intensity dependence of the QWR photoluminescence

The above photoluminescence study suggests that the appearance peak at 0.776eV can be related to bandfilling, producing the first evidence for a QWR structure. This is further supported by the temperature and pumping intensity dependence of the PL. As shown in figures 7.11 and 7.12, the intensity of the 0.776 eV transition relative to that of the lower energy (ground level) transition increases with sample temperature and PL pump power. This can be accounted for by a band-filling effect that is very common in low-

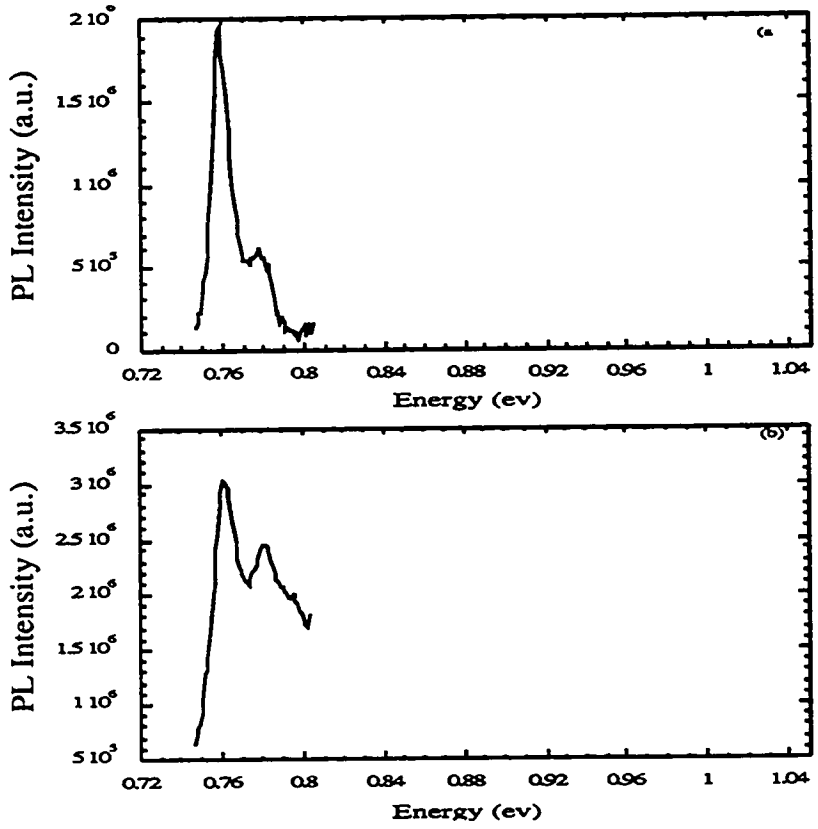

Figure 7.11. Photoluminescence spectra of InGaAs/InGaAsP grown in (111)B V-grooves pumped by a YAG laser with intensity of: a) 0.22mW; b) 220mW.

dimensional structures. This phenomenon has also been observed in GaAs/AlGaAs QWR photoluminescence where the bandfilling argument was experimentally supported by magneto-PL and time-resolved PL measurements (Rinaldi 1994, Maciel 1995). Results of the diamagnetic shift of different transitions in a magnetic field demonstrated that, even under low-power excitation and /or low temperatures, an extremely efficient population of excitons at excited state occurs (Rinaldi 1994). Time-resolved PL showed that ground state transition has a long decay time, whereas 2e-2hh transitions have a relatively rapid decay (Maciel 1995). Strong emission, including lasing, from excited subbands has been reported for electrically pumped GaAs/AlGaAs QWRs by Kapon (1984). Recently, similar results

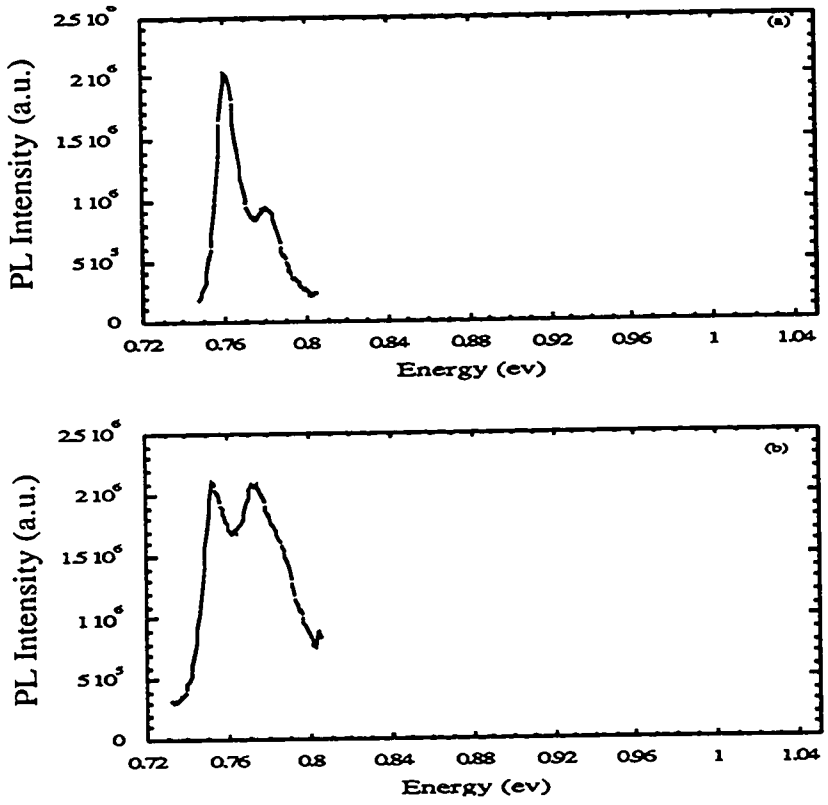

Figure 7.12. Photoluminescence spectra of InGaAs/InGaAsP grown in (111)B V-grooves, pumped by a YAG laser with intensity of 10.5 mW, at: a) 15K; b) 100K.

have been reported for quantum dots. Kamath (1996) reported strong photoluminescence transitions between second energy levels from InGaAs/GaAs QDs. He also did low temperature time-resolved PL measurements and found that the excited state had an order of magnitude shorter decay time constant than the ground state. Ustinov (1996) and Mirin (1996) have reported lasing from excited states for electrically pumped InGaAs/GaAs QDs. So far, the detailed mechanism for bandfilling is not fully understood, however, the bandfilling effects are believed to be associated with a narrow density of states and small subband separations (Rinaldi 1984). The narrow density states requires less carriers to fill a band.

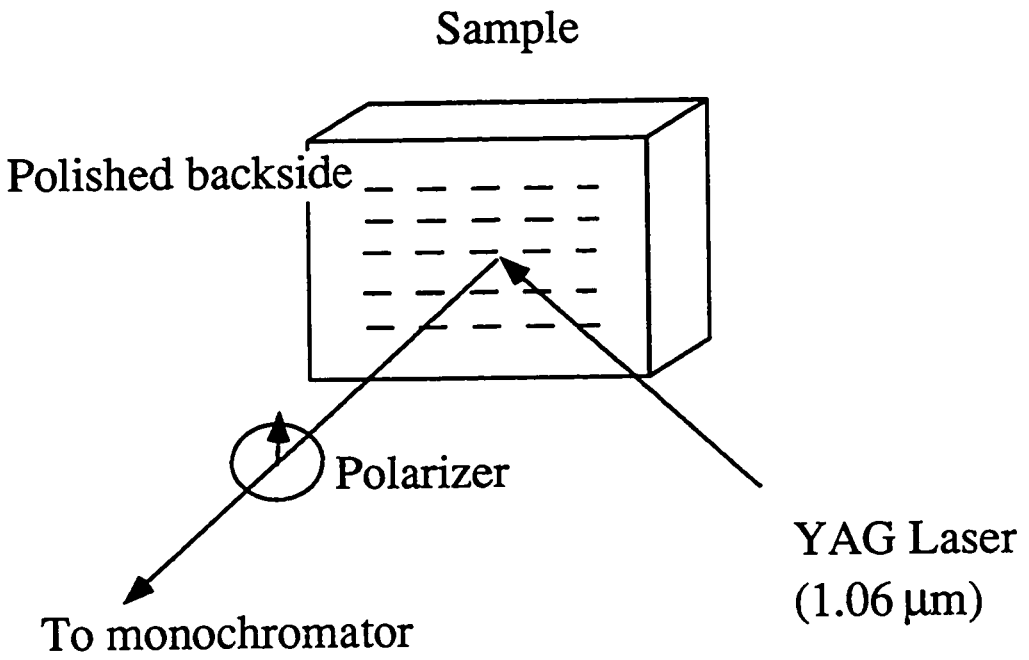

Figure 7.13. Schematic configuration for the photoluminescence polarization study.

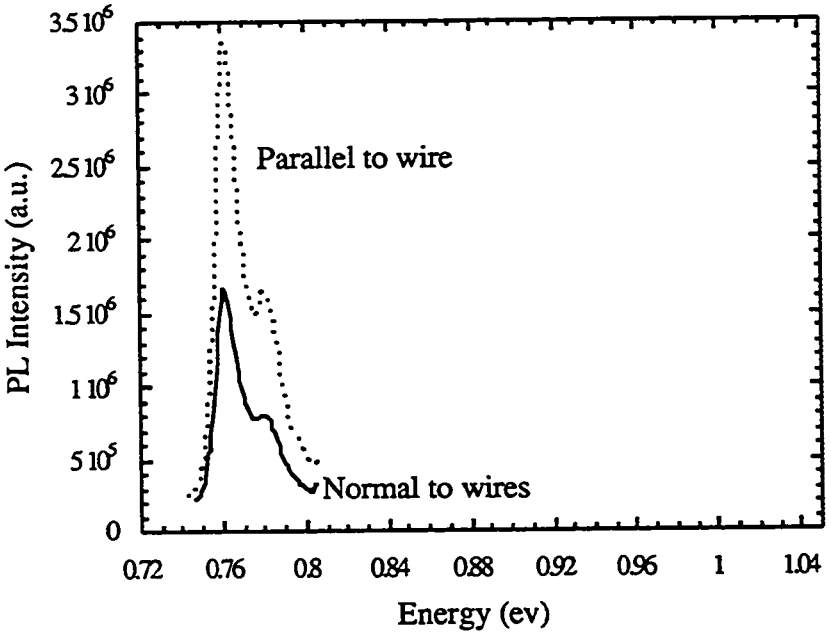

Figure 7.14. Polarization of the InGaAs/InGaAsP quantum-wire photoluminescence at a temperature of 15 K.

7.4.5. Polarization dependence of the QWR photoluminescence

Polarization of PL emission has also been used to confirm the QWR behaviour in this work. This required mechanically polishing the backside of the sample down to ~100 μm, then optically exciting with a cw YAG laser, as shown figure 7.13. The 1.06 μm YAG laser light passed through the InP substrates and selectively pumped the InGaAsP and InGaAs layers. The spectra were calibrated with respect to the polarization response of the PL system (fig. 4.2). Figure 7.14 shows the polarization of the PL emission measured along, and normal to, the wire direction. It is seen that the PL emission is strongly polarized parallel to the wire direction, being more than twice that perpendicular to the wire direction. This polarization behaviour results from heavy-hole transitions in the QWRs (Sercel 1991, Sugaya 1993, Pan 1994). The InGaAs wire is sufficiently strained and thin that the light-hole band is separated from the heavy-hole band, thus the transitions observed in the PL spectra are associated with heavy holes. As discussed in section 2.3, the polarization behaviour is consistent with QWR behaviour.

7.5. Summary

In summary, the growth of InGaAsP in (111)A V-grooves results in a significant planarization and flat V-bottoms; thus, InGaAs/InGaAsP QWRs cannot be obtained in (111)A V-grooves. In contrast, the growth of an InGaAsP layer in (111)B V-grooves leads to sharper, defect-free bottoms. Compositional analysis indicates that enhanced P incorporation at the groove bottoms reduces the strain associated with extra In incorporation due to migration from sidewalls to the bottoms. In (111)B V-grooves, InGaAs/InGaAsP quantum wires have been demonstrated. The QWRs are defect-free and crescent-shaped. A significant thickness variation across a small width results in subband separations comparable to those achieved in the GaAs-based system. The existence of

lateral subbands has been demonstrated in PL spectra and also supported by polarization measurements. The subband separation observed in PL spectra is consistent with a calculated value based on the wire geometry observed by TEM.

CHAPTER 8. CONCLUSIONS

Systematic studies have been carried out on V-groove etching, with different etchants, etch masks, native oxide status and so on. Etchants are grouped into two types: HCl acid-related and oxidizing agent-related. (111)A V-grooves are usually formed in solutions containing oxidizing agents, while (111)B and (211)A V-grooves can only be formed in the HCl-related acids. Consideration of surface dangling bond and electron configurations leads to the following order of chemical reactivity of various surfaces:

- in solutions containing oxidizing agents:

  (111)B and (100) > (011) > (111)A

  (111)B and (100) > (211)A > (111)A

- in $5HCl:1H_3PO_4$ or other HCl-related acids:

  (100) > (111)B > (011) > (111)A

  (100) > (111)B > (211)A > (111)A

The results of the analysis are consistent with observations on etched groove profiles.

Because of its slow etch rate, a (111)A V-groove is easily obtained with an ideal, point bottom, as long as a dielectric etch mask is used. The relatively high etch rate of the (111)B surface means that the (111)B V-groove can only be formed when controlled mask undercutting occurs. A tiny flat (100) surface region is always present at the bottom of the groove due to diffusion-limited dissolution in the bottom region, along with the relatively high etch rate of the (111)B surface. Excessive undercutting results in a wide flat bottom, while too little undercutting produces an arrow-shaped groove; i.e., ones with (011)-like sidewalls at the top. In this work, optimized undercutting for the (111)B V-groove formation was established with the employment of a photoresist mask and minimization of

native oxides. Also, it was noticed that the formation of (111)B V-grooves is sensitive to small amounts of mask misalignment relative to the [011] direction, while that of (111)A V-grooves is not.

The relationship between native oxide and undercutting has also been investigated, using a vacuum-linked MBE and SiN_x deposition chambers. It was found that mask undercutting was almost completely eliminated, when the interfaces between mask and semiconductor were oxide-free. The only situation where undercutting was totally absent was with an epitaxial semiconductor layer used as the etch mask.

Finally, recipes have been established to obtain (111)A and (111)B V-grooves, which possess sharp bottoms and smooth sidewalls and can be used for subsequent epitaxial growth for quantum wire formation.

InP/InGaAs/InP quantum well structures have been grown onto the two types of V-grooves. The surface morphology of epitaxial growth, in both (111)A and (111)B V-grooves, has been shown to be significantly affected by the growth conditions, especially the V/III flux ratio. V-bottom sharpness and sidewall smoothness are improved with the following trends in growth conditions: a high growth temperature, a low V/III flux ratio and a high growth rate, for (111)A V-grooves; a moderate growth temperature, a low V/III flux ratio and a low growth rate, for (111)B faceted V-grooves. An understanding of these observations, such as a lower V/III flux ratio resulting in sharper grooves, requires consideration of both the migration of the group III adatoms and the influence of the group V dissociation/incorporation rate on group III incorporation.

The surface morphology in (111)A grooves is completely different from that in (111)B V-grooves: faceted bottoms in (111)A V-grooves and flat bottoms in (111)B V-grooves. This difference in growth behaviour can be attributed to the difference in orientation of the P-dimer bonds with respect to the groove directions. Also, the absence of

defects such as twins and stacking faults on the sidewalls suggests a step-flow growth mode.

While good surface morphology could be obtained with the InGaAs/InP grown in either a (111)A or a (111)B V-groove, cross-sectional TEM shows that extended defects occur for growths in the (111)B V-groove, but not in the (111)A V-groove. TEM and photoluminescence from selectively etched samples also show that crescent-shaped InGaAs/InP quantum wires have been successfully grown onto (111)A V-grooves. The crescent-shape and small lateral dimension give reasonable subband separations. The spatial origin of observed PL peaks has been resolved by a selective etching technique. The photoluminescence emission from the InGaAs wires shows a red shift, indicating significant In adatom migration.

The growth of InGaAsP in (111)A V-grooves results in a trend to planarization and the production of a flattening of the V-bottoms; thus, InGaAs/InGaAsP QWRs cannot be obtained in (111)A V-grooves. In contrast, the growth of an InGaAsP layer in (111)B V-grooves leads to sharper bottoms, and defect-free growth, indicating promise for QWR fabrication. EDS analysis shows that the composition in the bottom of the V-groove is both In- and P-rich. The higher P content would compensate the strain associated with the higher In/Ga ratio. The measured compositional variations are consistent with photoluminescence observations. The increased incorporation probability for P is explained as being a result of the increased growth rate, associated with group III adatom migration, which leads to an As under-pressure situation, enhancing P incorporation.

InGaAs/InGaAsP quantum wires have been achieved in the (111)B V-grooves. The QWRs are defect free and crescent shaped. A significant thickness variation across a small width at the V-groove bottom results in estimated subband separations of 17 meV, 5.7 meV and 22.2 meV for electrons, heavy holes and light holes respectively. These are

comparable to those achieved in the GaAs-based system. The existence of lateral confinement has been confirmed by the subband behaviour in the PL emission and is also supported by polarization measurements. PL studies, including temperature and pumping intensity dependence, indicate the tendency for band-filling in the QWR structures. The subband separation observed in PL spectra is consistent with the calculated values based on the wire geometry observed by TEM. The InGaAs/InGaAsP QWR structure should be able to serve as the active region of a QWR laser.

APPENDIX A

Recipe for (111)A V-groove etching

1). Deposit 1000 Å thick SiO_2 onto InP wafers, at 300 °C for 20 min. in a Technics PECVD chamber.

2). Apply primer (Shipley), wait for 30 sec, then spin at 4000 rpm for 30 sec.

3). Wait for 1 min, then apply positive PR (Shipley 1808), spin at 7000 rpm for 30 sec.

4). Softbake in oven at 85 °C for 25 min. (or on a hot plate at 90 °C for 2 min.)

5). Use Karl Suss MJB3 mask aligned to expose the wafer for 6.5 sec at standard optical intensity, with 1μm and 2μm wide mask lines aligned along the $[0\bar{1}1]$ orientation.

6). Develop in diluted Shipley 351 developer (1:5) for 30 sec. Di-ionized (DI) water rinse for 5 min.

7). Hardbake PR in oven at 120°C for 20 min. (or on a hot plate at 120°C for 2 min.)

8). Etch SiO_2 mask in $1HF:10NH_3F_4$ for 100 sec. Rinse in DI water for 5 min. and blow dry.

9). Etch in one of three etchants:

a). Br_2-Methanol (2% by volume),

b). $1HBr:1H_2O_2$,

c). $2HBr:2H_3PO_4:1K_2Cr_2O_7$

at 23 °C for 10 sec. Then rinse in DI water for 10 min.

10). Strip away PR using emt 130 stripper at 90 °C for 10 min. Rinse in DI water for 10 min.

11). Strip away SiO_2 mask using $1HF:10NH_3F_4$ for 3 min. Rinse in DI water for 10 min.

Recipe for (111)B V-groove etching

1). Clean wafers using UV ozoner for 10 min.

2). Strip oxides using undiluted hydrofluoric acid for 2 min. Then blow dry with N_2.

Do **NOT** rinse the wafers with DI water.

3). Apply positive PR (Shipley 1808) immediately (less than 10 sec) after drying off the wafers with dry nitrogen. Spin the wafers at 7000 rpm for 30 sec.

4). Softbake in oven at 85 °C for 25 min.

5). Use Karl Suss MJB3 mask aligned to expose the wafers for 6.5 sec at standard optical intensity, with 1μm and 2μm wide mask lines aligned along the [011] orientation.

6). Develop in diluted Shipley 351 developer (1:5) for 30 sec. DI water rinse for 2 min.

7). Etch in 5HCl:1H_3PO_4 at 35 °C for 15 sec (or 23 °C for 30 sec). Agitate as much as possible. Use a Teflon beaker and tweezers.

8). Strip away PR using emt 130 striper at 90 °C for 10 min. Rinse in DI water for 10 min.

REFERENCES

S. Adachi (1981), and H. Kawaguchi, "Chemical etching characteristics of (001) InP", J. Electrochem. Soc. **128**, 1342.

S. Adachi (1982), "Chemical Etching of InP and InGaAsP/InP", J. Electrochem. Soc.: Solid-State Sci. and Tech. **129**, 609.

L.T.P. Allen (1988), E.R. Weber, J. Wahburn, Y.P. Pao and A.G. Elliot, "Characterization of surface faceting on (110) GaAs/GaAs grown by molecular beam epitaxy", J. Crystal Growth **87**, 193.

Y. Arakawa (1986), K. Yahala and A. Yariv, "Dynamic spectral properties of semiconductor lasers with quantum-well and quantum-wire effects", Surf. Sci. **174**, 155

Y. Arakawa (1986) and A. Yariv, "Quantum well lasers-gain, spectra, dynamics", IEEE J. Quantum Electron **QE-22**, 1887.

Y. Arakawa (1982) and H. Sakaki, "Multidimensional quantum well laser and temperature dependence of its threshold current", Appl. Phys. Lett. **40**, 939.

T. Arakawa (1993), S. Tsukamoto, Y. Nagamune, M. Nishioka, J.H. Lee and Y. Arakawa, "Fabrication of InGaAs strained quantum wire structures using selective-area metal-organic chemical vapor deposition growth", Jpn. J. Apll. Phys. **32**, L1377.

J.R. Arthur (1968), "Interaction of Ga and As_2 molecular beam with GaAs substrates", J. Appl. Phys. **39**, 4032.

J.R. Arthur (1969) and J.J. Lepore, "GaAs, GaP and $GaAs_xP_{1-x}$ epitaxial films grown by molecular beam deposition", J. Vac. Sci. and Tech. **6**, 545.

H. Asai (1987), "Anisotropic lateral growth in GaAs MOCVD layers on (001) substrates", J. Crystal Growth **80**, 425.

R. Bhat (1988), E. Kapon, D.M. Hwang, M.A. Koza, and C.P. Yun, "Patterned quantum well heterostructures grown by OMCVD on non-planar substrates: applications to extremely narrow SQW lasers", J. Crystal Growth **93**, 850.

R. Bhat (1990), E. Kapon, J. Werner, D.M. Hwang, N.G. Stoffel, and M.A. Koza, "Organometallic chemical vapor deposition of InP/InGaAsP on nonplanar InP substrates: application to multiple quantum well lasers", App. Phys. Lett. **56**, 863.

R. Bhat (1991), E. Kapon, S. Simhony, E. Colas, D.M. Hwang, N.G. Stoffel, and M.A. Koza, "Quantum wire lasers by OMCVD growth on nonplanar substrates", J. Crystal Growth **107**, 716.

M. Boudreau (1993a), M. Boumerzoug, P. Mascher and P.E. Jessop, "Electron cyclotron resonance chemical vapor deposition of siliconoxynitrides using tri(dimethylamino)silan", Appl. Phys. Lett. **63**, 3014 .

M. Boudreau (1993b), M. Boumerzoug, R.V. Kruzelecky, P. Mascher, P.E. Jessop, and D.A. Thompson, "Electron cyclotron resonance of silicon oxynitride for optoelectronic applications", Mat. Res. Soc. Symp. Proc. **300**, 183.

N.J. Bulitka (1993a), A. Gupta, B.J. Robinson, D.A. Thompson, G.C. Weatherly and J.G. Simmons, "Characterization of InGaAs/InP epitaxial layers grown over V-groove patterned InP substrates using gas source molecular beam epitaxy", Mat. Res. Soc. Symp. Proc. **326**, 183.

N.J. Bulitka (1993b), "V-groove patterned substrate epitaxy using InGaAs/InP", Msc. Thesis, McMaster University, Hamilton, Canada.

P. Chen (1991), K.C. Rajkumar and A. Madhukar, "Growth control of GaAs epilayers with specular surface free of pyramids and twins on nonmisoriented (111)B substrates", Appl. Phys. Lett. **58**, 1771.

Y.P. Chen (1993), J.D. Reed, S.S. O'kefe, W.J. Schaff and L.F. Eastman, "Fabrication and characterization of InGaAs/GaAs strained quantum wires grown by molecular beam epitaxy", J. Crystal Growth **134**, 162.

D.K. Choi (1987), T. Takai, S. Erkoc, T. Halicoglu and W.A. Tiller, "Free surfaces and multilayer interfaces in the GaAs/AlAs system", J. Crystal Growth **85**, 9.

A.Y. Cho (1970), "Epitaxial growth of gallium phosphide on cleaved and polished (111) calcium fluoride", J. Appl. Phys. **41**, 782.

A.Y. Cho (1971a), M.B. Panish and I. Hayashi, "Molecular beam epitaxy of GaAs, AlGaAs and GaP", Proc. the Third Inter. Symp. on GaAs, Inst. of Phys. London, 18.

A.Y. Cho (1971b), "Thin deposition by molecular beam techniques", J. Vac. Sci. and Tech. **8**, S31.

J. Christen (1984), D. Bimberg, A. Steckenborn and G. Weimann, "Localization induced electron-hole transition rate enhancement in GaAs quantum wells", Appl. Phys. Lett. **44** 84.

J. Christen (1992), E. Kapon, E. Colas, D.M. Huang and L.M. Schiavone, "Cathodoluminescence investigation of lateral carrier confinement InGaAs/AlGaAs quantum wires grown by OMCVD on nonplanar substrates", Surf. Sci. **267**, 267.

J. Cibert (1986), P.M. Petroff, G.J. Dolan, S.J. Pearton, A.C. Gossard and J.H. English, "Optically detected carrier confinement to one and zero dimension InGaAs quantum well wires and boxes", Appl. Phys. Lett. **49**, 1275.

D.S. Citrin (1990) and Y.C. Chang, "Subband structures of semiconductor quantum wires from the effective bond-orbit model", J. Appl. Phys. **68**, 161.

D.S. Citrin (1991) and Y.C. Chang, "Theory of optical anisotropy in quantum-well-wire arrays with two-dimensional quantum confinement", Phys. Rev. **B43**, 11703.

E.M. Clausen (1989), H.G. Graighead, J.M. Worlock, J.P. Harbison, L. M. Schiavone, L.T. Florez, and B. Van der Gaag, "Determination of nonradiative surface layer thickness in quantum dots etched from single quantum well GaAs/AlGaAs", Appl. Phys. Lett. **55**, 1427.

G. Cliff (1975), and G.W. Lorimer, "The quantitative analysis of thin specimens", J. Microsc. **103**, 203.

S.W. Corzine (1993), R.H. Yan and L.A. Coldren, "Optical gain in III-V bulk and quantum well semiconductors", in Quantum well lasers, edt. by P.S. Zory, Academic, New York, 55

Chrismatec (1992), InPact InP Technical Catalogue.

W.C. Dautremont-Smith (1986) and D.P. Wilt, "The fabrication of grooved semiconductor devices", Patent Cooperation Treaty (PCT), Int. Publ. Number WO 86/01367, Int. Publ. Date, March 13. 1986.

J.E. Davey (1968) and T. Pankey, "Epitaxial GaAs film deposited by vacuum epitaxy", J. Appl. Phys. **39** 1941.

R. Dingle (1974), W. Wiegmann and C.H. Henry, "Quantized states of confined carriers in very thin $Al_xGa_{1-x}As$-GaAs-$Al_xGa_{1-x}As$ heterostructures, Phys. Rev. Lett. **33**, 827.

J.W. Edington (1976), "Practical electron microscopy in materials science", van Nostrand Reinhold, New York, 7

L. Esaki (1974) and L.L. Chang, "New transport phenomenon in a semiconductor superlattice", Phys. Rev. Lett. **33**, 495.

J.W. Faust (1962), "Etching of the III-V Intermetallic Compounds", in Compound Semiconductors, Volume 1, Preparation of III-V Compounds, R. K. Willardson and H.L. Goering (Eds.), Reinhold Publishing Corp., New York, 445.

P. Finnie (1995), M. Buchana, C. Lacelle and A.P. Roth, "The growth of quantum wire structures by selective area chemical beam epitaxy", unpublished

C.T. Foxon (1975) and B.A. Joyce, "Interaction kinetics of As_4 and Ga on (100) GaAs surfaces using a modulated molecular beam technique", Surf. Sci. **50**, 434.

C.T. Foxon (1980), B.A. Joyce and M.T. Norris, "Composition effects in the growth of $Ga(In)As_yP_{1-y}$ alloys by MBE", J. Crystal Growth **49**, 132.

C.T. Foxon (1983), "MBE growth of GaAs and III-V alloys", J. Vac. Sci. and Tech. **B1**, 293.

H. Fujikura (1994), T. Iwa-Ana and H. Hasegawa, "Fabrication of InGaAs wires by preferential molecular beam epitaxy growth on corrugated InP substrate", Jpn. J. Appl. Phys. **33**, 919.

Y.M. Galeuchet (1988), P. Roentgen, and V. Graf, "Buried GaInP/InP layers grown on nonplanar substrates by one-step low pressure metalorganic vapor phase epitaxy", Appl. Phys. Lett. **53**, 2638.

Y.M. Galeuchet (1991), "Metalorganic vapor-phase epitaxy on patterned substrates for the fabrication of in-situ buried $Ga_xIn_{1-x}As/InP$ nanostructures", Ph.D. thesis, No. 933, Ecole Polytechnique Federale De Lausanne, Switzerland

H.C. Gatos (1960a), M.C. Lavine, "Etching and inhibition of the {111} surfaces of the III-V intermetallic compounds: InSb", J. Phys. Chem. Solids **14**, 169.

H.C. Gatos (1960b) and M.C. Lavine, "Characteristics of the {111}surfaces of the III-V intermetallic compounds", J. Electrochemical Soc. **107**, 427.

J.L. Gentner (1995), Ph. Jarry and L. Goldstein, "Chemical beam etching of InP in GSMBE", Proce. of InP and Related Materials Conf., Schwabisch Gmund, Germany 636.

J.I. Goldstein (1984), D.E. Newbury, P. Echlin, D.C. Joy, C. Fiori and E. Lifshin, "Scanning microscopy and X-ray microanalysis", Plenum, New York, 166.

J.D. Granges (1985) and D.K. Wickenden, "Comparison and critique of the epitaxial growth technologies", The Technology and Physics of Molecular Beam Epitaxy, edt. by E.H.C. Parker, Plenum Press, New York, 629.

H. Gerischer (1968) and W. Mindt, "The mechanisms of the decomposition of semiconductors by electrochemical oxidation and reduction", Electrochemica Acta **13**, 1329.

M. Grundmann (1994), J. Christen, M. Joschko, O. Stier, D. Bimberg and E. Kapon, "Recombination kinetics and intersubband relaxation in semiconductor quantum wires", Semicon. Sci. and Technol. **9**, 1939

S. Guha (1993) and A . Madhukar, "An explanation for the directionality of interfacet migration during molecular beam epitaxial growth on patterned substrates", J. Appl. Phys. **73**, 8662.

K.G. Gunther (1958), "Aufdampfschichten Aus Halbleitenden III-V Verbindungen," Zeitschrift fur Naturforschung, **13a**, 1081.

A. Gupta (1997), Ph.D. thesis, McMaster University

M. Hata (1990), T. Isu, A. Watanabe, and Katayama, "Distributions of growth rates on patterned surfaces measured by scanning microprobe reflection high-energy electron diffraction", J. Vac. Sci. and Tech. **B8**, 692.

R.B. Heimann (1982), "Principle of chemical etching - the art and science of etching crystal", in Silicon Chemical Etching, edt. J. Grabmaier, Springer-Verlag, New York, 173.

B. Henle (1993), R. Rudeloff, H. Bolay and F. Scholz, "In situ selective-area etching and MOVPE regrowth of GaInAs-InP on InP substrates", Semicond. Sci. Technol. **8**, 994.

P.G. Hofstra (1993), D.A. Thompson, B.J. Robinson and R.W. Streater, "Application of an in situ hydrogen plasma to the epitaxial regrowth of InP grown by molecular beam epitaxy" J. Vac. Sci. Technol., **B11**, 985.

P.G. Hofstra (1995), B.J. Robinson, D.A. Thompson, and S.A. McMaster, "Etching of InP surface oxide with atomic hydrogen produced by electron cyclotron resonance", J. Vac. Sci. Technol. **A13**, 2146.

G. Hollinger (1991), D. Gallet, M. Gendry, M.P. Besland and J. Joseph, "Evidence for new passivating indium rich phosphate prepared by ultraviolet/ozone oxidation of InP", Appl. Phys. Lett., **59**, 1617.

H.Q. Hou (1993) and C.W. Tu, "Homoepitaxial growth of InP in (111)B substrates by gas source molecular beam epitaxy", Appl. Phys. Lett. **62**, 281

H. F. Hsieh (1990) and H. C. Shih, "Synergism between chloride and photons in the InP dissolution mechanism", J. Electrochem. Soc. **137**, 1348.

D.T.C. Huo (1987), J.D. Wynn, S.G. Napholtz, F. R. Lenzo, and D.P. Wilt, "A novel etch mask process for the etching of (011) oriented facet V-grooves in InP (100) wafers", J. Electrochem. Soc. **134**, 2850.

D.T.C. Huo (1988a) , J.D. Wynn, S.G. Napholtz, and D.P. Wilt, "Controlled undercutting of V-groove channels for InP by photoresist etch mask", J. Electrochem. Soc. **135**, 1231.

D.T.C. Huo (1988b) , J.D. Wynn, S.G. Napholtz, and D.P. Wilt, "Preferential etching of InP through photoresist masks", J. Electrochem. Soc. **135**, 2334.

P. Ils (1994), M. Michel and F. Forchel, I. Gyuro, M. Llenk and E. Zielinski, "Room temperature study of strong lateral quantization effects in InGaAs/InP quantum wires", Appl. Phys. Lett. **64**, 496.

H. Imamoto (1989), F. Sato, K. Imanaka, and M. Shimura, "Migration-enhanced epitaxy on a (111)B oriented GaAs substrate", Appl. Phys. Lett. **55**, 115.

S.H. Jones (1991), L.K. Seidel, K.M. Lau and M. Harold, "Patterned substrate epitaxy surface shapes", J. Crystal Growth **108**, 73.

K. Kamath (1996), P. Bhattacharya and J. Philips, "Room temperature luminescence from self-organized InGaAs/GaAs quantum dots with high size uniformity", 9th International Conference on Molecular Beam Epitaxy, Malibu, California.

E. Kapon (1989a), D.M. Hwang and R. Bhat, "Stimulated emission in semiconductor quantum wire heterostructure", Phys. Rev. Lett. **63**, 430.

E. Kapon (1989b), S. Simhony, R. Bhat and D.M. Huang, "Single quantum wire semiconductor lasers", Appl. Phys. Lett. **55**, 2715.

E. Kapon (1992a), "Quantum wire lasers", Proceedings IEEE **80**, 398.

E. Kapon (1992b), K. Kash, E.M. Clausen Jr., D.M. Huang, and L.M. Schiavone, "Luminescence characteristics of quantum wires grown by organometallic chemical vapor deposition on nonplanar substrates", Appl. Phys. Lett. **60**, 477.

E. Kapon (1992c), M. Walther, J. Christen, M. Grundmann, C. Caneau, D.M. Hwang, E. Colas, R. Bhat, G.H. Song and D. Bimberg, "Quantum wire heterostructures for optoelectronics applications", Superlattices and Microstructures **12**, 491.

E. Kapon (1993), "Quantum wire semiconductor lasers", in: Quantum Well Lasers, edt. by P.S. Zory, Academic, New York, 466.

E. Kapon (1994), " Lateral patterning of quantum well heterostructures by growth of nonplanar substrates", in: Epitaxial Microstructure, edited by A.C. Gossard, Academic Press, New York, 259.

W. Kern (1978), "Chemical etching of silicon, germanium, gallium arsenide, and gallium phosphide", RCA Review, **39**, 278.

S. Koshiba (1994), H. Noge, H. Akiyama, T. Inoshita, Y. Nakamura, A. Shimizu, Y. Nagamune, M. Tsuchiya, H. Kano, and H. Sakaki and K. Wada, "Formation of GaAs ridge quantum wire structures by molecular beam epitaxy of patterned substrates", Appl. Phys. Lett. **64**, 363.

R. M. Lammert (1995), P.V. Mena, D.V. Forbes, M.L. Osawski, S.M. Kang and J.M. Coleman, "Strained-layer InGaAs-GaAs-AlGaAs lasers with monolithically integrated photodiodes by selective-area MOCVD", IEEE Photonics Tech. Lett. **7**, 247.

R. M. Lammert (1996), G.M. Smith, J.H. Hughes, M.L. Osawski, A.M. Jones and J.M. Coleman, "MQW wavelength-tunable DBR lasers with monolithically integrated external cavity electrosbsorption modulators with low-driving-voltages fabricated by selective-area MOCVD", IEEE Photonics Tech. Lett. **8**, 797.

R.R. LaPierre (1995), B.J. Robinson and D.A. Thompson, "Lateral composition modulation in InGaAsP deposited by gas source molecular beam epitaxy on (100)- and (h11)-oriented InP substrates", App. Surf. Sci. **90**, 437.

R.R. LaPierre (1996), B.J. Robinson and D.A. Thompson, "Group V incorporation in InGaAsP grown on InP by gas source molecular beam epitaxy", J. App. Phys. **79**, 3021.

T.L. Lee (1995), J.S. Liu and H.H. Lin, "The incorporation behavior of As and P in GaInAsP on InP grown by gas source molecular beam epitaxy", J. Crystal Growth **155**, 16.

X. Li (1993), W.I. Wang, A.Y. Cho and D.L. Sivco, "Amphoteric doping of Si in InAlAs/InGaAs/InP (311)A heterostructures grown by molecular beam epitaxy", J. Vac. Sci. Technol. **B11**, 912.

M.H. Loretto (1984), "Electron Beam Analysis of Materials", Chapman and Hall, New York, 205.

A.C. Maciel (1994), J.F. Ryan, R. Rinaldi, R. Cingolani, M. Ferrara, U. Matri, D. Martin, F. Morier-Gemound and F.K. Reinhart, "Hot-carrier photoluminescence from GaAs V-groove quantum wires", Semicond. Sci. Technol. **9**, 893.

O. Madelung(1991), "Semiconductors group IV elements and III-V compounds", Springer-Verlag, New York, 126.

A. Madhukar (1993), "Growth of semiconductor heterostructures on patterned substrates: defect reduction and nanostructures", Thin Solid Films, **231**, 8.

B.E. Maile (1989), A. Forchel, R. Germann, D. Grutzmacher, H.P. Meier and J.P. Reithmaier, "Fabrication and optical characterization of quantum wires from semiconductor materials with varying In content", J. Vac. Sci. Technol. **B7**, 2030.

R. Mirin (1996), J. Bowers and A. Gossard, "Alternating MBE formation of multiple layers of InGaAs quantum dots and application to quantum dot laser", 9th International Conference on Molecular Beam Epitaxy, Malibu, California.

J.H. Neave (1985), P.J. Dobson and B.A. Joyce, "Reflection high-energy electron diffraction oscillations from vicinal surfaces - a new approach to surface diffusion measurements", Appl. Phys. Lett. **47**, 100.

M. Notomi (1993) and T. Tamamura, "High quality InGaAs/InP quantum wires fabricated by electron beam lithography", Proce. of Con. on InP and Related Materials, Sapporo, Japan, 715.

P.H.L. Notten (1984), "The etching of InP in HCl solutions: a chemical mechanism", J. Electrochem. Soc., **131**, 2641.

P.H.L. Notten (1987), "The electrochemistry of InP in Br_2/HBr solutions and its relevance to etching behaviour", Appl. Surf. Sci. **28**, 331.

P. H. L. Notten (1991), "The influence of native oxide layers of InP on the shape of etching profiles at resist edges", J. Electrochem. Soc., **138**, 243.

R. Notzel (1996), "Self-organized growth of quantum-dot structures", Semicond. Sci. Technol. **11**, 1365.

M. Ohtsuka (1988) and S. Miyazawa, "Model for molecular-beam-epitaxy growth over nonplannar surfaces", J. Appl. Phys. **64**, 3522.

W. Pan (1994), H. Yaguchi, K. Onabe, K. Wada, Y. Shiraki and R. Ito, "Metalorganic vapor phase epitaxial growth and luminescence properties of GaAs/GaAsP quantum wires" J. Crystal Growth **145**, 702.

M.B. Panish and S. Sumski (1984), "Gas source molecular beam epitaxy of $Ga_xIn_{1-x}P_yAs_{1-y}$", J. Appl. Phys. **55**, 3671

M.B. Panish (1989), "Molecular beam epitaxy", AT&T Technical J., Jan/Feb 1989, 43.

J.I. Pankove (1971), "Optical process in semiconductors", Dover, New York, 107

D.D. Perovic (1995), M.R. Castell, A. Howie, C. Lavoie, T. Tiejie and J.S.W. Cole, "Field-emission SEM imaging of compositional and doping layer semiconductor superlattices", Ultramicroscopy **58**, 104.

S.B. Phatak (1979), and G. Kelner, "Material-selective chemical etching in the system InGaAsP/InP", J. Electrochem. Soc. **126**, 287.

K. Ploog (1987), "Molecular beam epitaxy of artificially layers III-V semiconductors on a atomic scale", Proceedings of a NATO Advanced Study Institute on Physics and Applications of Quantum Wells and Superlattices, Erice, Sicily, Italy April 1987, Plenum Press, New York

P.M. Petroff (1994), "Direct growth of nanometter-size quantum wire superlattices", in: Epitaxial Microstructure, edited by A.C. Gossard, Academic Press, New York, 219.

A. Pratt (1994), R.L. Williams, C.E. Norman, M.R. Fahy, A. Marinopoulou, and F. Chatenoud," Indium migration control on patterned substrates for optoelectronic applications", Appl. Phys. Lett. **65**, 1009.

R. Rinaldi (1993), R. Cingolani, F. Rossi, L. Rota, M. Ferrara, P. Lugli, E. Molinari, U. Marti, D. Martin, F. Morier-Gemoud, P. Ruterana and F.K. Reinhart, "Investigation of quantum states in V-shaped GaAs quantum wires", in Gallium Arsenide and Related Compounds, Inst. Phys. Conf. Ser. No. 136, Inst. of Phys. and Phys. Sc., London, 233.

R. Rinaldi (1994), M. Ferrara, R. Cingolani, U. Marti, D. Martin, F. Morier-Gemoud, P. Ruterana and F.K. Reinhart, "Evidence of one-dimensional exciton in GaAs V-shaped quantum wires" Phys. Rev. **B50**, 11795.

B.J. Robinson (1992), D.A. Thompson, P.G. Hofstra, G. Balcaitis and S.A. McMaster, "The use of an in-situ ECR hydrogen plasma to remove the oxide from InP substrates prior to epitaxial growth", Conference Proceedings of 4th International Conference on Indium Phosphide and Related Materials, May 1992, Newport, Rhode Island, USA, 90.

D.K. Schroder (1990), "Semiconductor material and device characterization", John Wiley & sons, New York.

P. C. Sercel (1991) and K. J. Vahala, "Polarization dependence of optical absorption and emission in quantum wires", Phys. Rev. **B44**, 5681.

H. Seki (1986) and A. Koukitu, " Thermodynamic analysis of molecular beam epitaxy of III-V semiconductors", J. of Crystal Growth **78**, 342.

X. Q. Shen (1993), M Tanaka, and T. Nishihaga, "Resharpening effect of AlAs and fabrication of quantum-wires on V-grooved substrates by molecular beam epitaxy", J. Cryst. Growth **127**, 932.

X.Q. Shen (1994a), D. Kishimoto and T. Nishihaga, "Arsenic pressure dependence of surface diffusion of Ga on Nonplanar GaAs substrates", Jpn. J. Appl. Phys. **33**, 11.

X.O. Shen (1994b), M Tanaka, K. Wada and T. Nishihaga, "Molecular beam epitaxial growth of GaAs, AlAs and $Al_{0.45}Ga_{0.55}As$ on (111)A-(0101) V-groove substrates", J. Cryst. Growth **134**, 85.

G.J. Shrobilgen (1997), private communication.

S. Simhony (1991), E. Kapon, E. Colas, D.M. Huang, N.G. Stoffel and P. Worland, "Vertically stacked multiple-quantum-wire semiconductor diode lasers", Appl. Phys. Lett. **59**, 2225.

J.S. Smith (1985), P.L. Derry, S. Margalit, and A. Yariv, "High quality molecular beam epitaxial growth on patterned GaAs substrates", Appl. Phys. Lett. **47**, 712.

T. Sugaya (1993), M. Kaneko, Y. Okada and M. Kawabe, "Fabrication of GaAs quantum wire structures by hydrogen-assisted molecular beam epitaxy", Jpn. J. Appl. Phys. **32** L1834.

Y. Sugimoto (1993), S. Kohmoto, H. Saito, N. Hamao and K. Asakawa, "Fabrication of quantum fine structures combined with pattern formation and crystal growth", Optoelectronics-Device and Technol. **8**, 577.

S. Tiwari (1994), G. D. Pettit, K.R. Milkove, F. Legoues, R.J. Davis and J.M. Woodall, "High efficiency and low threshold current strained V-groove quantum-wire lasers"Appl. Phys. Lett. **64**, 3536.

W.T. Tsang (1977), and A.Y. Cho, "Growth of GaAs-$Ga_{1-x}Al_xAs$ over preferentially etched channels by molecular beam epitaxy: a technique for two-dimensional thin-film definition", Appl. Phys. Lett. **30**, 293.

W. T. Tsang (1994), R. Kapre and P.F. Sciortino, Jr., "In-situ dry etching of InP using phosphorus tricholoride and regrowth inside a chemical epitaxial growth chamber", J. Crystal Growth 136, 42.

M. Tsuchiya (1989), J.M. Gaines, R.H. Yan, R.J. Simes, P.O. Holtz, L.A. Coldren and P.M. Petroff, "Optical anisotropy in a quantum-well-wire array with two-dimensional quantum confinement", Phys. Rev. Lett. **62**, 466.

S. E. Turley (1982) and P. D. Greene, "LPE growth on structured {100} InP substrates and their fabrication by preferential etching", J. Cryst. Growth, **58**, 409.

V.M. Ustinov (1996), A. Egorov, A.E. Zhukov, N.N. Ledentsov, M.V. Maksimov, A.F. Tsatsul'nikov, S.V. Zaitsev, N. Gordeev, A. Kosogov, P.S. Kop'ev, D. Bimberg and Z.I. Alferov, "Low-threshold (100 A/cm^2) injection lasers based on vertically coupled

InGaAs/GaAs quantum dots", 9th International Conference on Molecular Beam Epitaxy, Malibu, California.

S. Uekusa (1985) and K. Oigawa, "Preferential etching of InP for submicron fabrication with HCl/H_3PO_4 solution", J. Electrochem. Soc.: Solid-State Sci. and Technol., **132**, 672.

D.B. Williams (1984), Practical Analytical Electron Microscopy in Materials Science, Phillips Electronic Instruments Inc. Electron Optics Publishing Group, Mahwah, New Jersey, 67.

M. Walther (1993), E. Kapon, C. Caneau, D.M. Hwang and L.M. Schiavone, "InGaAs/GaAs strained quantum wire lasers grown by organometallic chemical vapor deposition on nonplanar substrates", Appl. Phys. Lett. **62**, 2170.

W. Wegscheider (1994), L. Pfeiffer, M. Dignam, A. Pinczuk, K. West and R. Hull, "Lasing in low-dimensional structures formed by cleaved edge overgrowth", Semicond. Sci. Technol. **9**, 1933.

C. Weisbuch (1991) and B. Vinter, "Quantum semiconductor structures: fundamental and applications", Academic, New York

T. Yamauchi (1992), Y. Arakawa and J.N. Schulman, "Quantum wires with strain effect: tight-binding analysis", Surface Sci. **267**, 291.

A. Yariv (1989), "Quantum well semiconductor lasers are taking over", IEEE Circuits and Device Magazine **5**, 25

H.A. Zarem (1989), P.C. Sercel, M.E. Hoenk, J.A. Lebens, and K.J. Vahala, "Nanometer scale wire structures fabricated by diffusion-induced selective disordering of a GaAs(AlGaAs) quantum well", Appl. Phys. Lett. **54**, 2692.